LA--10174-T

DE84 017074

Elastic Scattering of Polarized Protons on Deuterium at 800 MeV

Gary S. Weston*

*Guest Scientist at Los Alamos. Department of Physics, University of California at Los Angeles, Los Angeles, CA 90024.

Los Alamos Los Alamos National Laboratory
Los Alamos, New Mexico 87545

TABLE OF CONTENTS

LIST OF TABLES

LIST OF FIGURES

Acknowledgments

I am most grateful to my thesis advisors Professor George J. Igo and Professor Charles A. Whitten Jr. for their guidance and encouragement throughout my graduate program. George has always been very stimulating and energetic and has provided guidance whenever needed. Chuck has been a great friend and always extremely helpful.

I would also like to thank Drs. B. Aas, F. Sperisen, M. Bleszynski, K. Jones, J. McClelland, M. Gazzaly, G. Pauletta, R.L. Boudrie, N. Tanaka, M.W. McNaughton, B.E. Bonner, C.L. Hollas, Professor P.J. Riley and students A. Azizi, D. Lopiano, A. Mokhtari, J. Wagner, D. Adams, R.W. Fergeusen, E.C. Milner and G.J. Kim. I also want to thank Gloria Garcia, Maggie Eutsler, Chris Weaver, Barbara Cabot, Bea Blonsky, Katy Humphrey, Penny Lucky, Julie Sturm, and the other LAMPF and UCLA people who were very helpful. I am also indebted to Drs. S. Ishimoto, Y. Ohashi, and Professor A. Masaiike and the rest of the polarized target group. I especially want to thank Drs. R.L. Blake and E.E. Fenimore for their support.

Publications

1. E.E. Fenimore and G.S. Weston, " Fast Delta Hadamard Transform", Applied Optics 20(1981)3058.

2. G.S. Weston et. al., "Measurement of the Spin Rotation Parameters for $\vec{p}d \to \vec{p}d$ Elastic Scattering at 800 MeV", Bull. Am. Phys. Soc. 28(1983)996.; presented at Div. Nucl. Phys., Notre Dame, In. 10/83

3. Sun Tsu-hsun et. al., "Measurement of the Spin-Rotation Parameters for $\vec{p}d \to \vec{p}d$ at 496, 647 and 800 MeV", accepted by Phys. Rev. C.

4. F. Sperisen et. al., "Measurement of 3rd Order p-d Observables using a Polarized Deuteron Target", Bull. Am. Phys. Soc. 28(1983)996.

5. M. Gazzaly et. al., "Measurement of A_{nn} of $\vec{p}$-$\vec{p}$ Elastic Scattering in the Coulomb Interference Region at 1.46 and 1.28 GeV", Bull. Am. Phys. Soc. 28(1983)995.

6. N. Tanaka et. al., "Measurement of A_{nn} for $\vec{p}\vec{p} \to d\pi^+$ Reaction at 1.46 and 1.28 GeV/c", Bull. Am. Phys. Soc. 28(1983)995.

7. S. Ishimoto et. al., "A Polarized Proton and Deuteron Target for the LAMPF HRS", Bull. Am. Phys. Soc. 28(1983)991.

8. J.B. McClelland et. al., "Complete Measurement of Polarization-Transfer Observables for the Reaction $^{12}C(p,p)^{12}C^*$ at 500 MeV", Phy. Rev. Lett. 52(1984)98.

9. J.B. McClelland et. al., "The Experimental Determination of the Effective Nucleon-Nucleon Interaction for P-Nucleus Reactions at Intermediate Energies" , Nucl. Phy. A396(1983)29c.

10. Sun Tsu-hsun et. al., "The Spin Rotation Parameters D_{nn}, D_{sl}, D_{ss}, D_{ls}, D_{ll} and P for $\vec{p}\vec{d} \to \vec{p}\vec{d}$ Elastic Scattering at 500 and 800 MeV", Few-Body Conference, Karlsruhe, Germany 1983.

11. D.J. Cremans et. al., "D_{ss}, D_{ls}, D_{ll} and P for pp Elastic Scattering at 699 and 750 MeV", Few-Body Conference, Karlsruhe, Germany 1983.

12. S.E. Turpin et. al., "First Measurement of K_{nn} in the reaction $\vec{p}p \to \vec{d}\pi^+$ at 800 MeV", Few-Body Conference, Karlsruhe, Germany 1983.

13. B.E. Bonner et. al., "The Polarization Observables D_{nn}, P and A for $\vec{p}p \rightarrow \vec{p}\pi^+n$ at 800 MeV", Few-Body Conference, Karlsruhe, Germany 1983.

14. B.E. Bonner et. al., "A Novel Technique for measruing the Vector Polarization of a Deuteron", Few-Body Conference, Karlsruhe, Germany 1983.

15. J.J. Kelley et. al., "Energy Dependence of the Medium Modifications of the Two-Nucleon Effective Interaction Between 100 and 500 MeV", Bull. Am. Phys. Soc. (1983).

16. J.J. Kelley et. al., "Evidence for a New 3^- State in ^{16}O at 9.85 MeV", Bull. Am. Phys. Soc. (1983).

17. D. Lopiano et. al., "Analysis of 300 and 500 MeV Proton Scattering Data for ^{16}O", Bull. Am. Phys. Soc. (1983).

18. S.E. Turpin et. al., "Measurement of K_{nn} for $\vec{p}p \rightarrow \vec{p}\pi^+n$ at 800 MeV", Bull. Am. Phy. Soc. 28(1983)705.

19. G.S. Weston et. al., "Measurement of the Proton Spin Observables for $\vec{p}d \rightarrow \vec{p}d$ at 800 MeV", to be submitted to Phys. Rev. Lett.

ABSTRACT OF THE DISSERTATION

Elastic Scattering of Polarized Protons

on Deuterium at 800 MeV

by

Gary Steven Weston

Doctor of Philosophy in Physics

University of California, Los Angeles, 1984

Professor George J. Igo, Co-Chair

Professor Charles A. Whitten Jr., Co-Chair

A specific set of spin transfer coefficients has been measured for proton-deuteron elastic scattering at 800 MeV using an unpolarized liquid deuterium target. The experiment was done using the High Resolution Spectrometer (HRS) at the Los Alamos Meson Physics Facility (LAMPF) with a polarized proton beam. The scattered proton spin direction was determined using the Focal Plane Polarimeter (FPP) of the HRS, which employs a carbon analyzer. Some of the spin dependent parameters measured in this experiment are of considerable interest because they provide selective information about the nucleon-nucleon (NN) amplitude. Since the deuteron is the simplest bound nucleus, pd elastic scattering is particularly well

suited for testing multiple scattering theories. These measurements will also be used to eventually determine the full pd collision matrix, which contains all possible information about the scattering process. In addition, the experimental setup is described for a polarized proton-polarized deuterium target spin transfer experiment also done at the HRS at 800 MeV incident proton energy.

Introduction

In recent years a considerable amount of experimental and theoretical work has been done in the field of proton-nucleus scattering. The prime motivation is studying the strong interaction and determining nuclear structure. Together with the research done on the weak nuclear, electromagnetic and gravitational interactions, one hopes to understand the four fundamental forces of nature. Although proton-nucleus scattering at intermediate energies does not deal with the production of exotic particles, it does probe the spin dependence of the strong interaction.

In the past, the study of proton-nucleus scattering has mainly been limited to predicting and measuring the unpolarized differential cross section and analyzing power. With the recent advances in polarized beams and targets many more observables could be measured. These observables include spin transfer coefficients and correlation parameters using polarized beams and targets and measuring polarizations of outgoing particles in particular reactions.

At intermediate energies (100 MeV to 1 GeV) there have been a large number of proton-nucleus scattering experiments performed. The hope is to accurately predict the measurable observables. Proton-deuterium scattering is the simplest proton-nucleus reaction. Therefore it is one of the more important proton-nucleus experiments to be understood if the spin dependence in these reactions is to be on a sound basis.

In studying proton-deuteron scattering, six quark structures in nuclei might be probed, but they are not expected to be important at the small momentum transfers measured in this experiment. In addition, the extraction of three body forces may be unraveled. Currently the motivation is to determine the reasons for the discrepancies that exist between the proton-deuteron spin transfer data and a non-eikonal multiple scattering theory. With the recent advances in the relativistic impulse approximation based on the Dirac equation, proton-deuteron spin observables provide a good data base for testing the validity of a Dirac multiple scattering approach. The measurement of some proton-deuteron spin transfer observables at 800 MeV is described in this thesis.

1.A. Physics of Proton - Deuteron Scattering

The measurement of the spin-dependent observables in p-d elastic scattering can provide a sensitive test of the multiple scattering theory. One of the basic motivations for this work is to test the multiple scattering models and to determine whether or not the proton-deuteron observables are predictable using known free NN amplitudes. If so, then one could use these measurements to extract information on the NN interaction[1-1], such as the double spin flip components of the np amplitudes, which are not so well determined above 500 MeV. The observables D_x and D_z , which are linear combinations of the measured observables are very sensitive to the NN double spin flip amplitudes δ and ε [1-2] (see sections 1.C.1. and 1.E). The measurement of the pd spin observables will hopefully isolate problems in the multiple scattering theories. With the recent success of the relativistic Dirac impulse approximation in proton-nucleus spin dependent formalism, these data provide a sensitive test of the Dirac approach. Another goal is to completely determine the p-d scattering amplitude. It is made up of 12 complex amplitudes (see section 1.D.), so at least 23 independent observables are required to determine it up to a phase. Eventually one hopes to unravel three-body forces in nuclei. The ultimate goal would be to see six-quark effects in proton-deuteron scattering.

At forward angles, where the momentum transfer is not too large ($-t < 1.2$ $(GeV/c)^2$), the Glauber multiple scattering theory including non-eikonal (non-linear propagation) corrections is in good agreement with deuteron tensor analyzing power measurements[1-3]. In particular, the tensor analyzing power data provide a very sensitive method for determining the non-eikonal corrections to the Glauber theory due to the deuteron d-state. But there are large discrepancies between the multiple scattering calculation and the 800 MeV HRS proton spin rotation and depolarization data (the data presented in this thesis). The non-eikonal corrections are small in comparison to the discrepancies between the data and the calculation for the Wolfenstein parameters. The multiple scattering calculation includes non-eikonal corrections and uses the NN amplitudes taken from the (FA-83) phase shift analysis of Arndt and Roper[1-4]. Reid soft core deuteron wave functions[1-38] were used and the energy dependence of the NN amplitudes has been taken into account in the single and double scattering terms. The double scattering term is evaluated with the exact projectile free-wave propagator.

1.B. Current Status of Proton - Deuteron Measurements

In the last twenty years a great deal of nucleon-deuteron theoretical and experimental work has been done at intermediate energies. Several review articles exist that give some information on the status of the proton-deuteron scattering system[1-10-13].

Bennett et. al.[1-14] and Coleman et. al.[1-15,16] measured the p-d unpolarized differential cross section at 1 GeV and 1-2 GeV incident proton energy respectively. The differential cross section has a sharp forward peak followed by a region of much slower decrease at higher momentum transfer. The two regions are dominated by single and double scattering respectively. Originally, a large minimum in the cross section was predicted due to the destructive interference between the S-wave single and double scattering contributions. However, as noted by Harrington[1-17], effects due to the D-wave component in the deuteron wave function (~4-6%) are large enough to fill in the dip, turning it into a shoulder which gives good agreement between the theory and the data. As shown by Franco and Glauber[1-18], the p-d cross section is very dependent on the polarization of the deuteron spin. Several groups[1-19-24] have made pd differential cross section and proton analyzing power measurements in the incident proton energy range 316 MeV to 2 GeV. The asymmetry in the scattering of protons on a polarized deuterium target was measured at 1.21 GeV/c[1-25]. The spin alignment of elastically scattered deuterons was measured in a deuteron-proton double

scattering experiment using a 3.6 GeV/c deuteron beam[1-26]. Good agreement is seen between the Glauber model and all of these data.

More recently, tensor analyzing powers have been measured in pd scattering between 0.4 - 1 GeV using a vector and tensor polarized deuteron beam[1-27]. Analysis of these data using multiple scattering theory demonstrates the considerable sensitivity of the deuteron observables to the quadrupole form factor of the deuteron and to the double spin flip components of the NN amplitudes[1-28]. Also using these data, it is seen that the non-eikonal corrections are essential to the Glauber diffraction theory, especially for $-t > 0.2$ (GeV/c)^2, where discrepancies of up to 150% are observed with the theory based on the eikonal (straight-line propagation) approximation[1-3]. The non-eikonal multiple scattering theory with various corrections is in very good agreement with the deuteron tensor analyzing powers.

The unpolarized differential cross section and proton analyzing power at 800 MeV have recently been measured by Winkelmann et. al.[1-29] at the External Proton Beam (EPB) line at LAMPF.

The Wolfenstein parameters[1-8,9] have also been measured for $\vec{p}d \to \vec{p}d$ elastic scattering at EPB for 496, 647 and 800 MeV incident proton beam energies. Rahbar et. al.[1-30,31] measured D_{nn}, D_{ss}, $D_{\ell s}$, P and A_y for $\vec{p}d \to \vec{p}d$ elastic scattering using 496 and 800 MeV beams for lab angles 20-60°. The four - momentum transfer range covered at 496 MeV was 0.265 (GeV/c)$^2 < -t < 0.709$ (GeV/c)^2; for 800 MeV it was 0.242 (GeV/c)$^2 < -t < 1.494$ (GeV/c)^2. Sun Tsu-hsun et. al.[1-32,33] measured D_{nn}, $D_{s\ell}$, D_{ss}, $D_{\ell s}$, $D_{\ell\ell}$, P and A_y for $\vec{p}d \to \vec{p}d$ elastic

scattering at 496 and 647 MeV from 30 to 60° lab angle (0.293 $(GeV/c)^2 < -t < 0.883\ (GeV/c)^2$ for 496 MeV; $0.398\ (GeV/c)^2 < -t < 1.175\ (GeV/c)^2$ for 647 MeV) and $D_{s\ell}$, $D_{\ell\ell}$ at 800 MeV from 20 to 50° lab angle ($0.243\ (GeV/c)^2 < -t < 1.152\ (GeV/c)^2$). This work improved the statistical errors by a factor of two or three over the first measurements of D_{nn}, D_{ss} and $D_{\ell s}$ at 496 MeV by Rahbar et. al.[1-30,31] and represent the first measurements of $D_{s\ell}$, $D_{\ell\ell}$ at 800 MeV and all the proton observables at 647 MeV at these relatively large momentum transfers.

In the present work at the HRS we have measured the spin rotation parameters D_{nn}, D_{ss}, $D_{s\ell}$, $D_{\ell s}$, $D_{\ell\ell}$, P and the analyzing power, A_y, for $\vec{p}d \to \vec{p}d$ elastic scattering at 800 MeV from 3 to 28° lab angle ($.006\ (GeV/c)^2 < -t < 0.458\ (GeV/c)^2$)[1-34]. This represents the first measurement of these parameters at intermediate energies in the small momentum transfer region and completes the measurement of the proton spin transfer observables for $\vec{p}d \to \vec{p}d$ elastic scattering at 800 MeV out to $-t \approx 1\ (GeV/c)^2$. The data are presented in section 4.B.

Even more recently (November 1983) we have measured these same proton spin transfer observables at 500 MeV also at the HRS in the small momentum transfer range. These data are now being analyzed. A proposal (#853) to measure these parameters at 650 MeV and the unpolarized differential cross sections at 500, 650 and 800 MeV at the HRS has been accepted and will probably be done very soon.

In addition to the proton spin observables, we have begun a large program to measure all observables in the reaction $\vec{p}\vec{d} \rightarrow \vec{p}d$ using a polarized proton beam, polarized deuteron target and measuring the polarization of the final state proton at the HRS at 800 MeV. In September and October 1983, we did the $\hat{n}$-type polarized deuterium target part and during 1984 and 1985 we hope to complete the $\hat{\ell}$- and $\hat{s}$-type polarized deuteron target configurations. The $\hat{n}$-type part of the experiment is described in the appendix. In conjunction with the previous p-d measurements, these polarized deuteron target experiments should provide a sufficient number of independent observables to completely determine the p-d scattering amplitude at 800 MeV.

1.C. The Proton-Deuteron Multiple Scattering Theory

The multiple scattering calculation to be described is an extension of the high energy Glauber theory incorporating the complete spin structure and the corrections to the eikonal and fixed scatterer approximations. It turns out that the binding, recoil and Fermi motion corrections can be neglected in the projectile propagator of the double scattering term leaving the non-eikonal correction as the dominant one[1-7]. The inputs to this parameter free approach are the nucleon-nucleon (NN) amplitudes and the deuteron wave function. They are described in sections 1.C.1. and 1.C.2. respectively.

Proton-deuteron scattering provides the simplest example of a few body collision. The proton-deuteron scattering amplitude takes the form:

$$F = F_s + F_d \qquad (1\text{-}1)$$

where F_s and F_d are the single and double scattering contributions respectively and are represented in terms of relativistic multiple scattering diagrams. The assumption that the multiple scattering expansion only has single and double scattering terms neglects the contributions of "reflections". This has been done because the triple and higher order scatterings would require large angle or backward propagation of the projectile which is unlikely at these energies since the NN amplitudes are strongly peaked in the forward

direction at intermediate energies. The "local" off-shell extrapolation of the NN amplitudes is assumed. That is, they depend only on the momentum transfer.

The calculation of all the spin observables is done in the deuteron Breit frame[1-7]. This is the coordinate system in which the deuteron reverses its three-momentum (q) in the scattering. This frame minimizes the velocities of the nucleons within the deuteron justifying to a certain degree the use of the non-relativistic bound state wave function for the deuteron. See figure 1-1 for the definition of the reference axes in the Breit frame.

The single scattering amplitude, which is composed of a proton-proton (pp) and a proton-neutron (pn) term has the form:

$$F_S = S(\vec{Q}/2)[f(\vec{Q}) + g(\vec{Q})]M/m \qquad (1\text{-}2)$$

where

$$S(q) = \int d^3q' \tilde{\Psi}^*(\vec{q}' + \vec{q})\Psi(\vec{q}')/(2\pi)^3 \qquad (1\text{-}3)$$

where S(q) is the deuteron form factor, M is the mass of the deuteron composed of two nucleons of mass m and $\vec{Q}$ is the three-momentum transfer. The NN amplitudes f and g describe the scattering of the off-mass-shell nucleons. The double scattering amplitude, F_d, is described in ref 1-7.

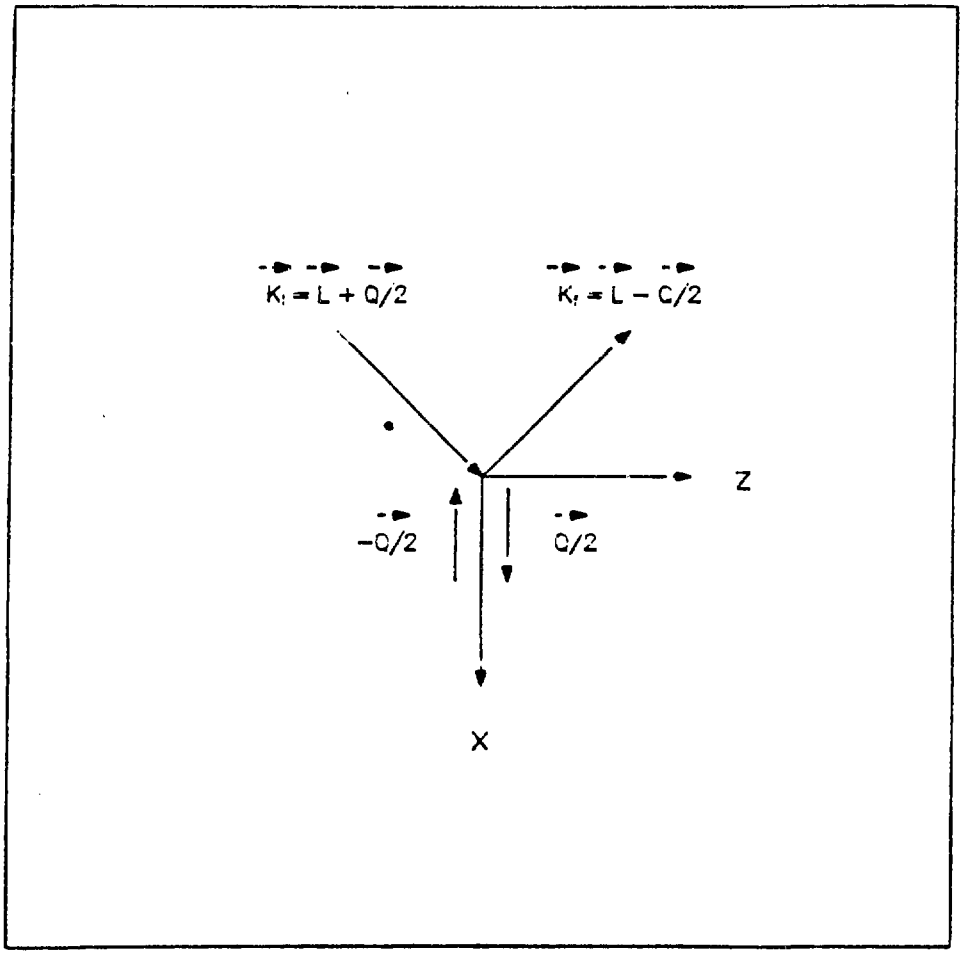

FIGURE 1–1

Breit Frame

The full pd scattering amplitude, F, in the deuteron Breit frame is composed of a complete set of spin-1 hermitian operators and the spin 1/2 Pauli operators. The deuteron spin space is spanned by 9 independent spin-1 operators and 4 Pauli operators span the proton spin space. For the most general form of F(Q), see sections 1.D. and A.10.

The NN amplitudes were taken from the phase shift analysis of ref. 1-4. The components of the pd amplitude (subamplitudes) in the multiple scattering formalism are most conveniently calculated in the deuteron Breit frame. Even though it is possible to perform Lorentz transformations on the amplitudes, it is simpler to calculate the observables in the Breit frame and then transform them to the lab system. This is done by relativistic spin transformations (Wigner rotations). For details of the Wigner rotations see section A.11.

The general pd spin observables, $C(\alpha,\mu;\beta,\nu)$, have the form[1-7]:

$$I_0 C(\alpha,\mu;\beta,\nu) = \mathrm{Tr}\{\hat{F}\sigma_\alpha \hat{O}_\mu \hat{F}^+ \sigma_\beta \hat{O}_\nu\} \qquad (1\text{-}4)$$

where $\sigma_0 = 1$ and σ_α, $\alpha = x,y,z$ are the Pauli matrices and $\hat{O}_\upsilon$ are the deuteron spin-1 operators (see sections 1.D. and A.10.). Here α, μ, β, ν denote the initial proton, the initial deuteron, the final proton and final deuteron spin directions respectively. Note that F is the full pd scattering amplitude and is described in section 1.D. The quantity

$$I_o = Tr(\hat{F}\hat{F}^+) \tag{1-5}$$

is proportional to the unpolarized differential cross section. The proton spin-rotation parameters measured in this experiment take the form[1-7]:

$$I_o C(\alpha,0;\beta,0) = 2\sum_{\rho\sigma}{}' \Omega_{\rho\sigma} Re[\delta_{\alpha\beta}(F^o_\rho F^o_\sigma - \sum_n F^n_\rho F^{n*}_\sigma) + 2F^\alpha_\rho F^{\beta*}_\sigma] \tag{1-6}$$

and the proton polarization, which is equal to the proton analyzing power, is given by:

$$I_o C(y,0;0,0) = 2\sum_{\rho\sigma}{}' Re(F^o_\rho F^{y*}_\sigma) = 2Re[6F^o_o F^{y*}_o + 4F^o_y F^{y*}_y + 4(F^o_{xx}F^{y*}_{xx} + F^o_{yy}F^{y*}_{yy}) - 2(F^o_{xx}F^{y*}_{yy} + F^o_{yy}F^{y*}_{xx})/3] \tag{1-7}$$

where

$$\Omega_{\rho\sigma} = Tr(\hat{O}_\rho \hat{O}_\sigma) \tag{1-8}$$

Here these F's are various components of the pd scattering amplitude (see section I.D.). The spin observables in the Breit frame have several symmetry properties. From parity invariance,

$$C(\alpha,\mu;\beta,\nu) = 0 \text{ (if } n_x+n_z \text{ is odd)} \tag{1-9}$$

where n_x and n_z are the number of times x and z appear in the

subscripts α, μ, β, ν respectively. From time reversal invariance, it follows that:

$$C(\alpha,\mu;\beta,\nu) = (-1)^{n_x} C(\beta,\nu;\alpha,\mu) \qquad (1\text{-}10)$$

This provides a systematic check on the data, see section 3.K.1. The derivations of eqns 1-9 and 1-10 are given in section A.10.

I.C.1. Nucleon - Nucleon Amplitude

The nucleon-nucleon (NN) amplitude can be parameterized as follows[1-7]:

$$f_\ell = \alpha_\ell(q) + \beta_\ell(q)\hat{\sigma}_y^1\hat{\sigma}_y^2 + i\gamma_\ell(q)(\hat{\sigma}_y^1+\hat{\sigma}_y^2) + \delta_\ell(q)\hat{\sigma}_x^1\hat{\sigma}_y^2 + \varepsilon_\ell(q)\hat{\sigma}_z^1\hat{\sigma}_z^2 \quad (1\text{-}11)$$

where the index ℓ = p,n refers to the proton-proton and proton-neutron amplitudes respectively, and $\hat{\sigma}^1$ and $\hat{\sigma}^2$ are the Pauli spin operators of the two nucleons and q is the momentum transfer. The x,y,z coordinate system is defined in eqn (1-14). The NN amplitudes are usually given in the NN center of mass system[1-4]. At the present time the NN (especially the n-p) amplitudes are not well known at 800 MeV. The amplitudes α and γ represent respectively the spin independent and spin orbit components while β, δ and ε represent the double spin-flip components.

The NN amplitudes used in the multiple scattering theory of Bleszynski et. al. were taken from the (FA-83) phase shift analysis of Arndt and Roper[1-4]. We have participated in measuring the spin transfer observables for pp elastic scattering at the EPB area of LAMPF at 600, 650, 700, 750 and 800 MeV incident proton energies[1-35,36,37]. For more details on these pp scattering measurements see section A.7. As a result of this work together with several other experiments, the T = 1 (pp) NN phase shift analysis will soon be completely determined up to 800 MeV. As seen in eqn (1-11), the NN amplitude has 5 complex components and thus requires 9

independent observables to determine it up to a phase. In practice even more are required[1-5,6].

1.C.2. Deuteron Wave Functions

Since the deuteron is a spin 1 object, the internal wave function for it in a magnetic substate m (m = ±1,0) relative to an axis of quantization $\hat{p}$ can be written as[1-17]:

$$\Psi_{\hat{p},m}(\vec{r}) = (4\pi)^{-1/2} r^{-1} [u(r) + 8^{-1/2} S_{12} w(r)] |\hat{p},m\rangle \qquad (1\text{-}12)$$

where $|\hat{p},m\rangle$ is a spin-1 spinor, u and w are the s- and d-state radial wave functions, and S_{12} is the tensor operator:

$$S_{12} = 3(\vec{\sigma}_1 \cdot \hat{r})(\vec{\sigma}_2 \cdot \hat{r}) - \vec{\sigma}_1 \cdot \vec{\sigma}_2 \qquad (1\text{-}13)$$

Reid soft core wave functions[1-38] were used in the multiple scattering calculation[1-7] outlined in this chapter. The radial wave function used is 94% s-state and 6% d-state.

1.D. Spin 1/2 - Spin 1 Scattering Amplitude

The most general form of the spin 1/2 - spin 1 elastic scattering amplitude can be obtained using symmetry arguments. This scattering amplitude must be rotationally invariant and also invariant under parity and time reversal transformations. Consider the following coordinate system (see figure 1-2):

$$\hat{x} = \vec{k}_i - \vec{k}_f$$

$$\hat{y} = \vec{k}_i \times \vec{k}_f \qquad (1\text{-}14)$$

$$\hat{z} = \vec{k}_i + \vec{k}_f$$

Using the parity and time reversal properties given in table 1, the most general scattering amplitude is constructed using the spin 1/2 Pauli operators $\hat{\sigma}_o$, $\hat{\sigma}_x$, $\hat{\sigma}_y$, $\hat{\sigma}_z$, the spin 1 vector operators $\hat{1}$, $\hat{J}_x$, $\hat{J}_y$, $\hat{J}_z$ and the five independent spin 1 quadrupole operators $\hat{Q}_{ik}$, given in eqn (1-16). The scattering amplitude has the form, also see section A.10.[1-1]:

$$\hat{F} = \hat{F}^o\hat{\sigma}_o + \hat{F}^x\hat{\sigma}_x + \hat{F}^y\hat{\sigma}_y + \hat{F}^z\hat{\sigma}_z \qquad (1\text{-}15)$$

$$\hat{F}^o = F^o_o\hat{1} + F^o_y\hat{J}_y + F^o_{xx}\hat{Q}_{xx} + F^o_{yy}\hat{Q}_{yy}$$

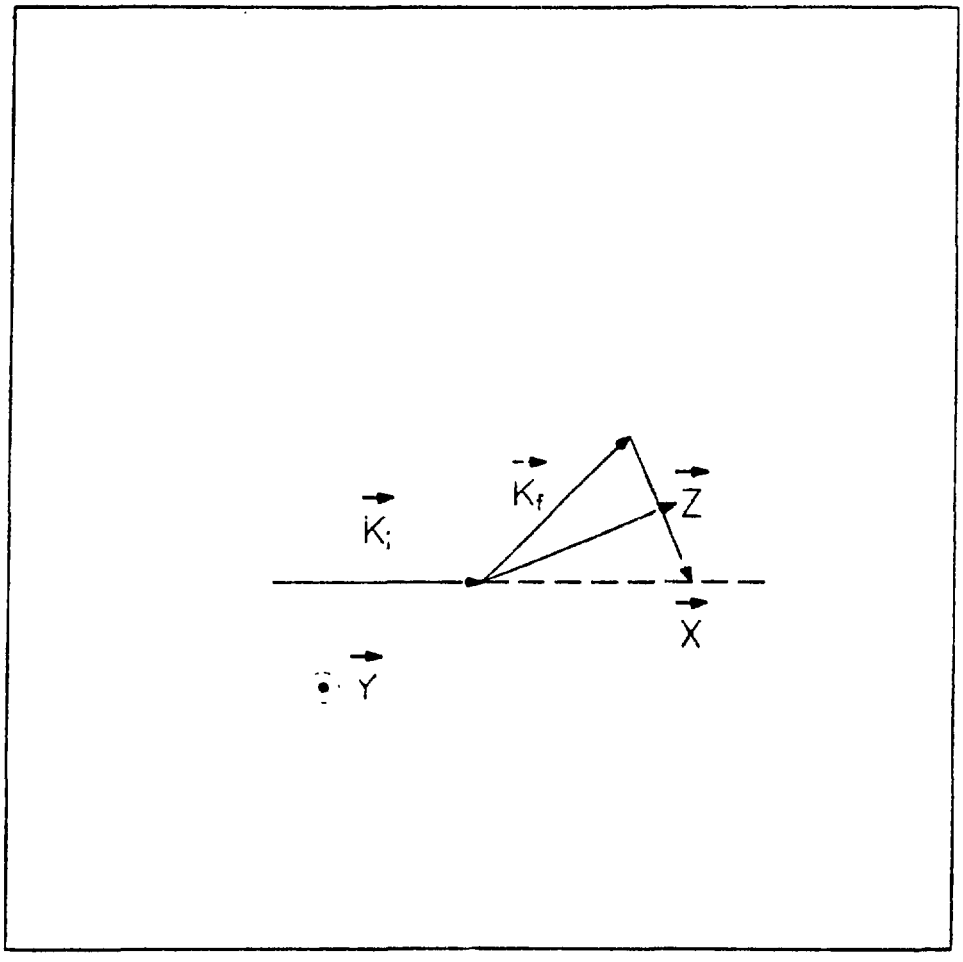

FIGURE 1–2

Coordinate System

$$\hat{F}^x = F^x_x \hat{J}_x + F^x_{xy} \hat{Q}_{xy}$$

$$\hat{F}^y = F^y_o \hat{1} + F^y_y \hat{J}_y + F^y_{xx} \hat{Q}_{xx} + F^y_{yy} \hat{Q}_{yy}$$

$$\hat{F}^z = F^z_z \hat{J}_z + F^z_{yz} \hat{Q}_{yz}$$

where

$$\hat{Q}_{ik} = 1/2\ (\hat{J}_i \hat{J}_k + \hat{J}_k \hat{J}_i) - 2/3(\delta_{ik} \hat{1}) \qquad (i,k = x,y,z) \qquad (1\text{-}16)$$

and δ_{ik} is the Kronecker-delta function.

There is no F^o_{zz} term because

$$\hat{Q}_{zz} = -\ (\hat{Q}_{xx} + \hat{Q}_{yy}) \qquad (1\text{-}17)$$

so $\hat{Q}_{zz}$ is not independent. In fact, there are 9 independent spin 1 operators, following the same $[(2J + 1)^2 - 1] + 1$ rule as the 4 independent Pauli spin 1/2 operators. For more details see ref. 1-39. In order to completely determine the p-d scattering amplitude up to a phase, 23 independent measurements (observables) are required since it is made up of 12 complex subamplitudes (eqn 1-15). And in practice, even more are necessary, as is well known from the pp system[1-5,6]. The current status of the p-d observables measured was

discussed in section 1.B. The construction of the most general form of the pd scattering amplitude is discussed in section A.10.

Table 1 - Parity and Time Reversal Properties

Vectors and Operators	Parity	Time Reversal
$\vec{k}_i$	$-\vec{k}_i$	$-\vec{k}_f$
$\vec{k}_f$	$-\vec{k}_f$	$-\vec{k}_i$
$\vec{x} = \vec{k}_i - \vec{k}_f$	$-\vec{x}$	$\vec{x}$
$\vec{y} = \vec{k}_i \times \vec{k}_f$	$\vec{y}$	$-\vec{y}$
$\vec{z} = \vec{k}_i + \vec{k}_f$	$-\vec{z}$	$-\vec{z}$
$\vec{\sigma}$	$\vec{\sigma}$	$-\vec{\sigma}$
$\vec{J}$	$\vec{J}$	$-\vec{J}$
$\hat{Q}$	$\hat{Q}$	$\hat{Q}$
$\hat{\sigma}_x = \vec{\sigma}\cdot\vec{x}$	$-\hat{\sigma}_x$	$-\hat{\sigma}_x$
$\hat{\sigma}_y = \vec{\sigma}\cdot\vec{y}$	$\hat{\sigma}_y$	$\hat{\sigma}_y$
$\hat{\sigma}_z = \vec{\sigma}\cdot\vec{z}$	$-\hat{\sigma}_z$	$\hat{\sigma}_z$
$\hat{J}_x = \vec{J}\cdot\vec{x}$	$-\hat{J}_x$	$-\hat{J}_x$
$\hat{J}_y = \vec{J}\cdot\vec{y}$	$\hat{J}_y$	$\hat{J}_y$
$\hat{J}_z = \vec{J}\cdot\vec{z}$	$-\hat{J}_z$	$\hat{J}_z$
$\hat{Q}_{xx} = \vec{x}^T\hat{Q}\vec{x}$	$\hat{Q}_{xx}$	$\hat{Q}_{xx}$
$\hat{Q}_{yy} = \vec{y}^T\hat{Q}\vec{y}$	$\hat{Q}_{yy}$	$\hat{Q}_{yy}$
$\hat{Q}_{xy} = \vec{x}^T\hat{Q}\vec{y}$	$-\hat{Q}_{xy}$	$-\hat{Q}_{xy}$
$\hat{Q}_{yz} = \vec{y}^T\hat{Q}\vec{z}$	$-\hat{Q}_{yz}$	$\hat{Q}_{yz}$
$\hat{Q}_{zx} = \vec{z}^T\hat{Q}\vec{x}$	$\hat{Q}_{zx}$	$-\hat{Q}_{zx}$

1.E. Proton-Deuteron Spin Dependent Observables

In the center of mass system, the spin rotation parameters can be expressed as

$$D_{\alpha\beta} = Tr\{\sigma_\alpha F \sigma_\beta F^+\}/I_o \qquad (1\text{-}18)$$

where I_o is unpolarized differential cross section and F is the p-d scattering amplitude given in section 1.D. Note that the proton spin rotation parameters of eqn 1-18 are a special case of the general pd spin observables given in eqn 1-4, where the deuteron spin operators, $\hat{O}_\mu$ and $\hat{O}_\nu$ are $\hat{1}$. This is the case where the deuteron target is unpolarized and the final state deuteron polarization is not measured.

$$I_o = T\{FF^+\} \qquad (1\text{-}19)$$

The depolarization parameters are defined as:

$$D_j = Tr\{F_j{}^+ F_j\}/I_o \quad (j = o, x, y, z) \qquad (1\text{-}20)$$

and the induced polarization ($P = A_y$ using time reversal, see section A.10.) is given by

$$P = 2Re\{Tr(F_o{}^+ F_y)\}/I_o \qquad (1\text{-}21)$$

The depolarization parameters, D_j, in the Breit frame can be expressed as a linear combination of the experimental spin rotation observables in the particle helicity laboratory system (see below), they have the following form (see section A.11.):

$$D_o=\frac{1}{4}\,[1 + D_{nn} + \cos(\chi - \chi')(D_{ss} + D_{\ell\ell}) + \sin(\chi - \chi')(D_{s\ell} - D_{\ell s})]$$

$$D_x=\frac{1}{4}\,[1 - D_{nn} + \cos(\chi + \chi')(D_{ss} - D_{\ell\ell}) - \sin(\chi + \chi')(D_{s\ell} + D_{\ell s})]$$

$$D_y=\frac{1}{4}\,[1 + D_{nn} - \cos(\chi - \chi')(D_{ss} + D_{\ell\ell}) - \sin(\chi - \chi')(D_{s\ell} - D_{\ell s})] \quad (1\text{-}22)$$

$$D_z=\frac{1}{4}\,[1 - D_{nn} - \cos(\chi + \chi')(D_{ss} - D_{\ell\ell}) + \sin(\chi + \chi')(D_{s\ell} + D_{\ell s})]$$

where

$$\chi = \theta_B/2 + \alpha, \quad \chi' = -(\theta_B/2 + \alpha) + \theta_L \quad (1\text{-}23)$$

where θ_B, $\bar{\theta}_L$ and α are the scattering angle of the scattered proton in the Breit system, the deuteron scattering angle in the anti-laboratory system and the angle between the velocities of the Breit frame and the laboratory system seen from the anti-laboratory system. The anti-laboratory system is the frame in which the initial proton is at rest[1-7]. The derivation of these relativistic transformations (Wigner rotations) is given in section A.11. In trying to to completely determine the components, F_j, of the p-d scattering amplitude, one can include measurements of the unpolarized

differential cross section, I_o, (see eqn 1-19) and the Wolfenstein parameters[1-8,9](eqns 1-18,22). In addition, some deuteron spin observables are required (at least 23 independent measurements). See section 4.A. for the physical interpretation of these proton spin observables and their relationship in the particle helicity laboratory coordinate system.

Figure 1-3 shows the particle helicity frame. As seen, it is defined in terms of two orthogonal sets of coordinate axes, based on the initial and final proton momenta, $\vec{k}_i$ and $\vec{k}_f$. For both sets of right-handed axes, the $\hat{y}$-direction is defined as the cross product of $\vec{k}_i$ and $\vec{k}_f$. The axes are defined as follows:

$$\begin{aligned}
&\vec{n} = \vec{n}' = \vec{k}_i \times \vec{k}_f && \text{(normal)} \\
&\vec{\ell} = \vec{z} = \vec{k}_i && \text{(initial longitudinal)} \\
&\vec{s} = \vec{x} = \vec{n} \times \vec{\ell} && \text{(initial sideways)} \\
&\vec{\ell}' = \vec{z}' = \vec{k}_f && \text{(final longitudinal)} \\
&\vec{s}' = \vec{x}' = \vec{n}' \times \vec{\ell}' && \text{(final sideways)}
\end{aligned} \qquad (1\text{-}24)$$

Note that the final proton axes are denoted by the primed letters.

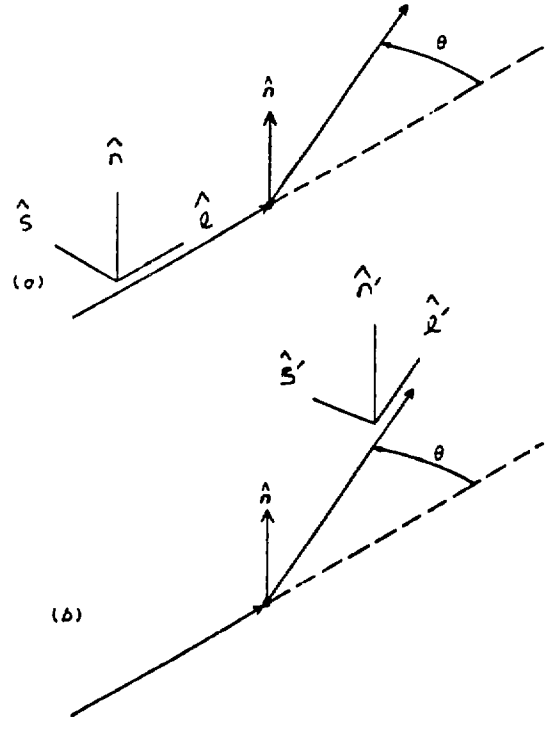

FIGURE 1-3

Projectile Helicity Frame

2.A. The Accelerator and Polarized Proton Beam

The experiment was done at the Clinton P. Anderson Meson Physics Facility (LAMPF) using the High Resolution Spectrometer (HRS). The LAMPF accelerator[2-1,2] (roughly 0.5 miles long) accelerates two beams simultaneously, protons (H^+) and negative hydrogen ions which are either polarized (P^-) or unpolarized (H^-). P^- or H^- beams from 300 to 800 MeV are available in steps of about 50 MeV. A Lamb-Shift ion source is used to produce the polarized proton beam.

LAMPF uses 750 KeV Cockroft Walton injectors which feed high intensity H^+, P^- or H^- beams to the main accelerator sections. The next stage is a 201.25 MHz Alvarez drift tube linac (61.7 meters long) which accelerates the particles from 750 KeV up to 100 MeV. Then the beams go through a transition region into a section made up of 44 side-coupled wave cavities which bring the beams up to their final energy of 800 MeV. This stage is 731 m long (~15 feet underground) and uses 805 MHz RF to accelerate the particles.

The beam structure is shown in figure 2-1. At 800 MeV, it consists of macropulses 750 μs wide which come at 120 Hz. The micropulses within a macropulse are 805 MHz RF. This beam structure results in a 9% duty factor at 800 MeV.

The P^- ions are magnetically separated from the simultaneously accelerated H^+ ions in the beam switchyard (see figure 2-2). The P^- ions are bent into Line X while the H^+ ions continue towards the production targets in Line A where they produce secondary beams

FIGURE 2–1

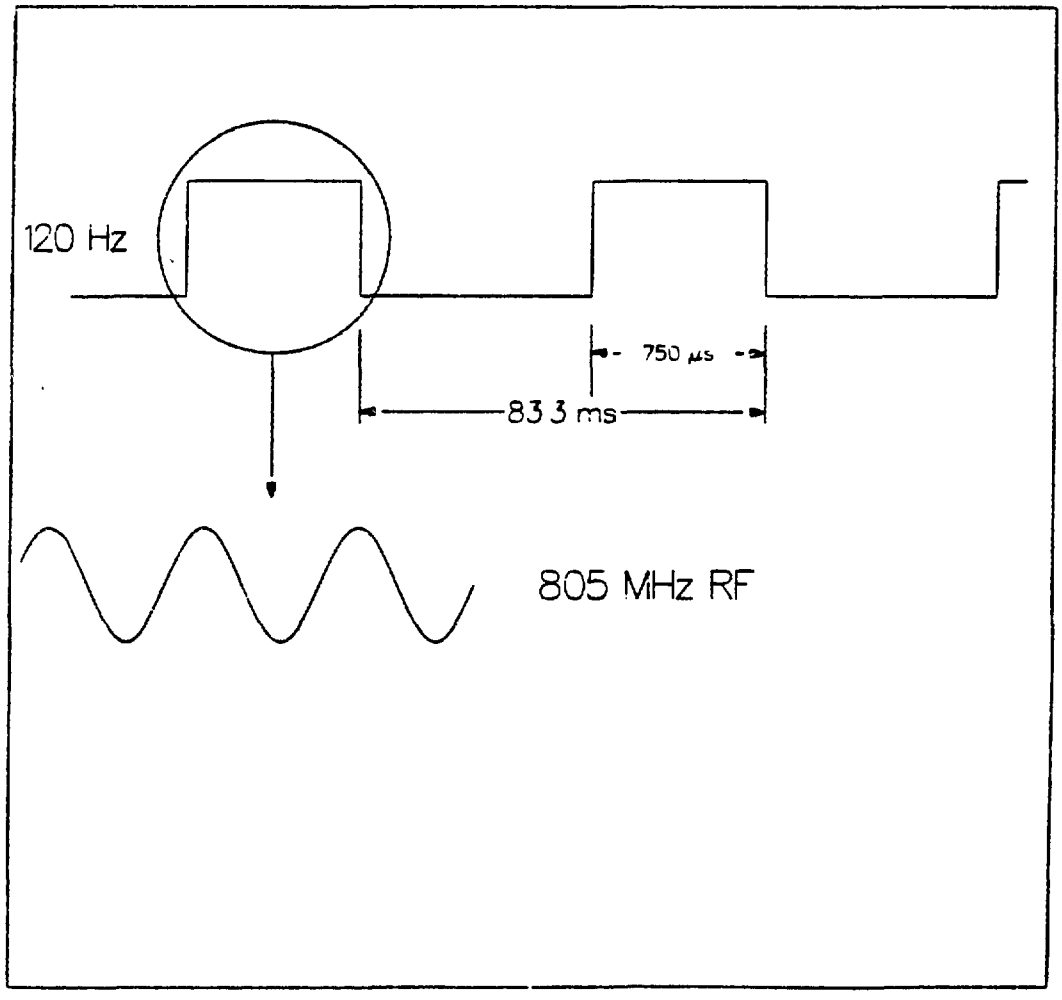

LAMPF beam structure

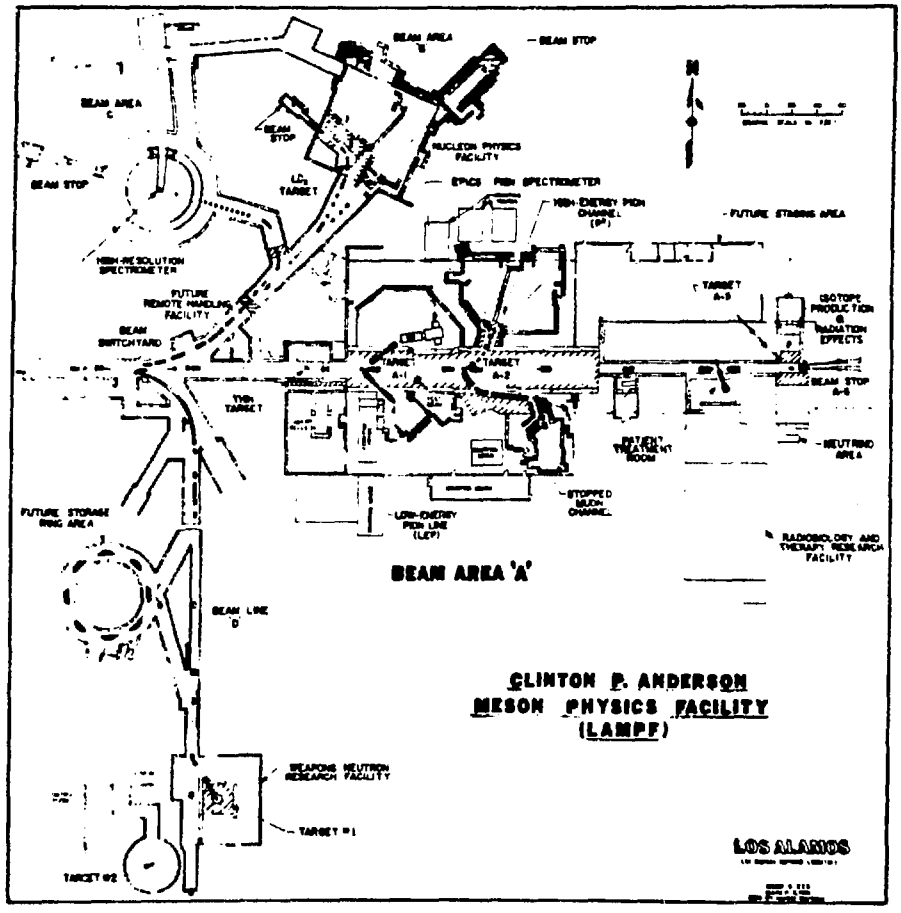

FIGURE 2- 2

LAMPF experimental areas

(mesons , muons, neutrinos, etc.). In Line X, strippers (foils and wires) are used to strip (P^- to polarized H^+) the fraction of the beam going to HRS through Line C while the unstripped part of the beam (P^-) continues on into Line B where it is later stripped for areas EPB and BR. Several bending and quadrupole magnets in Line C are then used to steer and focus the proton beam into the HRS area (see figure 2-3). In addition, several mechanical jaws (vertical and horizontal) can be used to regulate the beam spot size on target, which was approximately 2.5 cm - vertically and 3 mm - horizontally for this experiment. Between 5pA and 1.5nA polarized proton beam intensity was used in this experiment. A beam line polarimeter (10 meters upstream of the target) was used to measure the beam polarization, as described in section 3.B.

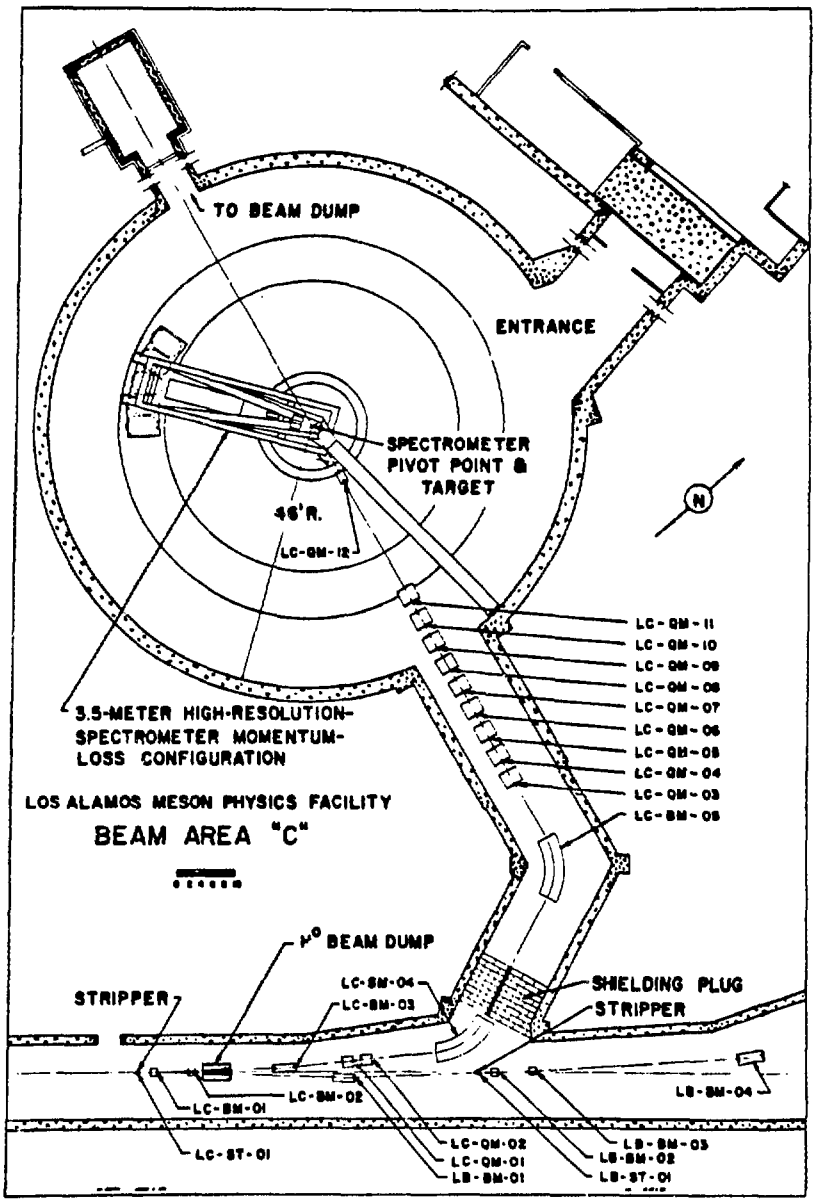

FIGURE 2-3

LAMPF area C

2.B. The High Resolution Spectrometer (HRS)

The HRS is a proton spectrometer employing a vertical Quad - Dipole - Multipole - Dipole (QDMD) magnet system as shown in figure 2-4. The multipoles were not used in this experiment. The HRS was designed[2-2,3] to give an energy resolution, $\delta E/E$, of 2.4×10^{-5} FWHM (equivalent to 30 KeV for 800 MeV protons), an angular resolution of ± 1 mr, a momentum bite of 2% and a solid angle of 3.6 msr. In this experiment the scattering angle acceptance was roughly ±1 degree. The energy resolution obtained in this experiment is described in section 3.D.

The HRS is a 14 meter radius hemispherical dome supported by a 4.5 meter high cylindrical section. The dome is covered by 3 meters of earth fill used for shielding.

The QDMD system consists of a large aperture quadrupole lens (HS-QM-01) followed by a 75 degree bend dipole (HS-BM-01), a 12 element multipole and another 75 degree bend dipole (HS-BM-02).

The HRS optics[2-3] are point-to-point in the dispersion (vertical-momentum) direction and point-to-parallel in the non-dispersion (horizontal) direction. This means that basically the vertical position at the focal plane is proportional to the outgoing proton momentum while the horizontal position at the focal plane corresponds to the horizontal component of the scattering angle at the target. The detectors at the focal plane are described in section 2.B.1.

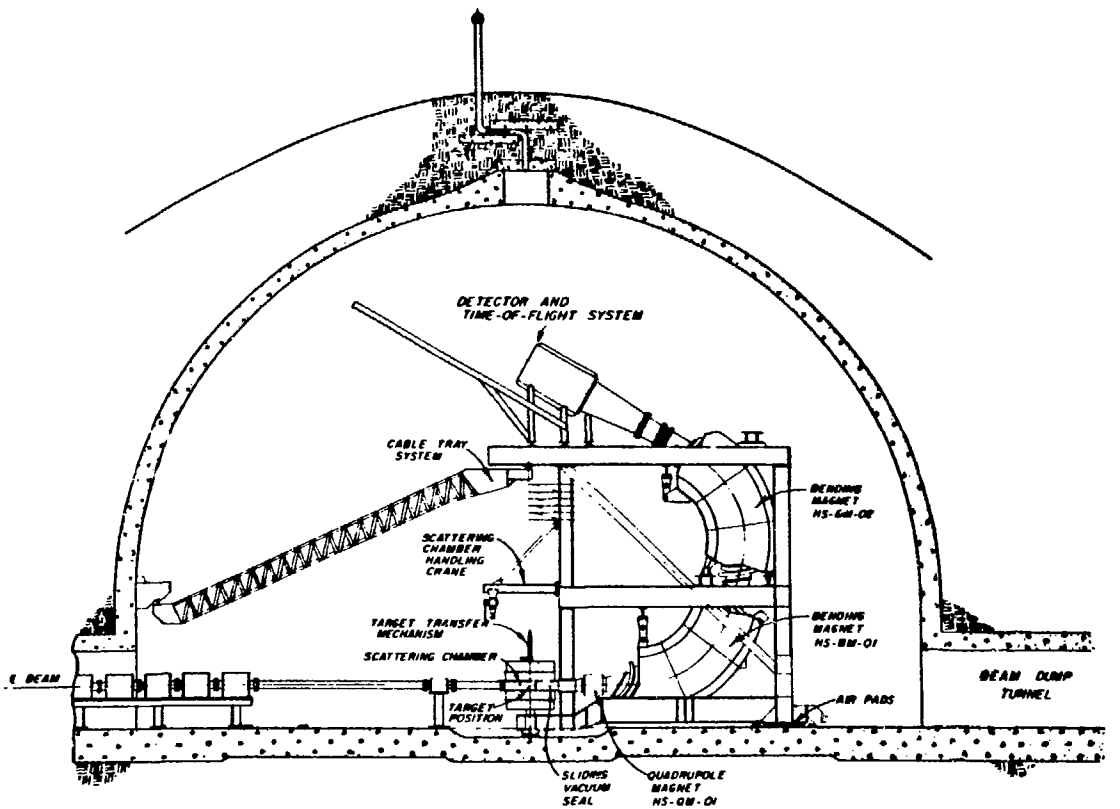

FIGURE 2-4

High Resolution Spectrometer (HRS)

2.B.1. The HRS Detectors and Focal Plane Polarimeter

The Focal Plane Polarimeter (FPP) is used to determine all of the information about the proton scattered at the deuterium target (scattering angle, momentum , position scattered, polarization, missing mass, etc.). All of the HRS detectors are located up on the focal plane, see figure 2-4. In this experiment, the detector system consisted of four Multiwire Drift Chambers[2-4,5] (MWDC) and four scintillators. The MWDCs are used to obtain the positions in space of the particle trajectories. They have a spacial resolution of 0.25 mm (FWHM) and can handle instantaneous particle rates of ~1 MHz[2-4,5]. The scintillators have temporal resolution of ~1 ns. They can typically handle up to ~500 KHz particle rates. The scintillators are used for particle timing and particle identification.

The HRS detector system is shown in figure 2-5. As seen in the figure, the two front chambers, C12 and C34, have an active area of 10 x 60 cm^2 and are separated by 0.5 meters. The two back chambers, C56 and C78, are 60 x 60 cm^2 and separated by 0.25 meters. All MWDCs employ a fast delay-line readout (2.5 ns/cm), both ends of which are sent through leading edge discriminators to fast buffered LRS 2250 Time-to-Digital-Converters (TDC). Each chamber consists of four High Voltage (HV) anode planes, two X and two Y with 8 mm wire spacing offset by 4 mm. Using closely spaced pairs of drift planes in each direction gives left-right identification of drift positions in each direction. Mylar ground planes separate the anode wire

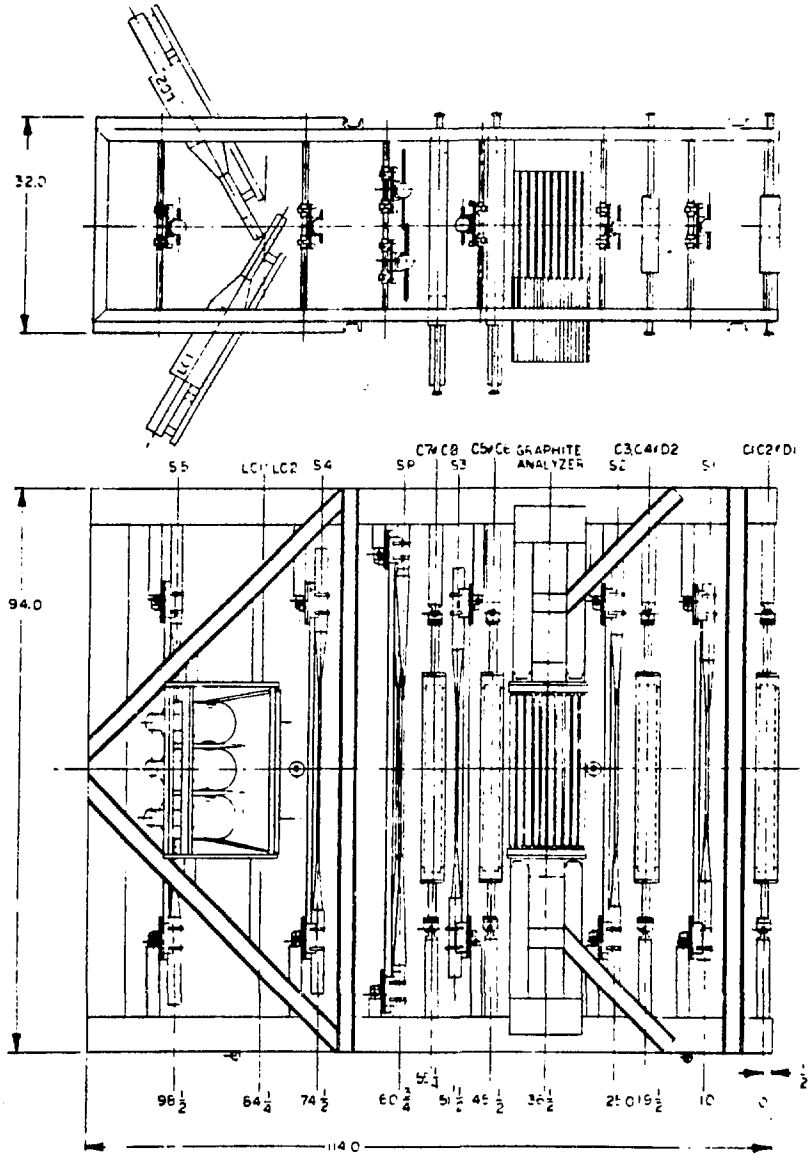

FIGURE 2-5

HRS detector system

planes. The particle position information is obtained using the TDC time differences and sums between the two ends of the delay line.

The front scintillators, S1 and S2, are 10 x 56 cm^2 while the back scintillators, SP1 and SP2, are 38 x 76 cm^2 overlapping by about 3 cm. Each scintillator has a phototube at the top and bottom and gives signals which are sent to fast buffered LRS 2550 Analog-to-Digital-Converters (ADC) for pulse height information and through leading edge discriminators to TDCs for timing. Another scintillator, S_x, 10 x ~30 cm^2, was placed downstream of S1 (between S1 and S2, as shown in fig. 2-5) and was used to limit the focal-plane acceptance in the vertical (momentum) direction in order to increase the fraction of useful events on tape.

The carbon analyzer[2-6,7], used to produce nuclear scatterings in order to measure the polarization of the outgoing proton, consists of nine slabs of graphite (1.78 gm/cm^3 density) each 41 x 41 3 cm^3 in size. Between 7 and 9 slabs were used in order to keep the multiple scattering angle roughly constant - see section 3.G. With this FPP setup, scattering angles of up to 21 degrees in the carbon analyzer are detected for rays at the center of the FP. The FPP has a momentum acceptance of 30 MeV at 800 MeV. In this double scattering process, the FPP is about 15% efficient in obtaining useful scattering events for measuring the polarization of the protons scattered at the deuterium target. Most of the outgoing protons undergo small angle ($< 2.5^o$) multiple Coulomb scatterings in the

carbon and give no polarization information since multiple Coulomb scattering does not contain any spin dependence.

2.C. Data Acquisition and Software

The data was acquired using Computer Automated Measurement and Control Standard IEEE 583 (CAMAC) fast digital electronics. Standard LeCroy Research Systems (LRS) modules were used. For the particle position information, the multiwire drift chamber (MWDC) delay line signals were sent through discriminators to time to digital converters (TDC). The timing signals from the scintillators go through discriminators to TDCs. Scintillator pulse height signals go directly to analog to digital converters (ADC). As described in section 2.B.1., for good events (scintillator coincidences), the raw data, which consists of these TDC and ADC signals, are sent to the computer.

Basically all other quanities, such as momentum, scattering angle, position in the target in which the particle scattered, missing mass, proton polarization, etc., are calculated in the software and are used to determine the proton spin observables for a particular reaction. A Digital Electronics Corp. (DEC) PDP 11/45 mini-computer with associated peripherals, including a microprogrammable branch driver (MBD), interfaced to the 11/45, is used to take the data. The software is a set of fortran programs which use the raw data to calculate all other quanitiies of interest.

The system can handle a data rate of 1200 events/second. This is the maximum rate given the 9% duty factor of the LAMPF accelerator at 800 MeV. The MBD becomes inefficient at rates much higher than 1200 events per second.

The MBD (microprocesser) is used to do fast calculations on the data in order to put crude cuts on it before it goes to the computer and is written to magnetic tape. It is used to maximize the fraction of good events written to tape. The main cuts done in the MBD are cuts in the polar scattering angle in the carbon (see section 3.G.) and the position differences in the MWDCs. Typically, 10-15% of the events going into the MBD are written to tape in this type of focal plane polarimeter experiment at the HRS. For those events written to tape, all of the raw data is put on tape. During data acquisition, the computer calculates parameters on-line when it has time. Therefore it is possible to get a rough idea of what the data looks like while the experimental data is being taken.

2.D. The Electronics

The electronics is made up of discriminators, time-to-digital converters (TDC), analog-to-digital converters (ADC), logic units (and, or gates), fan in/outs etc. The TDCs are used to encode (digitize) time signals; the ADCs digitize pulse height signals. The discriminators take a pulse of a given threshold and put out a standard square-like pulse. The logic units perform operations on discriminator output signals. The fanouts are used to take an input signal and produce several identical outputs. The fast digital electronics used in the HRS area is buffered CAMAC modules made by LRS. A schematic diagram of the fast-logic signal electronics is given in fig. 2-6.

A system trigger is defined as an event (scintillator coincidence) when the computer is not busy during a beam gate and is used to determine when the system will take data. In this experiment an event is defined as a coincidence between the scintillators S1, S_X, S2 and SP as shown in fig. 2-5. The trigger is built up using LRS621 and LRS821 gated discriminators, LRS624, LRS465 and LRS365 logic units, fanouts and delay boxes. The TDCs and ADCs plug into camac crates. The TDCs and ADCs are gated by the trigger. These buffered TDCs and ADCs have 512 channels. When the Camac buffer is filled (32 events) it dumps the raw data through a fast microprocessor to the PDP 11/45 computer.

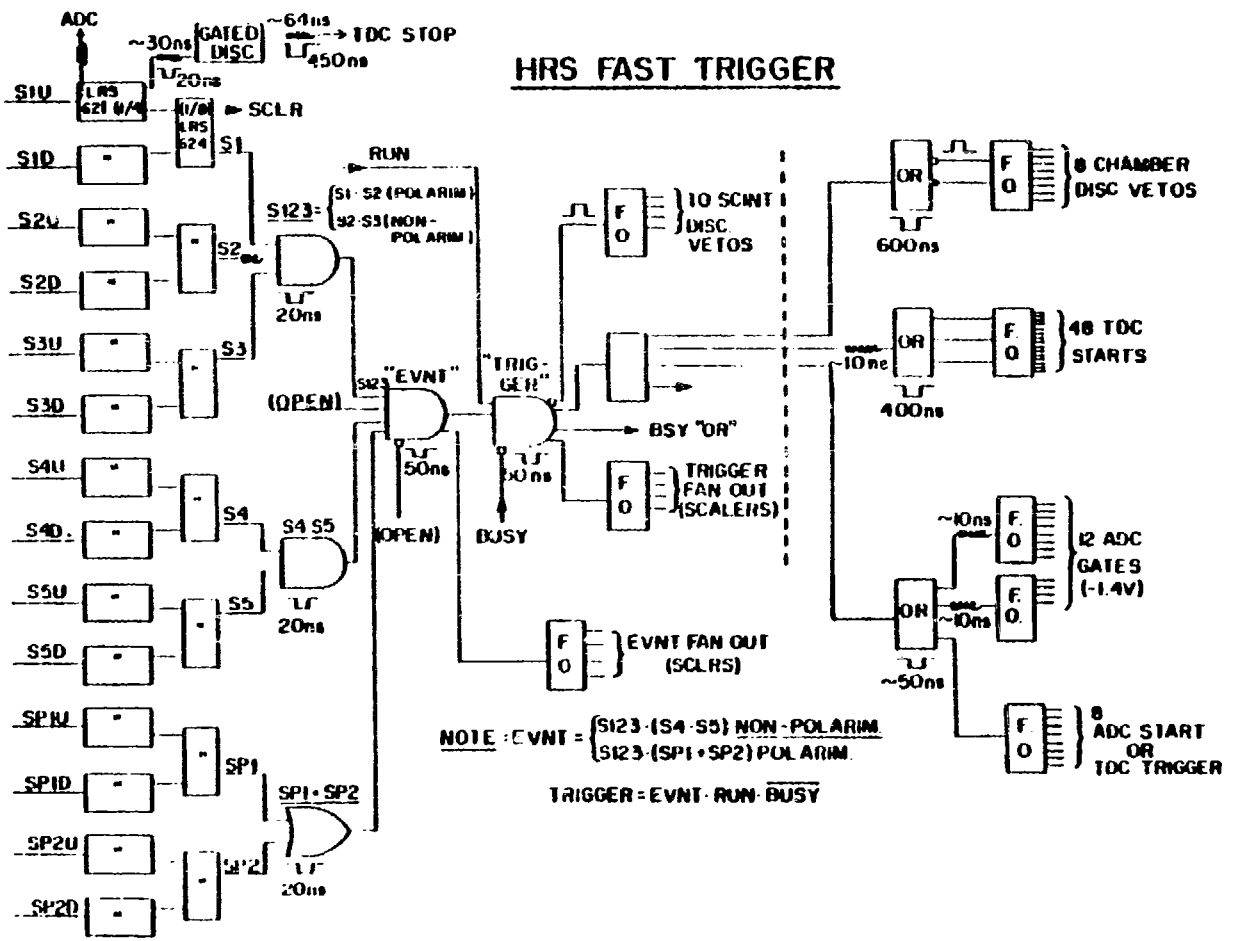

FIGURE 2-6

HRS fast trigger electronics

The slow logic electronics is shown in fig. 2-7. This is used for constructing a beam gate. A beam gate occurs only during the small fraction of time (9% duty factor) in which protons impinge on the target and is used in the coincidence making up the system trigger. As seen in fig. 2-7, a beam gate is defined as the coincidence between a run gate and a polarized signal.

The same type of electronics is used to build up the left/right and up/down yields from the polarimeter in order to calculate the beam polarization. For more details, see ref. 3-1.

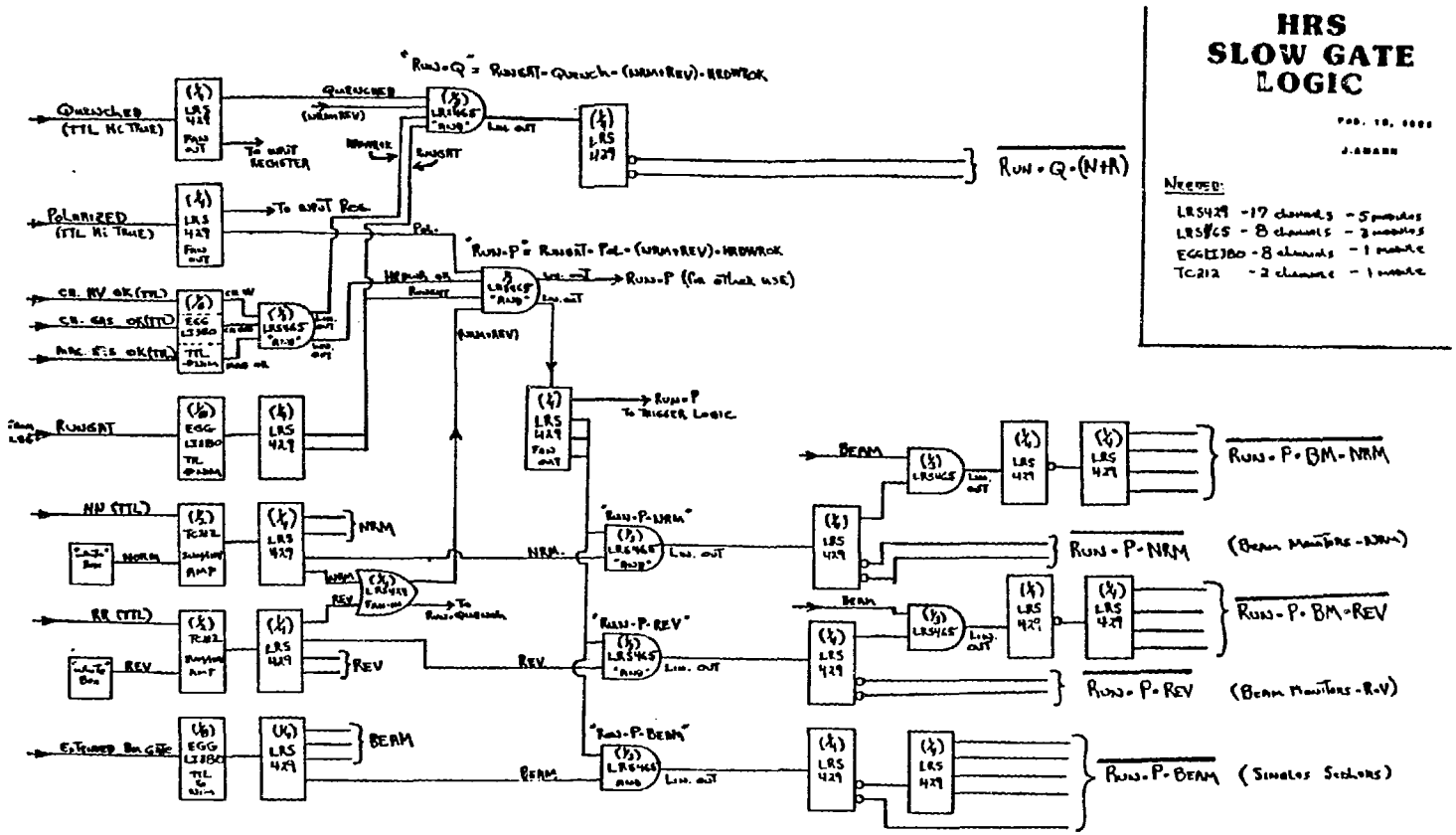

FIGURE 2-7

HRS slow trigger electronics

3.A. The Wolfenstein Parameters and Analyzing Power

In this experiment the proton spin observables measured are the Wolfenstein parameters[1-8,9] and the analyzing power. The Wolfenstein paameters use a polarized proton beam and require the measurement of the proton polarization after the scattering. The outgoing proton spin direction is precessed due to the magnetic field of the HRS. The precession angle of the proton polarization with respect to its momentum is given by:

$$\chi = \gamma(g/2-1)\alpha \simeq 269\alpha \qquad (3\text{-}1)$$

γ is the Lorentz factor, g/2 is the proton magnetic moment (2.793) and α is the bend angle in the HRS (150^0). A derivation of eqn 3-1 is given in section A.9. Data are taken for both normal and reverse beam polarizations. For $\hat{n}$-type beam polarization, normal corresponds to spin up and reverse is spin down. $PN^+(FP)$ and $PN^-(FP)$ are the normal and reverse components of normal (vertical) polarization at the focal plane. Similarly, $PS^+(FP)$ and $PS^-(FP)$ are the normal and reverse components of the sideways (horizontal) polarization at the focal plane. The method for determining these focal plane polarizations, $PN^+(FP)$, $PN^-(FP)$, $PS^+(FP)$ and $PS^-(FP)$ is described in sections A.8. and A.12. The measured spin observables take the following form[2-6]:

$$D_{nn} = \{\frac{[PN(FP)+P_nA_y\langle\cos\phi\rangle[A_y\langle\cos\phi\rangle(\cos\chi-P_nPN(FP))]}{\langle\cos^2\phi\rangle}$$

$$-(P_\ell D_{\ell\ell}+P_s D_{s\ell})\sin\chi\}/(P_n\cos\chi)-\frac{D_{ss}\langle\sin^2\phi\rangle}{\langle\cos^2\phi\rangle}-\frac{D_{s\ell}\langle\sin\phi\rangle\tan\chi}{\langle\cos^2\phi\rangle} \quad (3\text{-}2)$$

$$D_{ss} = R_o(1-P_sA_y\langle\sin\phi\rangle)-\frac{D_{nn}\langle\sin^2\phi\rangle}{\langle\cos^2\phi\rangle}+\frac{P(\theta)\langle\sin\phi\rangle}{(P_s\langle\cos^2\phi\rangle)} \quad (3\text{-}3)$$

where $R_o = PS(FP)/(P_s\langle\cos^2\phi\rangle)$

$$D_{s\ell} = R_o'[1 - P_sA_y\langle\sin\phi\rangle] \quad (3\text{-}4)$$

where $R_o' = PN(FP)/2P_s\langle\cos\phi\rangle\langle\sin\chi\rangle$

$$D_{\ell s} = PS(FP)/(2P_\ell\langle\cos\phi\rangle) \quad (3\text{-}5)$$

$$D_{\ell\ell} = A_o' - D_{\ell s}\langle\sin\phi\rangle\langle\cot\chi\rangle \quad (3\text{-}6)$$

where

$A_o' = PN(FP)/(2P_\ell\langle\sin\chi\rangle)$

$$P = \{[P_n^+(FP) + P_n^-(FP)]/2 + P_nA_y\langle\cos\phi\rangle[P_n^+(FP) - P_n^-(FP)]/2\} \quad (3\text{-}7)$$

where by definition:

$$PN(FP) = [PN^{+}(FP) - PN^{-}(FP)]/2$$

$$PS(FP) = [PS^{+}(FP) - PS^{-}(FP)]/2 \qquad (3\text{-}8)$$

ϕ is the azimuthal scattering angle at the target, where $\phi = 0$ corrresponds to scattering horizontally to the left and ϕ is positive in a clockwise direction. $\langle\cos\phi\rangle$ represents the mean of the outgoing proton $\cos\phi$ distribution averaged over all good pd elastic scattering events. χ is the proton precession angle given in eqn (3-1). P_n, P_s, and P_ℓ are the $\hat{n}$-, $\hat{s}$- and $\hat{\ell}$-type beam polarizations. For the derivations of formulas 3-2 through 3-7, see section A.12. The parameters D_{nn}, D_{ss}, $D_{\ell s}$, $D_{\ell\ell}$ and $D_{s\ell}$ basically repesent the probability of the proton to change its spin direction (from the direction of the first subscript to the direction of the second subscript). These observables are measured in the particle helicity laboratory system (see section 1.E.). Note that the expression for D_{nn} given in eqn 3-2 assumes $P = A_y$ (time reversal invariance-see sections 3.K.1. and A.10.) and only depends on the difference in focal plane polarizations, PN(FP) given in eqn 3-8. Because it only depends on PN(FP), the false asymmetries , originating from non-uniform efficiencies and misalignments in the rear wire chambers, tend to cancel. The alternative method for calculating D_{nn} depends on both the difference and the sum of focal plane polarizations, as the induced polarization (P), and is therefore prone to instrumental asymmetries (see section A.12. for the derivation of D_{nn} using this

technique). For a brief description of these instrumental effects see section 3.I. The analyzing power, A_y, is given by:

$$A_y = \{[L-R]/[L+R]\}/P_{beam} \qquad (3\text{-}9)$$

where L and R are the normalized yields for normal and reverse beam polarizations respectively. This is equivalent to measuring the left/right ($\pm\theta$) yields with normal (spin up) beam polarization. But in this experiment, the yields measured, L and R, were made at a lab angle ($+\theta$) using normal and reverse beam polarization. The expressions for the statistical errors in these parameters are given in eqns 3-24 through 3-29.

3.B. Beam Polarization

The polarization, P_{beam}, of a beam of nucleons (polarized in the vertical direction) is given by:

$$P_{beam} = \langle \hat{\sigma}_y \rangle = (\uparrow - \downarrow)/(\uparrow + \downarrow) \tag{3-10}$$

where $\uparrow$, $\downarrow$ denote the number of nucleons with spin up and down respectively and $\hat{\sigma}_y$ is a Pauli spin operator. Empirically, if a polarized beam of nucleons ($P_{beam} > 0$) scatters from a nucleus, a different number of nucleons scatter left (L) than right (R), giving a scattering asymmetry, e, defined by

$$e = (L - R)/(L + R) \tag{3-11}$$

where L, R denote the left and right yields. The analyzing power, A, is defined by

$$e = A \cdot P_{beam} \tag{3-12}$$

Therefore, the maximum asymmetry possible equals A, ,for a 100% polarized beam ($P_{beam} = 1$), and depends on the particular reaction ($A < 1$). The beam polarization, P_{beam}, was typically > 0.8 and varied at most a few percent during the week of beam time.

The Line C beam line polarimeter[3-1], used to measure the beam polarization, employs one of a set of CH_2 target foils whose thicknesses vary between 10 and 32 mils. The polarimeter detector system consists of 8 scintillators, 2 in each arm up, down, left and right. Only the up/down arms are shown in figure 3-1. The polarimeter detects proton-proton (pp) elastic scattering events and $^{12}C(p,2p)^{11}B$ quasifree scattering events. As shown in figure 3-1, the pp events are detected at $\theta_{lab} = 17^{o}$ (conjugate angle is $\theta_{lab} = 66^{o}$, where the analyzing power for pp elastic scattering at 800 MeV is a maximum[3-2] and equals 0.504. The two protons are detected in coincidence, therefore eight scintillators are required to construct the four - left, right, up, down yields. Because the carbon in the CH_2 target contributes to the pp elastic scattering yield, the inclusive analyzing power[3-3,4] is less (0.475 at 800 MeV).

The left/right and up/down asymmetries are used to measure the normal and sideways components of beam polarization respectively. From parity conservation, the longitudinal component produces no scattering asymmetry and therefore cannot be measured by a polarimeter.

A technique which eliminates instrumental asymmetries to a high order uses the fact, from rotational symmetry (180^{0} about the beam direction), that the left yield for normal beam is equal to the right yield for reverse beam and vice versa. The left and right yields in eqn (3-11) are defined as:

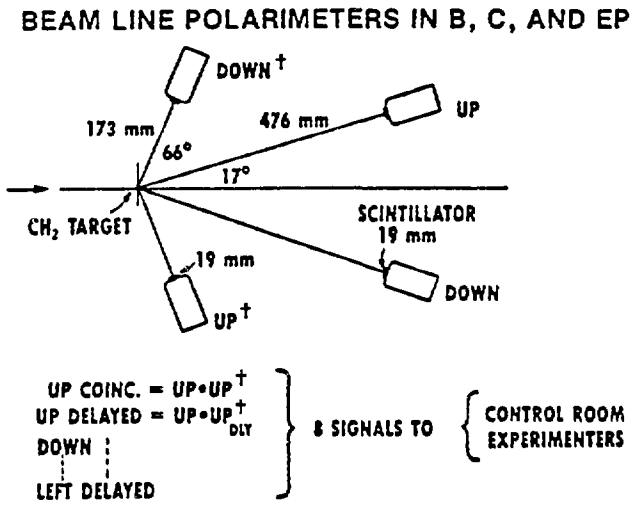

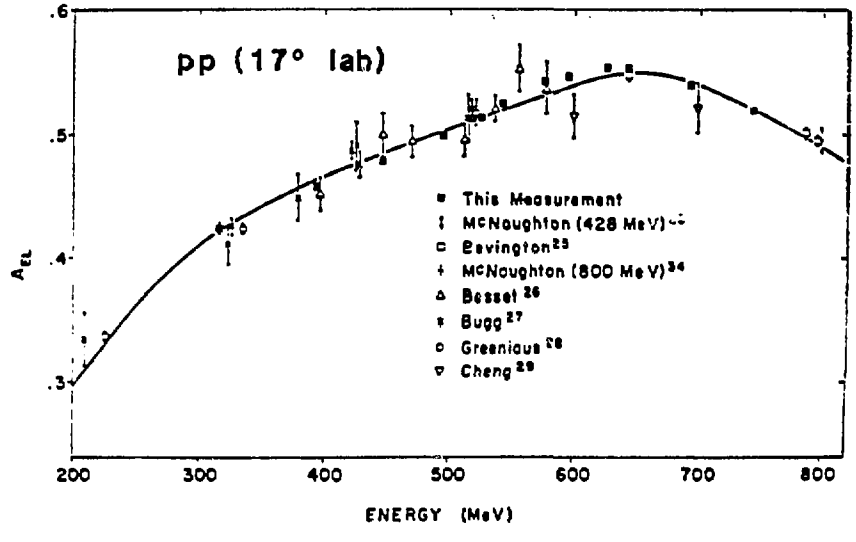

FIGURE 3-1

Beam-line Polarimeter EPB, BR, LC areas

$$L = \sqrt{(L\uparrow)(R\downarrow)} \tag{3-13}$$

$$R = \sqrt{(R\uparrow)(L\downarrow)}$$

Here $\uparrow$, $\downarrow$ denote normal and reverse (up and down) beam polarizations. In order to minimize effects due to beam fluctuations, the beam polarization was flipped every minute. The beam was polarized in the normal direction 55 seconds, then for 5 seconds it was quenched, then polarized in the reverse direction. During the quenched period only the unpolarized background in the beam remains (the unpolarized component of the "polarized" beam). Using this method for determining the beam polarization assumes that the polarization is the same for normal and reverse beam.

In addition, it was possible to obtain the magnitude of the beam polarization using the "quench ratio". The magnitude of the beam polarization is[3-5]

$$P'_{beam} \simeq 1 - I_q/I_p \tag{3-14}$$

where

P'_{beam} = magnitude of the beam polarization

I_q = Intensity of the unpolarized background of the beam

I_p = Intensity of the beam during the polarized cycle

The beam intensities, I_q and I_p, were measured using ion chambers. The beam polarization given here, P'_{beam}, is the magnitude of the polarization vector which can be in a direction slightly off from the one of the three orthogonal directions desired. Therefore, $P'_{beam} > P_{beam}$.

Unfortunately because of the "beam spray" at the Line - C polarimeter (LCPO) the random coincidence rate at the LCPO could be extremely high (> 20% sometimes). In addition, there is probably a substantial amount of pp quasifree scattering from the polarimeter target frame. These effects make the LCPO asymmetry and value of polarization too low in most cases (all of the yields increase, diluting the asymmetry, e, given in eqn (3-11)). The accuracy in making corrections for the random coincidences was at the few percent level. Even with these corrections, the LCPO value of polarization was still too low. In addition, the disagreement between the LCPO and quench values of beam polarization were not beam intensity dependent implying that the problem with the LCPO arises from scattering from the frame. As a result, in this experiment, the quench ratio was used to determine the beam polarization, except for a few instances when the statistics on the quench ratio were very poor. At forward angles, where the pd unpolarized differential cross section is large, the computer limits how fast data can be taken, allowing for only a small beam intensity with a finite thickness CH_2 polarimeter target. Therefore, the quench ratio had poor statistics

at small scattering angles. In most cases[3-6], the quench value of beam polarization is accurate to ~1%.

But the LCPO was useful in determining the spurious beam polarization components due to small (<5 degrees) misalignments of the beam spin direction. These corrections were made to the data, see section 3-C. The data from the External Proton Beam (EPB) polarimeter was also used for these corrections. Fortuitously, during most of the experiment, EPB had their bending magnets set so that the EPB polarimeter (EPPO) $\hat{s}$-type spin component approximately measured the HRS $\hat{\ell}$-component of spin, which is not measured by the LCPO. It turns out that during part of this experiment the beam polarization was ~5° off and rather large (~8%) spurious $\hat{\ell}$-components of beam polarization existed. The corrections to the observables measured are described in section 3.C. Even though the absolute magnitude of beam polarization could not be extracted accurately from the LCPO in most cases, it was useful in tracking the fluctuations.

3.C. Spurious Beam Polarization Corrections

The incident proton beam was polarized in one of three independent directions. The three orthogonal directions are defined in the laboratory system to be $\hat{\ell}$, $\hat{n}$ and $\hat{s}$ which represent the longitudinal ($\parallel$ to the incident proton momentum), normal ($\perp$ to the scattering plane) and sideways ($\hat{n} \times \hat{\ell}$, in the scattering plane) components respectively, see eqn (1-24). When the beam was polarized in any one of these three directions, it was within 5^0 of that direction. In some cases, when the beam spin direction was off by up to 4.6^0, the other components of the incident beam polarization were up to 8% (i,e. $\tan\theta = P_\ell/P_n$). In calculating the proton spin transfer observables, large corrections (<17%) were necessary. The worst case in this experiment is the $\hat{n}$-type beam polarization portion of data. Corrections of 10-17% were made in the calculation of D_{nn}.

These spurious (unwanted) beam polarization corrections were made using the Line C polarimeter (LCPO), located 10 meters upstream of the target and the EPB polarimeter (EPPO), which is in the EPB area. As described in section 3.B., one of the most useful functions of the LCPO in this experiment was to determine the spurious $\hat{n}$- and $\hat{s}$-type polarization components. Fortuitously during the HRS $\hat{n}$-type beam measurements of this experiment, the bending magnets in the EPB area were such that the EPB $\hat{s}$-component of spin was basically the HRS $\hat{\ell}$-component, aside from small differences in the phase space of the beam between the two areas. Therefore the EPPO was used to determine the HRS $\hat{\ell}$-component of spin. The proton spin observable expressions

(eqns 3-2 to 3-7) given in section 3.A. include terms which correct for these spurious components using the first order measured observables (without the spurious beam polarization corrections included). No information on the HRS $\hat{\ell}$-component of polarization was available for the $\hat{s}$-type beam data, so the $\hat{\ell}$-component of beam polarization was neglected in this case.

Table 2 gives the $\hat{\ell}$-component beam polarization corrections to the HRS $\hat{n}$-type beam data. These corrections were obtained from the EPPO data discussed above. As seen in the table, the $P_{\ell}D_{\ell\ell}\sin\chi/P_n\cos\chi$ correction to D_{nn} in eqn 3-2 was 10-17%. These correction make D_{nn} smaller and happened to be largest at the largest scattering angles, see discussion on the data in section 4.B.

Table 2 - Longitudinal Beam Polarization Corrections to $\hat{n}$-Beam Data

Angle(deg)	$P_\ell D_{\ell\ell} \sin\chi / P_n \cos\chi$
3	.097
6	.109
9	.119
12	.124
15	.133
18	.155
20	.161
22	.173

3.D. Energy Resolution

For p-d elastic scattering at the HRS, energy resolution is not very important since deuterium has only one bound state - its ground state (2.2 MeV binding energy). The first "excited state" of deuterium is 80 KeV unbound and represents a spin-flip transition (spin triplet to spin singlet). Even at the smallest momentum transfer measured ($-t = .005$ $(GeV/c)^2$ - 3^o lab), the d(p,p) peak was well separated from the $^{12}C(p,p)$ elastic peak, which came from the mylar target window and jacket (see the spectra of fig. 3-2). The yield from deuteron break-up spans from ~ 2.2 MeV out to ~10 MeV, the HRS acceptance produces a cutoff. The break-up was largest (relative to the elastic peak) at the largest scattering angles (see figure 3-3). But it is also well separated from the d(p,p) elastic peak. As seen in fig. 3-3, the break-up is to the right of the pd elastic peak (larger missing mass). The carbon scattering high excitation region produces background to the left of the pd elastic peak. The FWHM of the pd elastic peak was typically ~ 500 KeV at 3^o and ~ 2 MeV at the largest scattering angles (out to 28^o). The energy resolution has three contributions. These different effects are summed in quadrature in obtaining the width of the elastic peak. The total width of the spectrum is given by

$$\Gamma = \sqrt{K^2 + S^2 + I^2} \quad \text{(MeV)} \qquad (3\text{-}15)$$

where K, S and I are defined below.

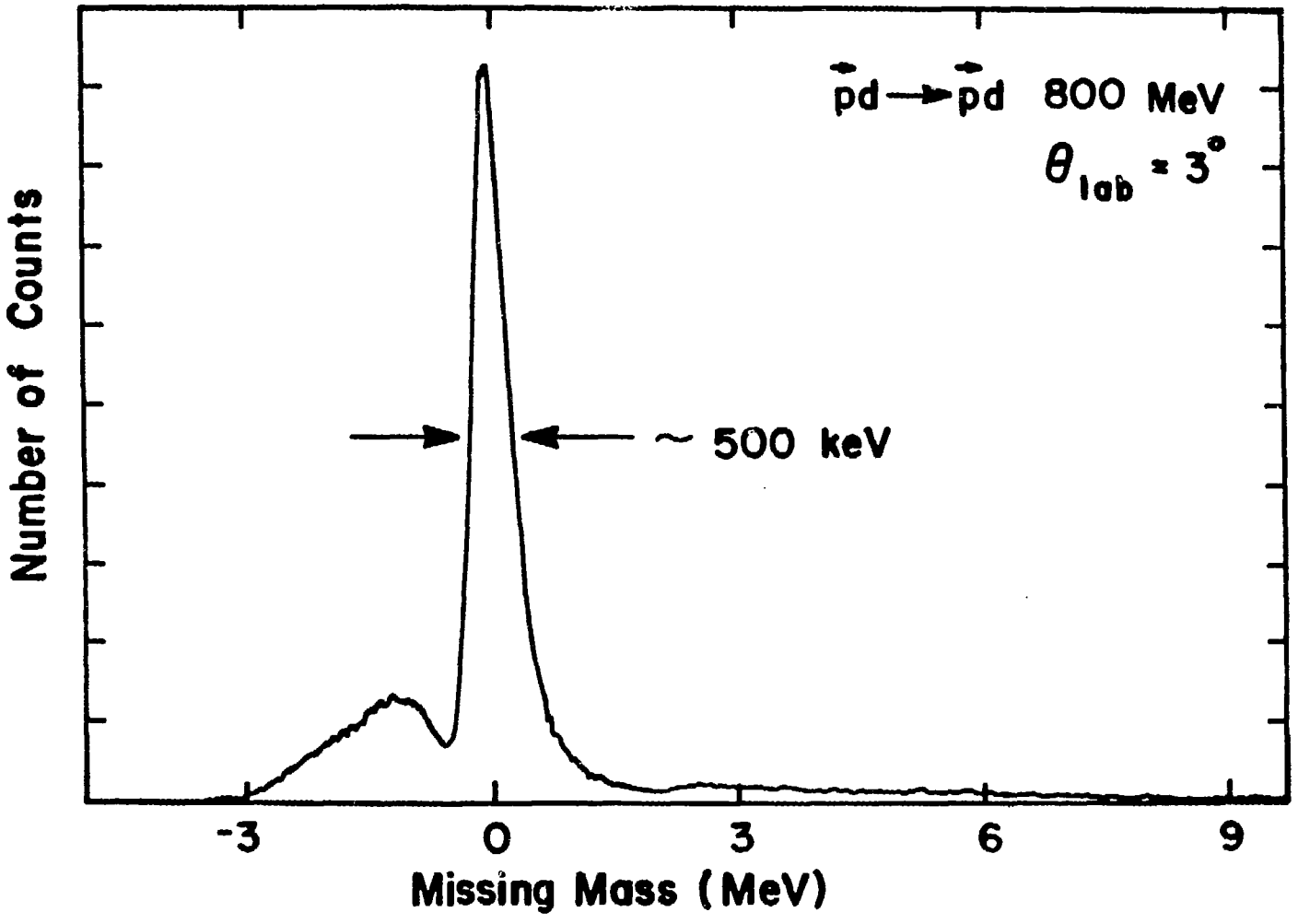

FIGURE 3-2 Missing mass spectrum $\theta_{lab} = 3^{\circ}$ for $\vec{p}d \rightarrow \vec{p}d$ at 800 MeV

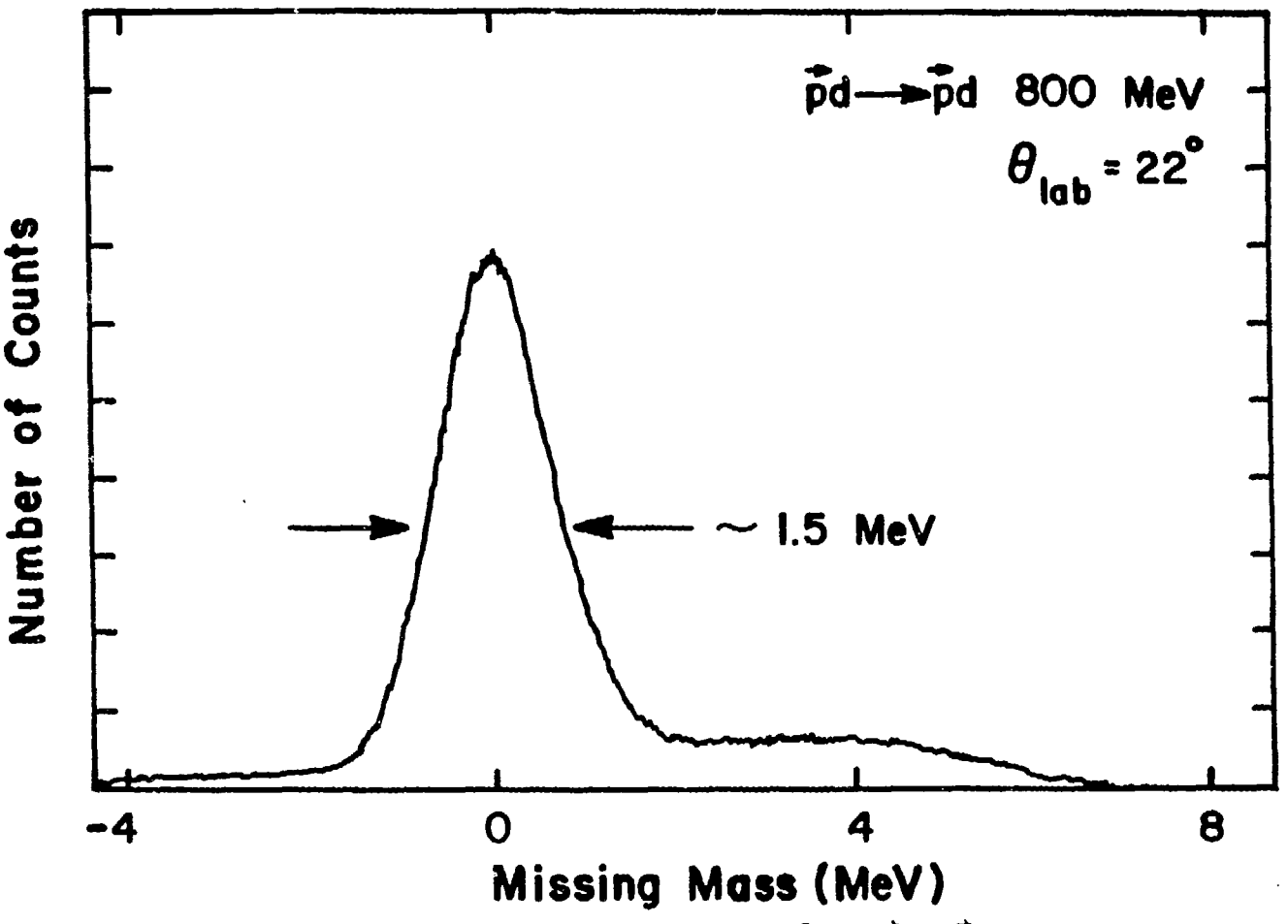

FIGURE 3-3 Missing mass spectrum $\theta_{lab} = 20^{\circ}$ for $\vec{p}d \rightarrow \vec{p}d$ at 800 MeV

A) Multiple Coulomb Scattering - Kinematic Shift (K)

Because elastically scattered protons of different scattering angles have different outgoing energies and the HRS has ~2° horizontal acceptance, the d(p,p′) peak is broadened because of angular resolution. In addition to the finite angular resolution of the HRS, multiple Coulomb scattering broadens the scattering angle distribution. The energy of the outgoing protons is calculated from its scattering angle using the kinematics for a single nuclear d(p,p) elastic scattering. But the elastically scattered outgoing protons also undergo many small angle Coulomb deflections (in the deuterium and the carbon of the target jacket) which produce a scattering angle cone. The software cannot correct for the angular broadening and as a result this degrades the energy resolution. The rms multiple coulomb scattering angle decreases with increasing proton energy in this energy regime. The rms multiple coulomb scattering angle, θ_o, is given by[3-7]

$$\theta_o = (14.1 \text{ MeV/c}) Z_{inc} \sqrt{L/L_R} \cdot [1+1/9 \cdot \log_{10}(L/L_R)]/p \cdot \beta \text{ (radians)} \quad (3\text{-}16)$$

where p,β and Z_{inc} are the momentum (in MeV/c), velocity and charge number of the incident particle, and L/L_R is the thickness, in radiation lengths, of the scattering medium. θ_o for d(p,p)at 800 MeV, including the mylar target jacket and window, is 0.030° at 3° lab and 0.033^0 at 28° lab. The FWHM of the multiple coulomb scattering (assuming a gaussian distribution) is $2.354\ \theta_o$.

The change in the outgoing proton energy per change in the outgoing proton scattering angle (kinematic shift) is defined as, $dT/d\theta$, given in MeV/deg. At a lab angle of 3° $dT/d\theta$ is -1.04 MeV/deg and at 28° it is -7.78 MeV/deg. Note kinematically that as the scattering angle increases the magnitude of $dT/d\theta$ increases strongly.

The multiple Coulomb-kinematic shift effect results in a FWHM broadening of 0.08 MeV at 3° and 0.61 MeV at 28° and dominates the energy broadening at large momentum transfers. The inherent angular resolution (without multiple Coulomb scattering) of the HRS is $\sim 0.06^{0}$ which is roughly the same as the multiple Coulomb scattering contribution. Since these angular effects are added in quadrature, the FWHM energy spectra are broadened by a factor of $\sim\sqrt{2}$.

B) Energy Straggling

As a result of the elastically scattered protons losing different amounts of energy in the target, the energy resolution also degrades. The Landau straggling contribution (FWHM of energy loss distribution) is of the order:

$$\Delta \approx 1/3(\text{Energy loss in the target}) \qquad (3\text{-}17)$$

The energy loss in the target and jacket together is ~1.5 MeV, so $\Delta \approx$ 0.5 MeV.

This straggling contribution stays roughly constant throughout the momentum transfer range of this experiment, but is most important at the small scattering angles where the multiple coulomb scattering/kinematic shift contribution to energy resolution is not as important.

C) Intrinsic Spectrometer-Beam Resolution

The d(p,p) peak is also broadened in energy because the incoming beam protons have an equivalent energy bite ~80 KeV. The accelerator provides roughly a 2 MeV FWHM energy bite. The vertical direction at the HRS target is the dispersion direction. Even though the FWHM energy bite on target is ~1.5 MeV, the spectrometer together with the Line-C dispersion matched optics provides a ~80 KeV FWHM energy distribution at a given vertical position at the target. This was not extremely important since its contribution to the total energy resolution is negligible in this experiment, especially at the large momentum transfers. This energy bite is determined by the spectrometer calibrations together with the Line C beam tune.

3.E. Out of Plane Scattering Corrections

Corrections to the polarization data are necessary because of the finite vertical acceptance of the HRS. The vertical acceptance of the HRS is $\sim\pm1^0$ and allows outgoing particles to scatter such that the scattering plane, which is defined by the incident and outgoing proton momenta, make an angle with the floor. As a result, the $\hat{n}$ and $\hat{s}$ components of the outgoing proton polarization are mixed in the HRS coordinate system (defined by the floor). These corrections can be shown to be of the form[2-6]:

$$1/\langle\cos\phi\rangle \text{ or } 1/\langle\cos^2\phi\rangle \tag{3-18}$$

and are included in the expressions for the spin rotation parameters in section 3.A. For the derivation of these corrections, see section A.12. Note that $\langle\cos\phi\rangle$ is the mean of the $\cos\phi$ distribution, where ϕ is the azimuthal scattering angle of the proton at the target (see section 3.A.). As seen in the expressions for the spin-transfer observables given in section 3.A., these corrections increase the values of the parameters. This is because the measured polarizations are only projections onto the HRS coordinate system (see section 1.E.).

These corrections are largest at forward angles, where the azimuthal acceptance of the HRS is largest. For example, at a laboratory scattering angle of 3^0 the azimuthal acceptance of the spectrometer, ϕ_{max}, is $\sim15^0$. The corrections to the spin rotation

parameters were up to 14% at a lab angle of 3^0. The magnitudes of these out of plane corrections to the measured observables is given in Tables 3A and 3B.. The validity of these corrections were checked and the method is described in section 3.K.3.

Table 3A - Out of Plane Scattering Corrections

Parameter affected	D_{nn}	D_{nn}	D_{ss}
Angle	$D_{ss}\langle\sin^2\phi\rangle/\langle\cos^2\phi\rangle$	$D_{s\ell}\langle\sin\phi\rangle\tan\chi/\langle\cos^2\phi\rangle$	$D_{nn}\langle\sin^2\phi\rangle/\langle\cos^2\phi\rangle$
2.5	.1297	-.0007	
3.0	.1151	-.0005	.1226
3.5	.1039	-.0004	
6.0	.0444	.0054	.0355
9.0	.0178	.0040	.0189
12.0	.0091	.0035	.0106
15.0	.0060	.0033	.0061
18.0	.0040	.0033	.0036
20.0	.0032	.0033	.0032
22.0	.0028	.0021	

Table 3B - Out of Plane Scattering Corrections Continued

Parameter affected	D_{ss}	D_{ss}	$D_{\ell\ell}$	D_{nn}
Angle	$P\langle\sin\phi\rangle/P_s\langle\cos^2\phi\rangle$	$P\langle\sin\phi\rangle/P_s\langle\cos^2\phi\rangle$	$D_{\ell s}\langle\sin\phi\rangle/\tan\chi$	$1/\langle\cos\phi\rangle$
3.0	-.0002	-.0378	.0022	.9383
6.0	.0016	-.0454	-.0005	.9805
9.0	-.0009	-.0331	-.0005	.9914
12.0	-.0021	-.0286	-.0008	.9952
15.0	.0013	-.0380	.0001	.9963
18.0	.0002	-.0337	-.0002	.9976
20.0	.0006	-.0282	-.0004	.9983
22.0	-.0230	-.0001		.9984
24.0	-.0200	-.0001		.9987
26.0	-.0151	-.0003		.9990
28.0	-.0116	-.0001		.9991

3.F. Analyzing Power in Carbon

Given the scattering distribution of protons in the carbon, the carbon analyzing power, A_c, is required to extract the proton polarizations. The values of the analyzing power in carbon used in the analysis were obtained using the global fit from 400-800 MeV of Ransome et. al[3-3]. As shown in table 4, A_c ranges from 0.2-0.3 in the angular region of interest at energies near 800 MeV. This makes the maximum scattering asymmetry in the carbon ~0.2-0.3, even with a 100% polarized proton beam and an unprecessed component of spin with a Wolfenstein parameter of unity (see section 3.A.).

In table 4, A_c is given for various energies in MeV as a function of carbon polar scattering angle. For $\vec{p}d \rightarrow \vec{p}d$ elastic scattering the outgoing proton energy decreases fairly rapidly as the proton scattering angle increases. The values of A_c are given for $1\text{-}20^0$ polar scattering angle in the carbon at the energies corresponding to the scattering angles measured in this experiment. See table 6 for the proton scattering angles that these energies correspond to.

Actually the energies of the carbon analyzing powers used in the analysis and listed in table 4 are ~41-51 MeV lower than the scattered proton energies listed in table 6 because of the proton energy loss in the carbon.

An estimate for the uncertainty in A_c can be taken from the difference in the 800 MeV measurement by Bartlett et. al.[3-11] and

the global fit (as a function of momentum) of ref 3-3, used in this analysis. The relative difference in A_c is ~4%.

Table 4 - Carbon Analyzing Power at Various Energies (MeV) vs θ

θ (deg)	748	744	735	724	716	700	688	675	661	651	636
1	.041	.042	.043	.044	.045	.046	.047	.047	.048	.048	.048
2	.083	.084	.087	.089	.091	.093	.094	.096	.096	.097	.097
3	.125	.127	.131	.134	.137	.140	.143	.144	.145	.147	.148
4	.166	.169	.173	.178	.181	.186	.189	.192	.194	.196	.198
5	.203	.206	.211	.216	.220	.227	.231	.234	.237	.240	.243
6	.229	.233	.238	.244	.248	.256	.260	.265	.268	.272	.277
7	.244	.247	.252	.258	.262	.270	.275	.280	.283	.288	.293
8	.248	.251	.255	.260	.264	.271	.275	.280	.283	.287	.293
9	.246	.248	.251	.255	.258	.263	.267	.270	.273	.277	.281
10	.242	.243	.245	.247	.249	.252	.255	.258	.259	.262	.266
11	.239	.239	.240	.240	.241	.242	.244	.245	.246	.248	.251
12	.238	.237	.236	.235	.234	.234	.235	.235	.236	.237	.239
13	.237	.235	.233	.231	.230	.228	.227	.227	.227	.228	.229
14	.237	.234	.231	.228	.226	.223	.222	.221	.221	.221	.222
15	.236	.234	.230	.226	.223	.219	.218	.216	.216	.216	.216
16	.236	.233	.228	.223	.220	.216	.214	.212	.212	.211	.211
17	.235	.231	.226	.221	.218	.213	.210	.208	.207	.207	.207
18	.233	.229	.224	.218	.214	.209	.206	.204	.203	.202	.202
19	.229	.226	.220	.214	.210	.205	.202	.199	.199	.198	.197
20	.225	.221	.216	.209	.206	.200	.197	.194	.193	.192	.192

3.G. Multiple Scattering in the Carbon

The outgoing protons in the scattering undergo small angle multiple Coulomb scatterings in the liquid deuterium target, mylar window and flask and the carbon of the carbon analyzer. As discussed in section 3.D., the multiple scattering in the target and its walls degrades the energy resolution. Because the scattering distribution in the carbon analyzer is used to determine the outgoing proton polarization, it is fairly important to fix the multiple Coulomb scattering angle in the carbon. In fact the critical feature is to keep the multiple Coulomb scattering angle smaller than the carbon polar scattering angle software cut (see below). The multiple Coulomb scattering angle goes like:

$$\theta_{ms} \propto \sqrt{L}/p\beta \qquad (3\text{-}19)$$

where L = carbon thickness and p = outgoing proton momentum. The exact expression is given in eqn (3-16). The carbon thickness was decreased (see section 2.B.1.) at the larger momentum transfers as a result of the kinematic shift in order to keep θ_{ms} roughly constant as a function of momentum transfer.

At small scattering angles in the carbon, multiple Coulomb scattering dominates. Since the nuclear scatterings in the carbon are used to determine the proton polarization and the multiple Coulomb scatterings carry no information on the proton polarization (Coulomb force has no spin dependence) software cuts are imposed on

the polar scattering angle in the carbon. In addition to the software cuts, $3.5^0 < \theta_c < 20.5^0$, the MBD puts hardware cuts on the polar scattering angle during data acquisition. As described in section 2.C., the MBD does crude calculations on the data in order to maximize the fraction of good data written to tape. The crude MBD cuts in the carbon polar scattering angle data are restricted to polar scattering angles less than 2.5^0 in the carbon so that no instrumental asymmetries are introduced by the MBD. Note that the MBD cut in polar scattering angle is not sharp because it is a fast-rough calculation. The Coulomb multiple scattering extends out to 2.5^0, but drops off rapidly as the polar scattering angle increases.

3.H. Calculating the Analyzing Power for pd Elastic Scattering

The analyzing power, A_y, is the left/right scattering asymmetry produced using a 100% polarized beam (polarized ⊥ to the scattering plane). The analyzing power has the form:

$$A_y = \{[YN^* - YR^*]/[YN^* + YR^*]\}/P_{beam} \qquad (3\text{-}20)$$

where YN^* and YR^* are the normalized yields for normal (spin up) and reverse (spin down) beam polarizations. They have the form:

$$YN^* = CF^N * YN/ERO4^N \qquad (3\text{-}21)$$

$$YR^* = CF^R * YR/ERO4^R$$

where

$$CF^N = [CLT^N \cdot CE^N \cdot MBD^N]^{-1} \qquad (3\text{-}22)$$

$$CF^R = [CLT^R \cdot CE^R \cdot MBD^R]^{-1}$$

$ERO4^N$ and $ERO4^R$ répresent the ion chamber counts for normal and reverse beam. Two ion chambers are located roughly 50 cm downstream of the target and measure the integrated beam intensity. CLT^N and CLT^R are the computer livetimes for normal and reverse beam polarizations, they typically were 0.90. CE^N and CE^R stand for the overall chamber efficiencies for normal and reverse beam. They were 0.8 during most of the expetriment, but varied by as much as 0.2.

The chambers are much more efficient at forward angles, when the beam intensity used is much lower due to the larger cross section. Therefore fewer background particles/second are going through the wire chambers. Because the microprogrammable branch driver microprocessor (MBD) was used during data aquisition, and its efficiency was different for normal and reverse beams, (because there were different event rates into the MBD for normal and reverse beam and the MBD efficiency is event rate dependent) corrections were necessary in calculating A_y. MBD^N and MBD^R are these correction for normal and reverse beam polarizations.

3.I. Problems in Calculating the Induced Polarization

The induced polarization, P, is the outgoing polarization obtained using an unpolarized beam and target. As shown in eqn 3-3, P depends on the sum of the normal and reverse beam components of polarization in the vertical direction at the focal plane polarimeter. This is the only spin observable which depends on the sum of focal plane polarizations. As a result, instumental asymmetries due to poor chamber calibrations do not cancel as they do in the other parameters which depend only on differences in measured focal plane polarizations. Chamber calibration refers to the whole procedure of calculating particle positions, which are used to calculate almost all quantities of interest. Even a poor chamber calibration (calculation of wire position or drift time-see section 3.A.) is not extremely important except in the case of P.

The instrumental asymmetries (false asymmetries due to the hardware or the analysis techniques) are large at 800 MeV. The errors are of the following form:

$$\Delta P \propto \Delta\varepsilon / A_c \cos\chi \qquad (3\text{-}23)$$

where $\Delta\varepsilon$ is the instrumental asymmetry, A_c is the carbon analyzing power and $\cos\chi$ is the correction due to the precession of the normal component of spin through an angle χ. At 800 MeV, as given in table 3, $0.2 < A_c < 0.3$. The values of $\cos\chi$ range from 0.5 to 0.8.

Therefore in the calculation of P, the instrumental asymmetries are magnified by a factor of 6. So a false asymmetry, $\Delta\varepsilon$, if not corrected for, of 0.01 gives an error in P, ΔP, of 0.06. The values of P obtained in the analysis were very inconsistent and were not used. This was not too serious since A_y was measured independently and $P = A_y$ from time reversal invariance (see section 3.K.1 and figure 4-1b).

3.J. Sources of Errors in the Data

In addition to the standard errors in the data due to counting statistics, there were several other sources of statistical and systematic errors. The errors quoted in tables 8-13 and figures 4-2,13 only include counting statistics except for a few data points, where fairly large beam polarization uncertainties exist.

Uncertainty in the beam polarization inherently produces errors in the measured observables. It is unclear whether these errors are statistical or systematic in nature. The quench value of beam polarization *(see section 3.B) is normally known to ~1-2%, although* it can be dependent on the properties of the ion source[3-5].

Uncertainties in the carbon analyzing power, A_c, as a function of polar scattering angle in the carbon creates errors in the outgoing proton polarizations. As discussed in section 3.F., the values of the A_c used in the data analysis were taken from the global fit of Ransome et. al.[3-3]. Some 800 MeV A_c measurements were done by Bartlett et. al. at the HRS[3-11]. The values of A_c obtained from their measurements were ~3.8% higher than the fit of ref. 3-3. Assuming this to be the uncertainty in A_c, this creates a relative (systematic) error in the parameters of up to ~3.8%, depending on the value of a particular parameter.

In general, the chamber calibrations could be an important source of systematic errors. Chamber calibration refers to the whole procedure of calculating particle positions, which are used to calculate all quantities of interest. But most of the measured

spin-rotation parameters are calculated using differences in the polarizations measured at the focal plane. As a result, the "instrumental asymmetries" errors due to a poor chamber alignment, tend to cancel to first order. But the measurement of the induced polarization, P, involves the sum of focal plane polarizations. Because of this it is extremely difficult to measure, especially at 800 MeV. As discussed in section 3.I., the errors in P, due to instrumental asymmetries, were so large that P was not calculated in this experiment. This is not too serious since $P = A_y$ from time reversal, and A_y was measured, but it would have been "nice" to have for an additional systematic check.

As discussed in section 3.H., the calculation of A_y was complicated because all of the data was taken using a fast microprocessor (microprogrammable branch driver, MBD) in addition to the main computer. The A_y data had to be corrected because of the MBD and has a statistical error associated with this correction. This statistical error has been included in the errors of table 13 and figure 4-6.

The corrections to the spin observables due to unwanted or spurious beam polarization components were known to ~1%. These corrections were made using the LCPO and EPPO as described in section 3.C.

An error in the spin precession angle due to the uncertainty in bend angle of the protons in the HRS dipoles produces errors which are virtually negligible compared to the other errors discussed

above. Also an uncertainty in the incoming proton beam energy creates a negligible error in the observables. The proton beam energy was known absolutely to within a few MeV, but the proton spin observables are insensitive to differences in beam energy this small. The expressions for the statistical errors in the Wolfenstein parameters and the analyzing power are given below. They result from counting statistics only and are derived using first order gaussian error propagation.

$$\delta D_{nn} = \frac{\{[P_b A_y \langle\cos\phi\rangle+1]^2[\delta P_N^+(FP)]^2+[1-P_b A_y \langle\cos\phi\rangle]^2[\delta P_N^-(FP)]^2\}^{1/2}}{2\cos\chi\langle\cos\phi\rangle} \quad (3\text{-}24)$$

$$\delta D_{ss} = \delta PS(FP)/P_s\langle\cos\phi\rangle \quad (3\text{-}25)$$

$$\delta D_{s\ell} = \delta PN(FP)/P_s\langle\cos\phi\rangle\sin\chi \quad (3\text{-}26)$$

$$\delta D_{\ell s} = \delta PS(FP)/P_\ell\langle\cos\phi\rangle \quad (3\text{-}27)$$

$$\delta D_{\ell\ell} = \delta PN(FP)/P_\ell\sin\chi \quad (3\text{-}28)$$

$$\delta A_y^2 = |dA_y/dYN^*|^2\delta YN^{*2} + |dA_y/dYR^*|^2\delta YR^{*2} \quad (3\text{-}29)$$

where YN^* and YR^* are the normalized yields for normal and reverse beam polarizations.

3.K. Systematic Checks

Several systematic checks on the data were possible. In section 3.K.1., time reversal invariance requires that $D_{s\ell}$ equal $-D_{\ell s}$ data in the center of mass frame. Parity conservation (see section A.10.) restricts the depolarization observable, D_{nn}, for a spin 1/2 x 0 reaction, such as proton-carbon elastic scattering. This is presented in section 3.K.2. As described in section 3.E., large out of plane scattering corrections to the data were required at forward angles. The checks on these corrections are discussed in section 3.K.3. In addition, the data of this experiment are compared with data taken at larger momentum transfers in an independent experiment performed at the EPB area of LAMPF. As seen in figures 4-8 through 4-13, the proton spin transfer observables of this experiment are in agreement with those of the EPB experiment in the region of overlap. The experimental method at EPB[1-30] was rather different than the HRS setup.

3.K.1 Time Reversal Invariance

As a result of time reversal invariance,

$$P = A_y \tag{3-30}$$

The induced polarization, P, which is the outgoing polarization obtained with an unpolarized beam and target is equal to the analyzing power, A_y which is the left/right scattering asymmetry for a 100% polarized beam (polarized $\perp$ to the scattering plane) as defined in eqns (3-11,12). For the proof of eqn 3-30, see section A.10. This result was not checked because of the problems mentioned in section 3.I.

Another result that follows from time reversal invariance is the following relation (see section A.10. for the proof):

$$D_{s\ell} = -D_{\ell s} \text{ (in the center of mass system)} \tag{3-31}$$

The transformation of the proton spin observables from the lab to the center of mass (CM) frames and vice versa are done using the appropriate Wigner rotations, as described in section A.11. The CM observables are just linear combinations of the lab observables. The transformation matrix takes the following form:

$$\begin{bmatrix} D_{xx} \\ D_{zz} \\ D_{zx} \\ D_{xz} \end{bmatrix} = \begin{bmatrix} cc' & ss' & -sc' & -cs' \\ ss' & cc' & cs' & sc' \\ sc' & -cs' & cc' & -ss' \\ cs' & -sc' & -ss' & cc' \end{bmatrix} \begin{bmatrix} D_{ss} \\ D_{\ell\ell} \\ D_{\ell s} \\ D_{s\ell} \end{bmatrix} \qquad (3\text{-}32)$$

Here

$$\begin{aligned} \chi &= \theta_{cm}/2 \\ \chi' &= -\theta_{cm}/2 + \overline{\theta}_{lab} \\ c &= \cos\chi \\ c' &= \cos\chi' \\ s &= \sin\chi \\ s' &= \sin\chi' \end{aligned} \qquad (3\text{-}33)$$

Here D_{xx}, D_{zz}, D_{zx} and D_{xz} are the center of mass observables and D_{ss}, $D_{\ell\ell}$, $D_{\ell s}$ and $D_{s\ell}$ are the corresponding lab observables. For more details on these Wigner rotations see section A.11. Table 5 gives the values of $D_{s\ell}$ and $D_{\ell s}$ in the CM as a function of lab scattering angle. In fig 3-4 $D_{\ell s}$ and $-D_{s\ell}$ in the center of mass system are plotted as a function of q(GeV/c). This provides a nice consistency check on the data.

Table 5 - $D_{\ell s}$ and $D_{s\ell}$ in the CM System

Angle	$D_{\ell s}$(CM)	$D_{s\ell}$ (CM)
3	-.447±.022	.485±.024
5	-.369±.023	.364±.020
9	-.190±.039	.200±.020
12	-.056±.018	.026±.024
15	.089±.018	-.099±.022
18	.201±.017	-.175±.021
20	.257±.019	-.211±.023

FIGURE 3–4

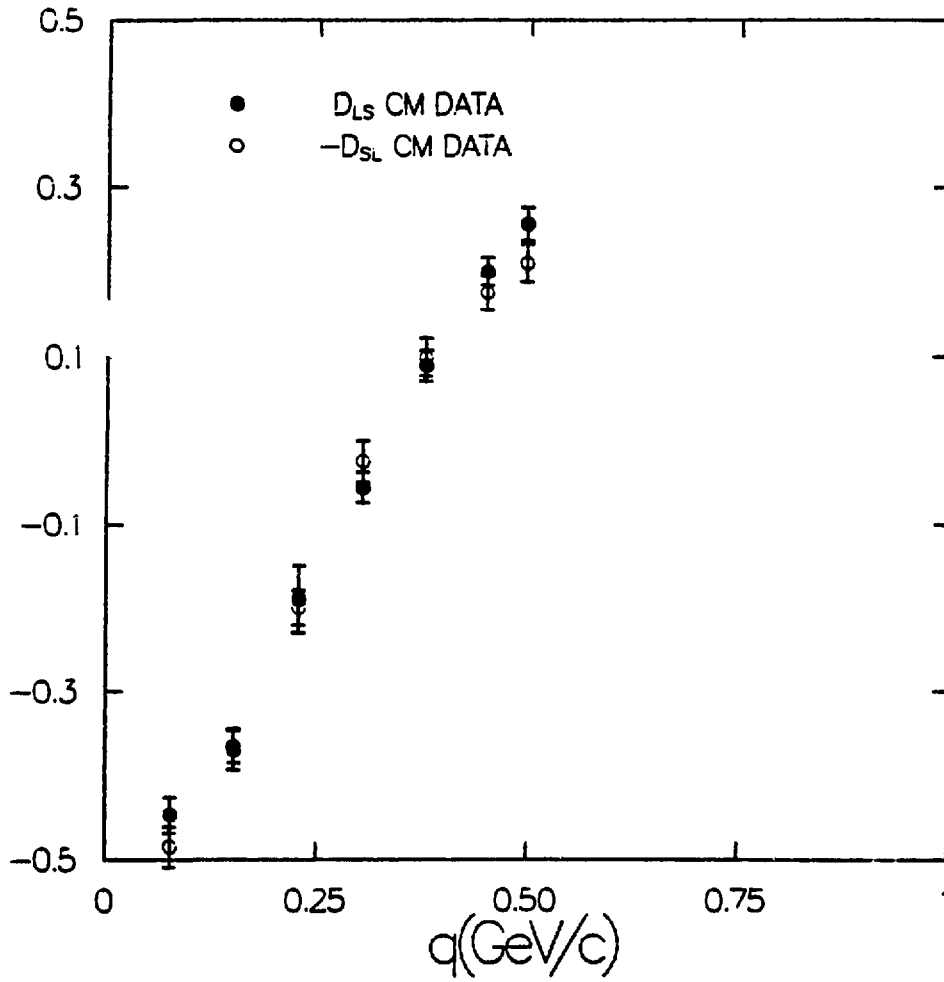

FIGURE 3-4

$D_{\ell s}$ and $-D_{s\ell}$ in CM system

3.K.2. D_{nn} for Carbon

It was possible to separate the proton-deuterium from the proton-carbon elastic scattering, even at forward angles, where the outgoing proton energies from these reactions are relatively close (see the p-d and p-^{12}C kinematics given in table 6. The peaks are separated by ~1.3 MeV at 3^{0} and the p-d peak is ~500 KeV wide, see figure 3-2 and section 3.D. Because $^{12}C(\hat{p},\hat{p})$ is a spin 1/2 x 0 system, it provides the opportunity to verify this spin-transfer technique in a different fashion. For the spin 1/2 x 0 scattering case,

$$D_{nn} = 1 \qquad (3\text{-}34)$$

from parity (proved in section A.10). This means that no spin-flip is possible on a spin 0 nucleus. This result has been verified in other experiments done at the HRS. In this p-d experiment, it was only possible to detect the proton scattering from carbon at 3^{0} because of the limited momentum acceptance allowed by the scintillator S_x (see section 2.B.1). At 3^{0}, $D_{nn} = 0.94 \pm 0.07$ for 12C(p,p'), so $D_{nn} = 1$ within error bars.

Table 6 - $\vec{p}d \rightarrow \vec{p}d$ Kinematics

Lab Angle	CM Angle	$-t$(GeV/c)	T^D(MeV)	T^{12C}(MeV)	$dT^D/d\theta$(MeV/^{0})
2.5	4.4	0.0041	798.9	799.8	-0.9
3.0	5.3	0.0059	798.4	799.7	-1.0
3.5	6.2	0.0080	797.9	799.6	-1.2
6.0	10.6	0.0234	793.8	799.0	-2.1
9.0	15.8	0.0522	786.1	797.6	-3.1
12.0	21.0	0.0920	775.5	795.8	-4.0
15.0	26.2	0.1420	762.1	793.5	-4.9
18.0	31.4	0.2016	746.2	790.7	-5.7
20.0	34.8	0.2463	734.4	788.6	-6.2
22.0	38.1	0.2945	721.5	786.2	-6.7
24.0	41.5	0.3460	707.8	783.7	-7.1
26.0	44.8	0.4005	693.2	780.9	-7.4
28.0	48.1	0.4576	678.0	778.0	-7.8

3.K.3. Out of Plane Scattering Correction Checks

As mentioned in section 3.E., relatively large out of plane scattering corrections to the data were necessary because of the finite vertical acceptance of the HRS. These corrections were validated by calculating the spin observable, D_{nn}, using different vertical scattering angle bins. The $\pm 2^0$ vertical acceptance was broken up into 4 adjacent angular bins. D_{nn} was the same for all bins within error bars, eventhough the out of plane scattering corrections were basically zero for the two central bins ($\approx 0.5^0$) and 0.14 for the two outer bins ($\approx 1.5^0$). As seen in eqn 3-2, the out of plane scattering correction for D_{nn} has the form:

$$D_{nn}^{correction} = D_{ss}\langle \sin^2\phi \rangle / \langle \cos^2\phi \rangle \qquad (3\text{-}35)$$

Table 7 shows the validity of this correction. As seen there, D_{nn} was the same for the full vertical scattering angle acceptance as it was in the limited acceptance region ($\pm 1^0$), even though the out of plane scattering corrections were 0.14 with the full vertical scattering angle acceptance bin and only 0.05 for the limited acceptance bin.

Table 7 - Out of Plane Scattering Correction Checks

Vertical Scattering Angle	$D_{nn}^{correction}$	$D_{nn}^{corrected\ value}$
full bin ($\pm 2^0$)	0.14	0.86
$\pm 1^0$	0.05	0.86

4.A. The Proton Spin Observables Measured

The proton spin observables measured in this experiment are sometimes called the spin-transfer parameters. They are also referred to as the Wolfenstein parameters[1-8,9]. Basically they represent the probability of the proton changing its spin direction in the interaction. The definition of the $D_{\alpha\beta}$ in the center of mass (CM) system in terms of the pd scattering amplitude are given in section 1.E. Physically in the laboratory particle helicity frame they are defined as follows:

$$\begin{pmatrix} P'_s \\ P'_n \\ P'_\ell \end{pmatrix} = \left[\begin{pmatrix} D_{ss} & 0 & D_{\ell s} \\ 0 & D_{nn} & 0 \\ D_{s\ell} & 0 & D_{\ell\ell} \end{pmatrix} \begin{pmatrix} P_s \\ P_n \\ P_\ell \end{pmatrix} + \begin{pmatrix} 0 \\ P \\ 0 \end{pmatrix} \right] \frac{1}{1 + P_n \cdot A_y} \qquad (4\text{-}1)$$

where P_s, P_n and P_ℓ represent the incident proton beam polarization and P'_s, P'_n and P'_ℓ are the final state proton polarizations. The D's are the spin transfer parameters and P is the induced polarization. The induced polarization, P, is the final state proton polarization obtained with an unpolarized beam and target. From time reversal invariance $P = A_y$ where A_y represents the analyzing power. The analyzing power is the left/right scattering asymmetry produced by a 100% polarized beam ($\perp$ to the scattering plane) and is defined in eqns 3-11,12. Figure 4-1 shows physically what the spin transfer observables mean in the laboratory particle helicity system defined in section 1.E. Figure 4-1a shows the spin-transfer parameters and figure 4-1b displays A_y and P. For example, $D_{s\ell}$ is the ratio of the

scattered proton polarization in the longitudinal direction to the incident proton polarization in the sideways direction.

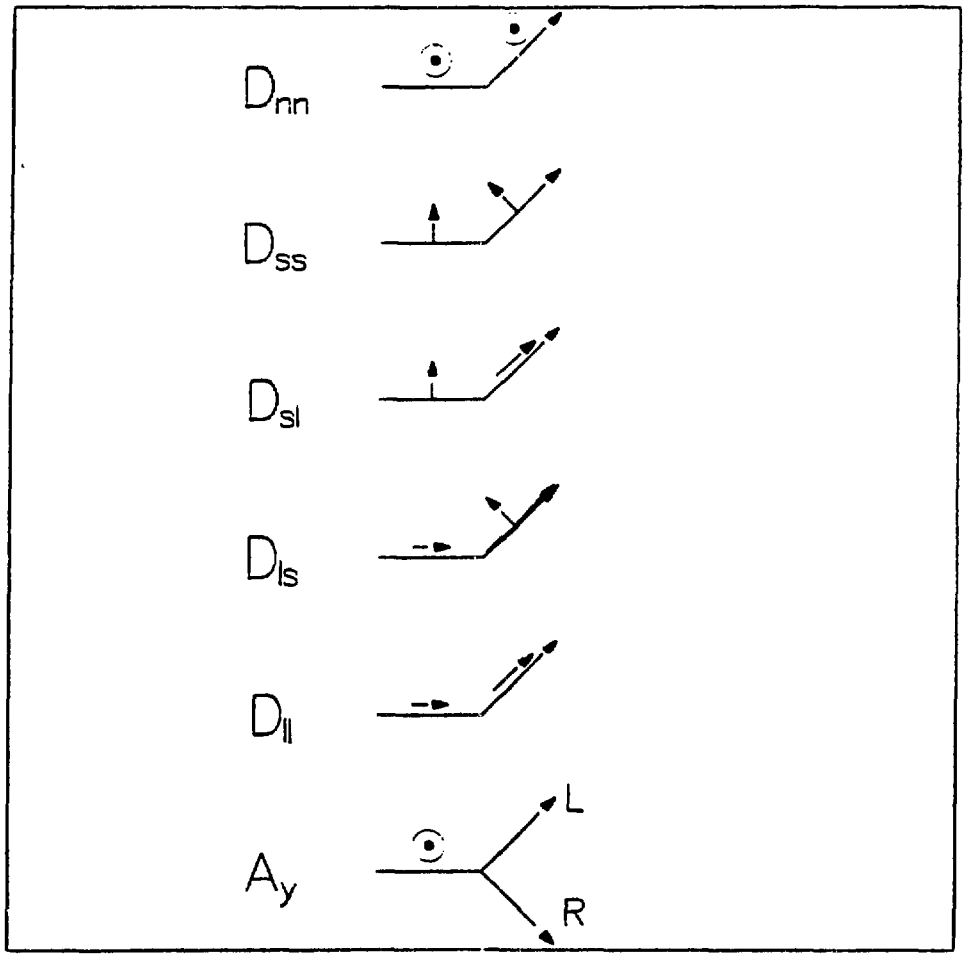

FIGURE 4–1A

Spin Transfer Observables

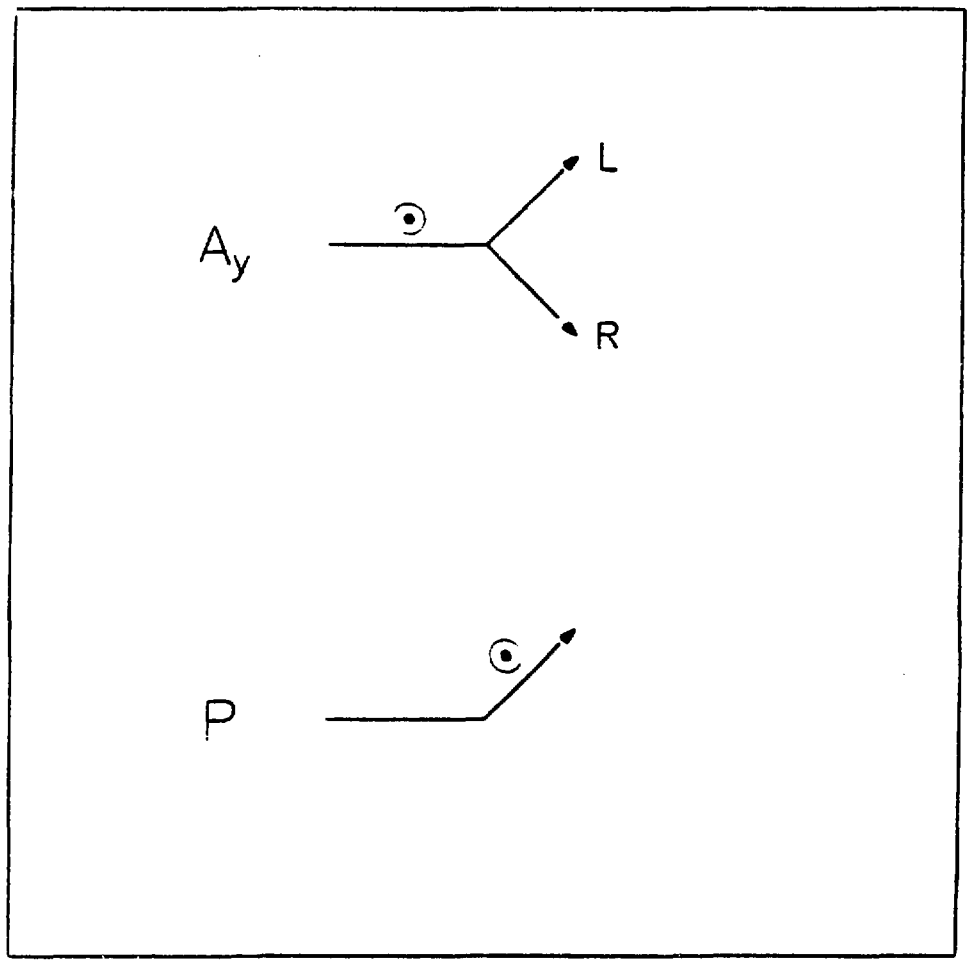

FIGURE 4–1B

Analyzing Power and Induced Polarization

4.B. The Data

The values of the Wolfenstein parameters and the analyzing power for $\vec{p}d \rightarrow \vec{p}d$ at 800 MeV are given in tables 8 through 13. The $\hat{\ell}$-type beam data were measured at 3, 6, 9, 12, 15, 18, 20, 22, 24, 26, 28^0. The $\hat{n}$-type beam measurements were made at the same angles out to 22^0 and the $\hat{s}$-type measurements went out to 20^0. The data were analyzed using two angular bins for each HRS setting, but only for the 3^0 $\hat{n}$-type beam point was the two-angular bin data used. For all other points all of the data for a particular HRS setting was used to determine a single data point. This was done in order to show the small angle depolarization ($D_{nn} \neq 1$) structure but to keep the statistical errors relatively small at all other momentum transfers measured.

Figures 4-2 through 4-7 show plots of the measured Wolfenstein parameters and the analyzing power along with their multiple scattering predictions. As seen in the figures, the non-eikonal multiple scattering calculation is in poor agreement with the data. The first minimum (actually a shoulder) in the unpolarized differential cross section[1-29] occurs at $-t \approx 0.45$ $(GeV/c)^2$, which is a laboratory scattering angle of $\theta \approx 30^0$. In general for p-nucleus scattering, the proton spin observables show rapid fluctuations only near the minima in the unpolarized differential cross section. Relatively large depolarization is seen at forward angles. This is rather unexpected and is not understood to date. As seen in figure 4-7, the fit to A_y is the best of all the observables. This is not

too suprising since A_y arises from the interference of single-spin-flip and non-spin-flip amplitudes.

In figures 4-8 through 4-13 the data of figures 4-2 through 4-7 are combined with all ready existing $\vec{p}d \to \vec{p}d$ data[1-29,30,33]. As seen, the discrepancies between the data and the calculation also exist at the larger momentum transfers. Note that the independent HRS and EPB data are in agreement in the region of overlap. Some possible explanations are presented in section 4.C.

FIGURE 4–2

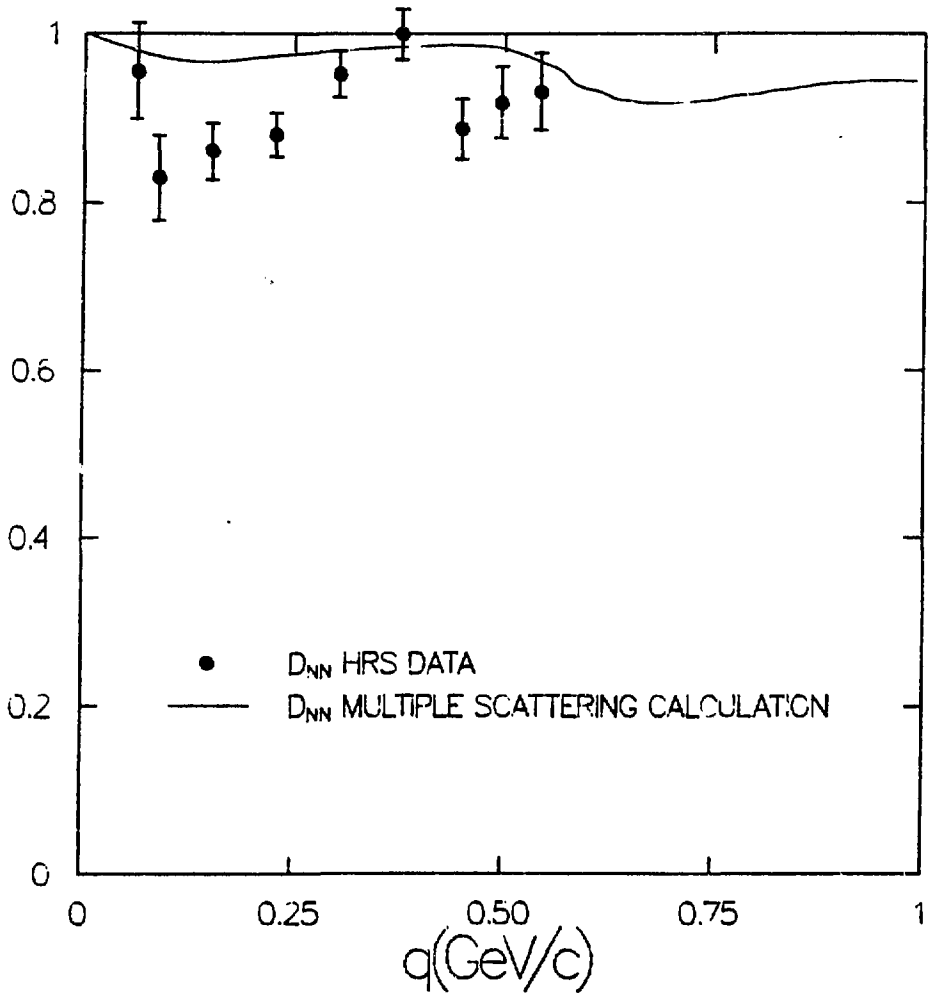

D_{nn} $\vec{p}d \rightarrow \vec{p}d$ at 800 MeV data of this thesis

FIGURE 4–3

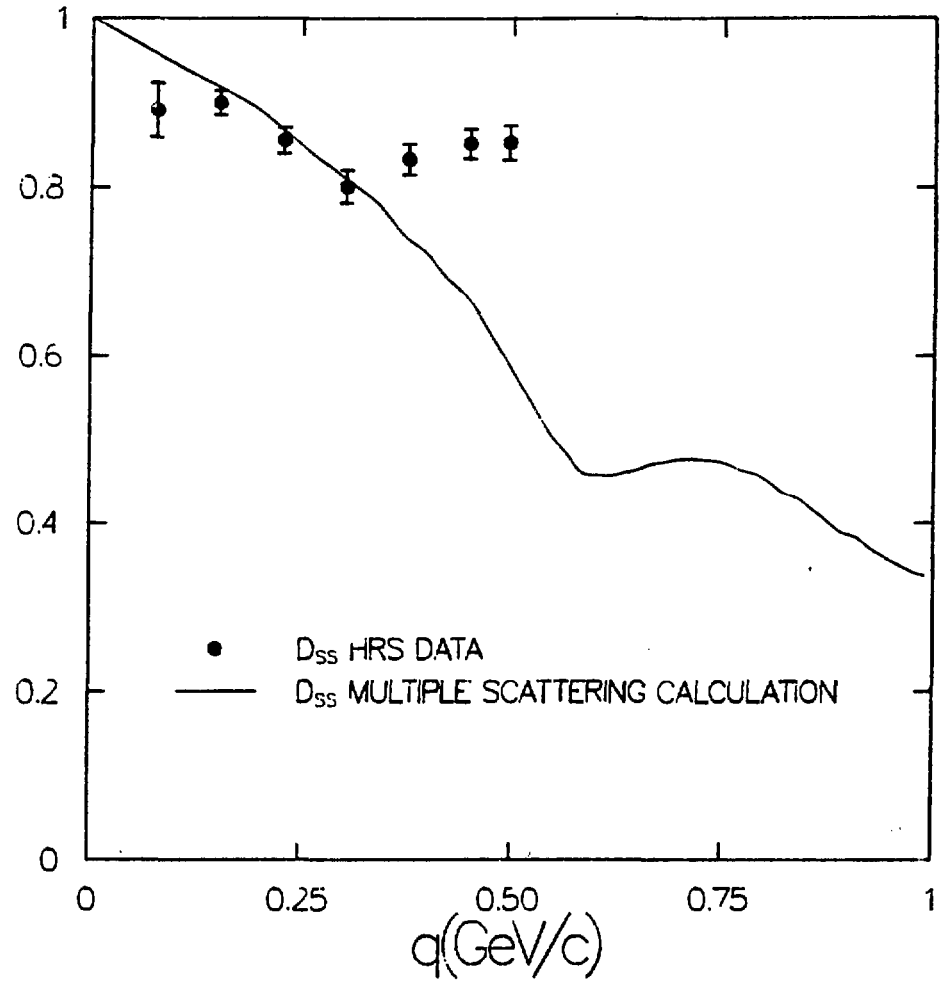

D_{ss} $\vec{p}d \rightarrow \vec{p}d$ at 800 MeV data of this thesis

FIGURE 4–4

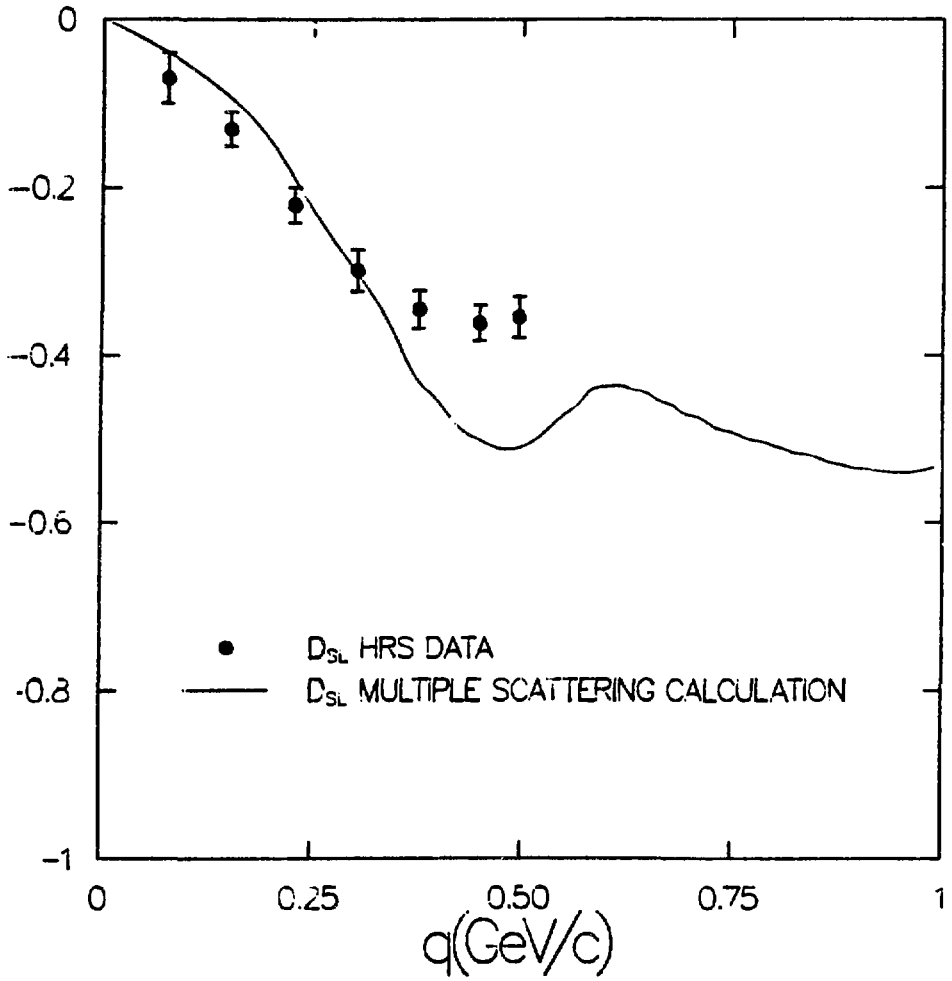

$D_{s\ell}$ $\vec{p}d \rightarrow \vec{p}d$ at 800 MeV data of this thesis

FIGURE 4–5

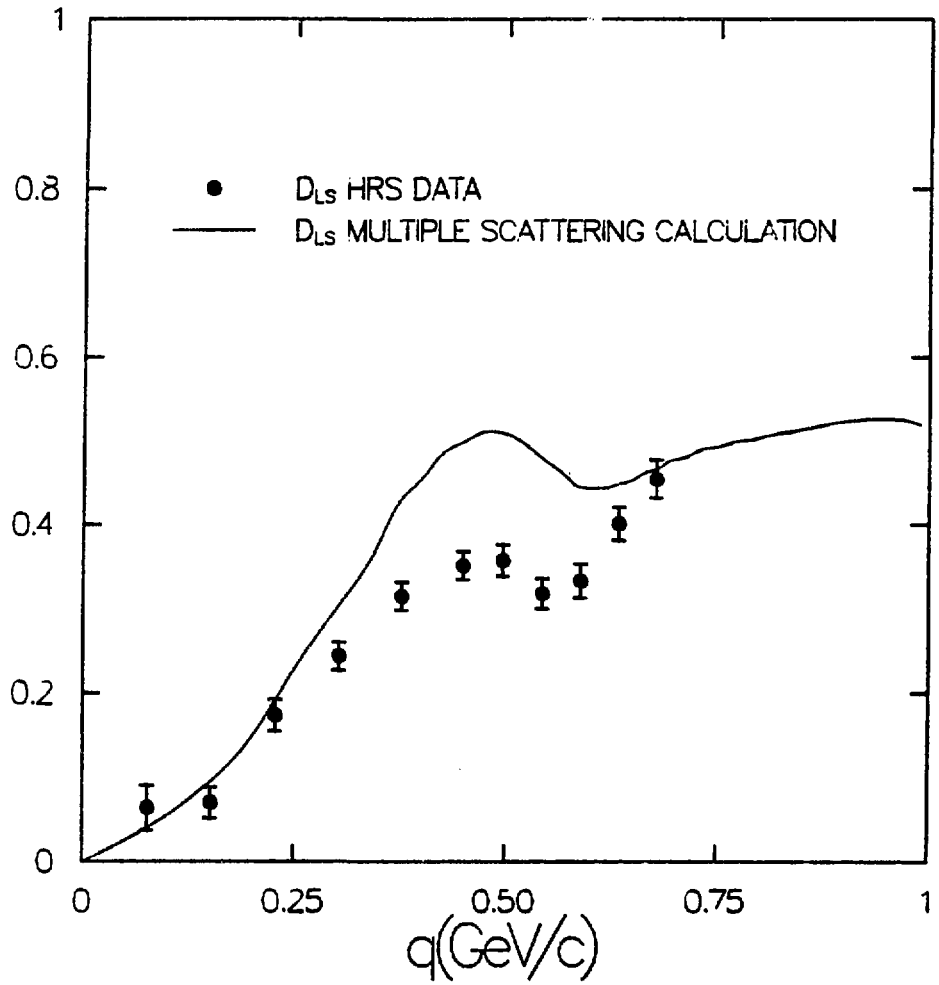

$D_{\ell s}$ $\vec{p}d \rightarrow \vec{p}d$ at 800 MeV data of this thesis

FIGURE 4–6

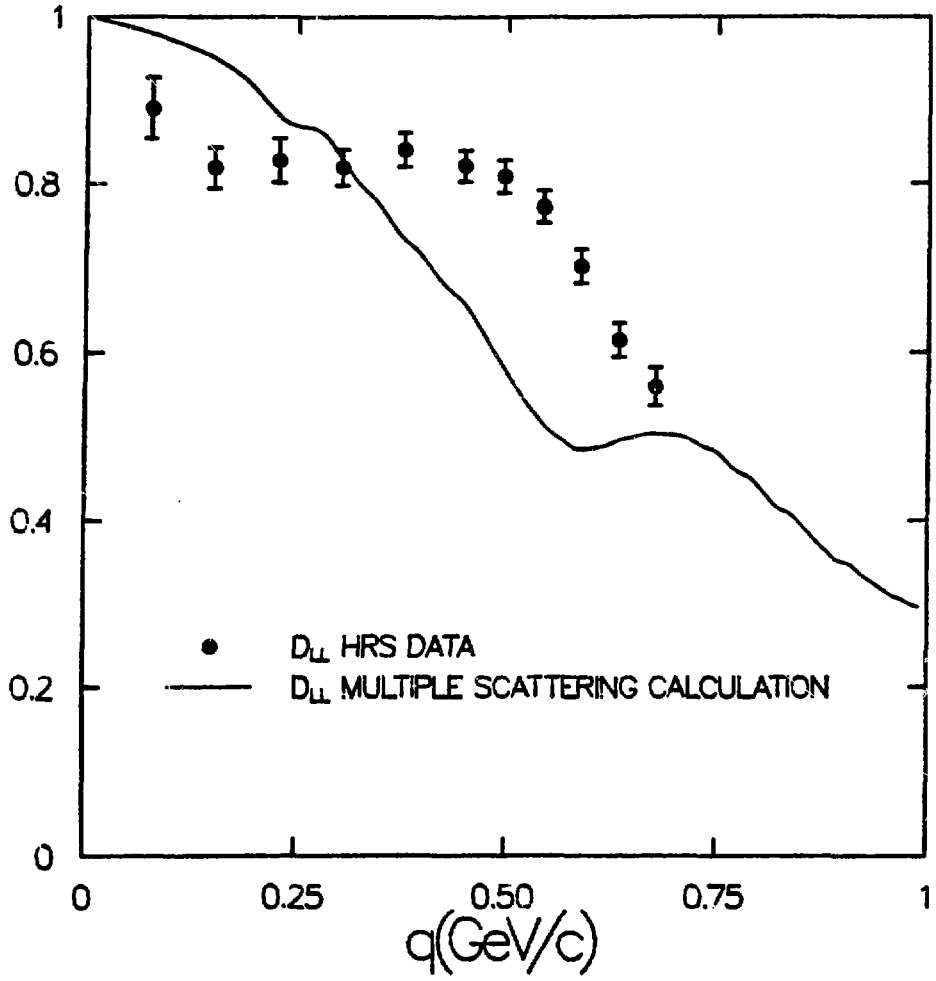

$D_{\ell\ell}$ $\vec{p}d \rightarrow \vec{p}d$ at 800 MeV data of this thesis

FIGURE 4–7

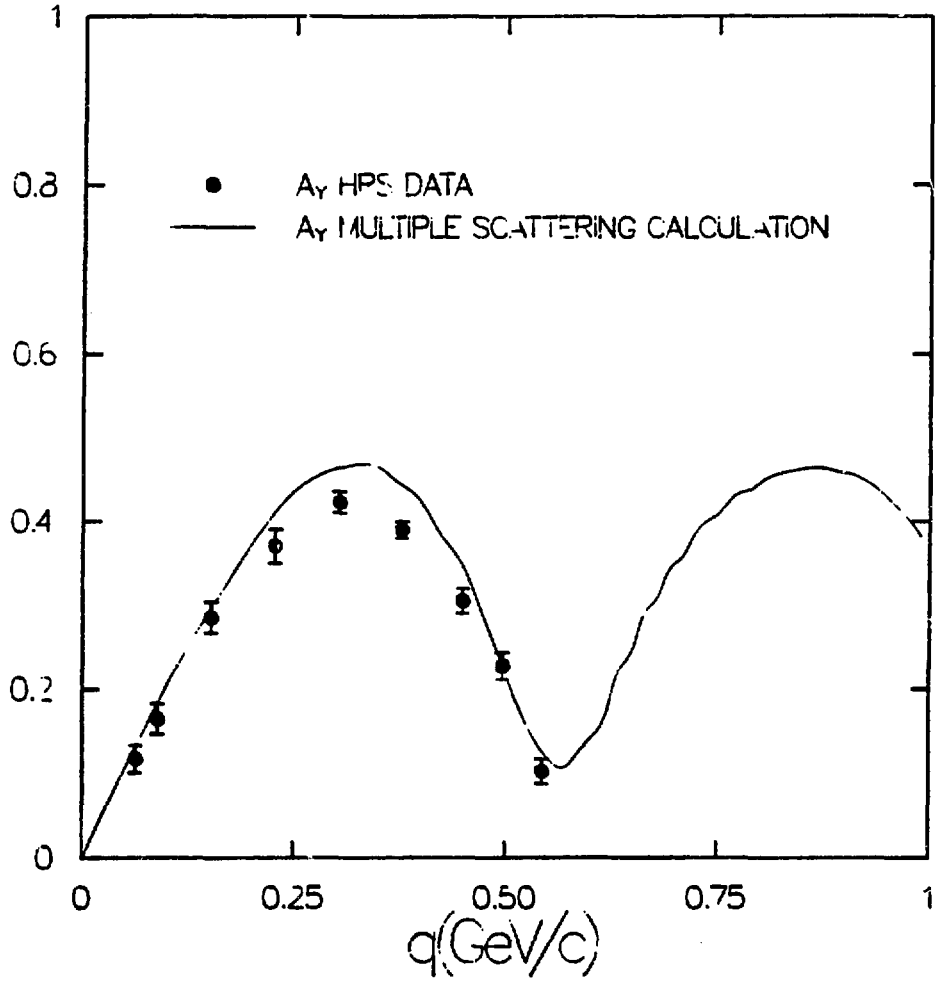

A_y $\vec{p}d \rightarrow \vec{p}d$ at 800 MeV data of this thesis

FIGURE 4–8

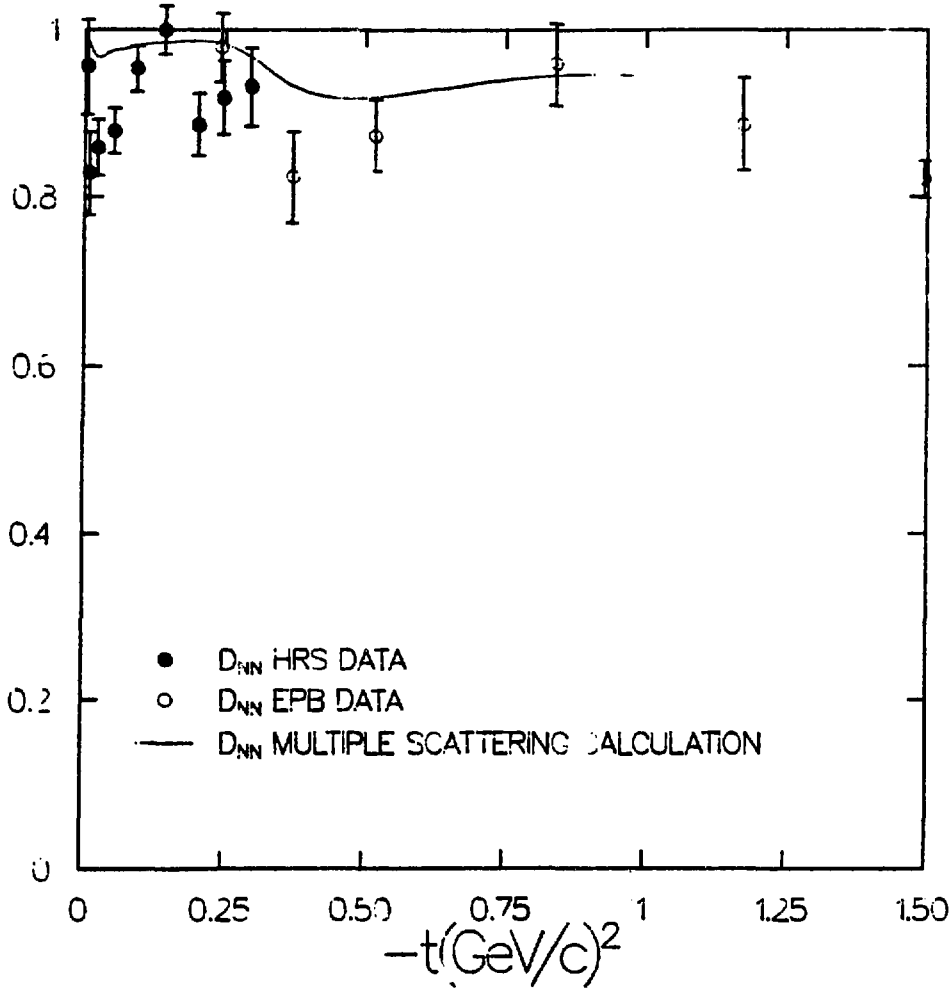

D_{nn} $\vec{p}d \rightarrow \vec{p}d$ at 800 MeV data combined with already existing data

FIGURE 4--9

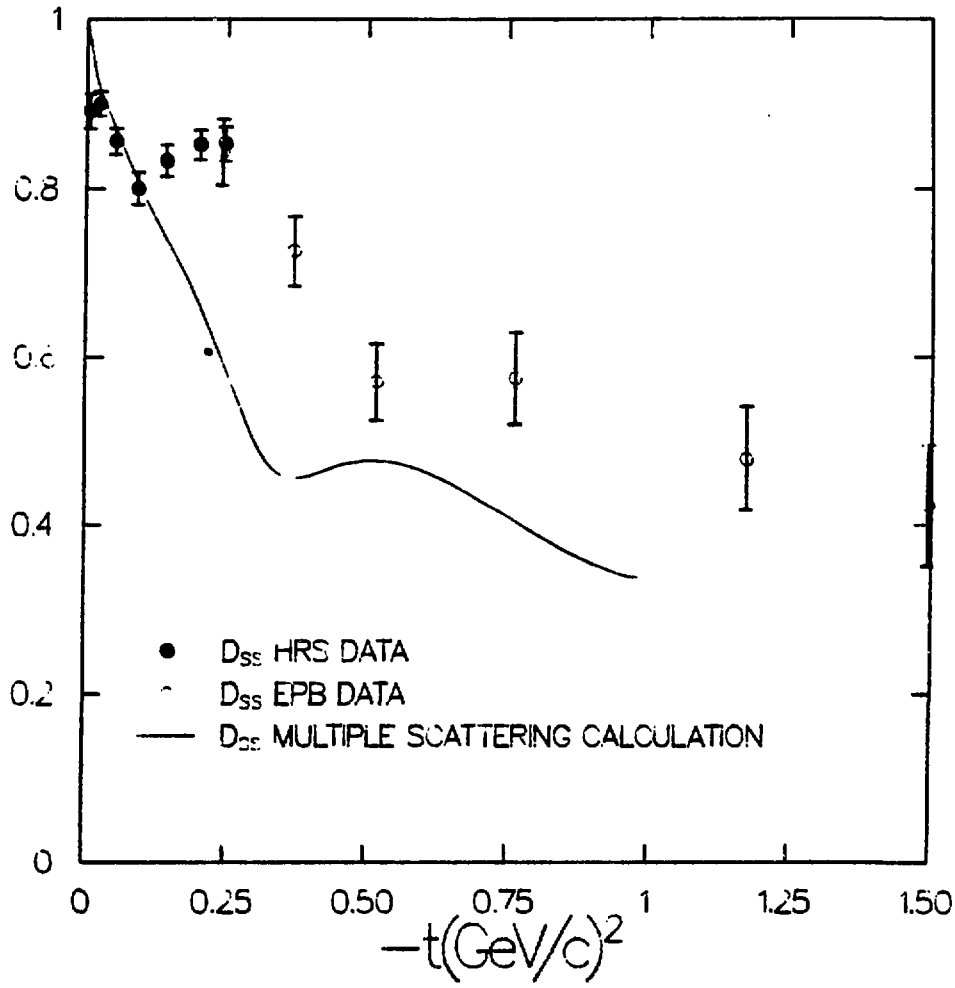

D_{ss} $\vec{p}d \rightarrow \vec{p}d$ at 800 MeV data combined with already existing data

FIGURE 4–10

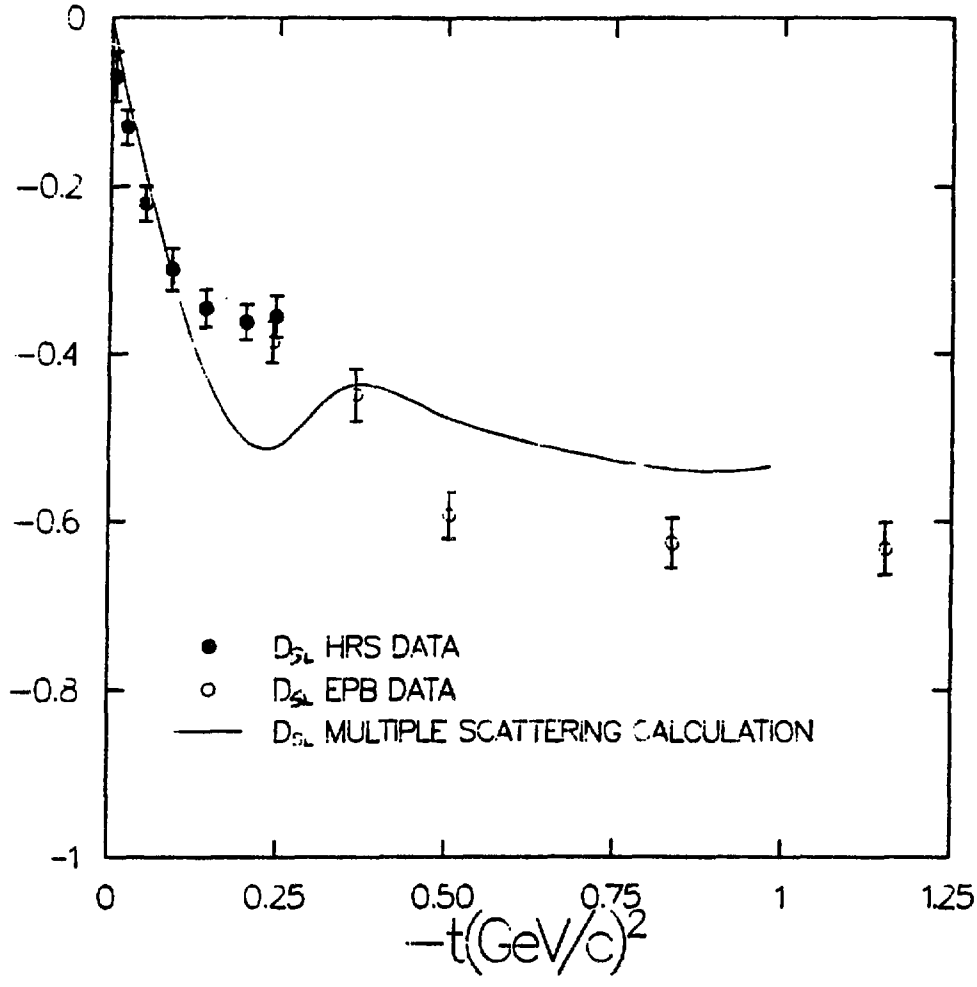

$D_{s\ell}$ $\vec{p}d \rightarrow \vec{p}d$ at 800 MeV data combined with already existing data

FIGURE 4—11

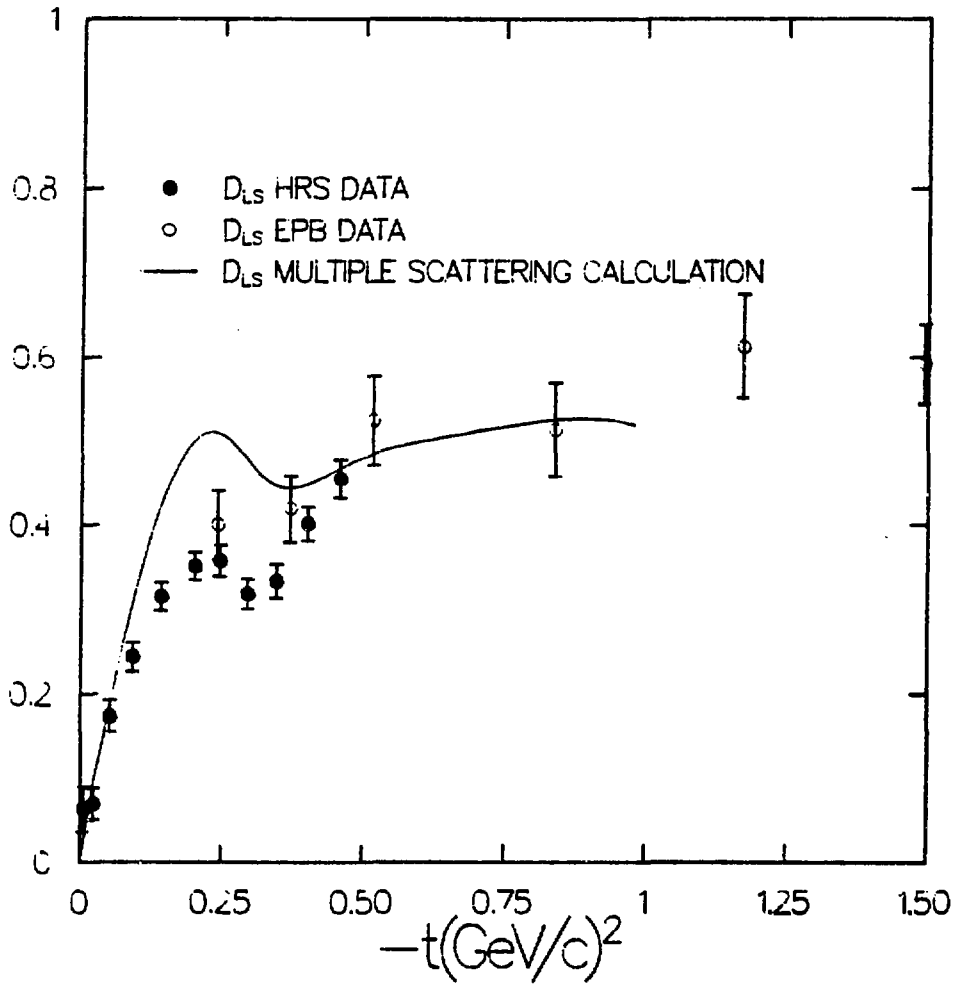

D_{ls} $\vec{p}d \rightarrow \vec{p}d$ at 800 MeV data combined with already existing data

FIGURE 4–12

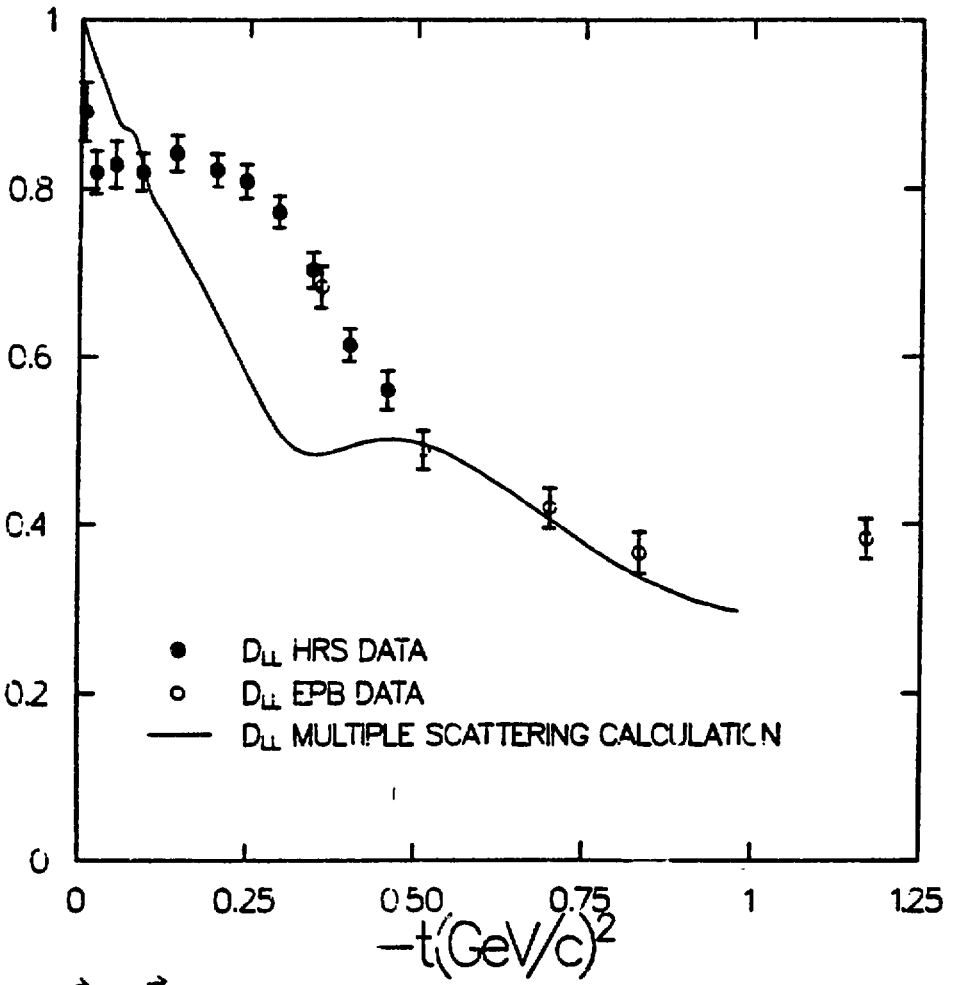

D_{11} $\vec{p}d \rightarrow \vec{p}d$ at 800 MeV data combined with already exixting data

FIGURE 4–13

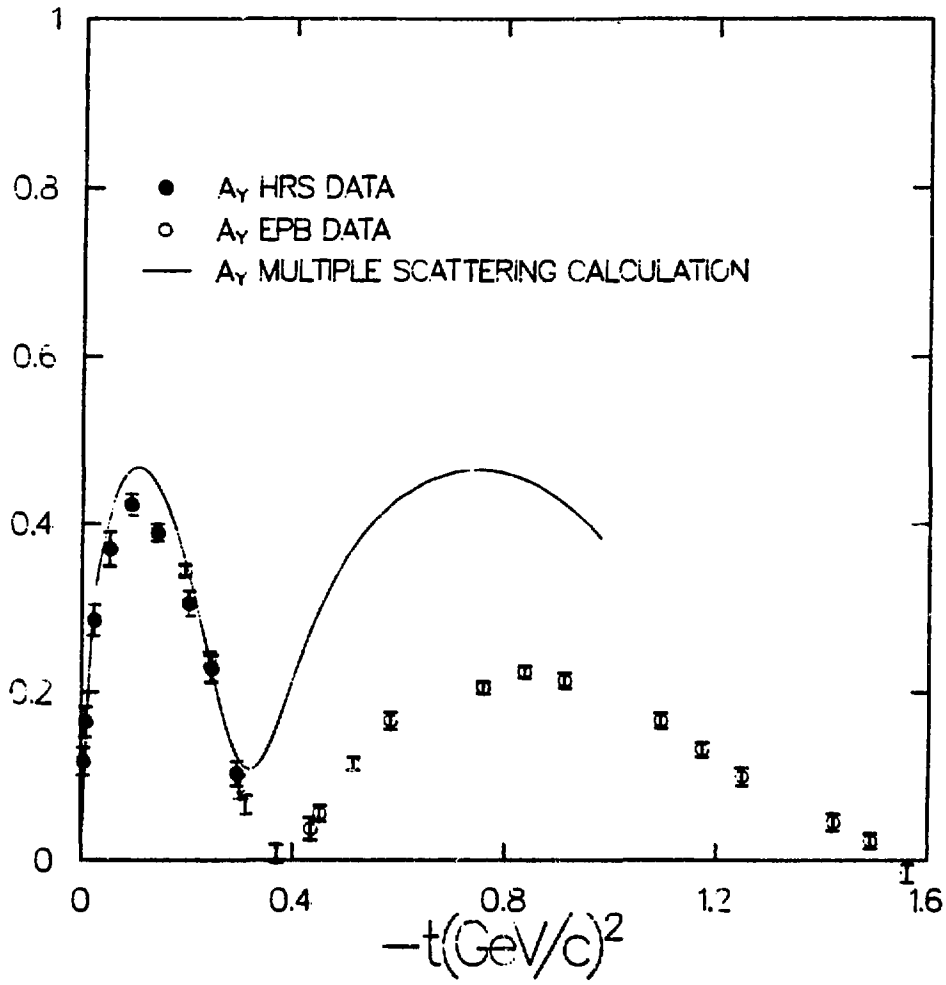

A_y $\vec{p}d \rightarrow \vec{p}d$ at 800 MeV data combined with already existing data

4.C. Conclusions

As seen in the figures of chapter 4, large discrepancies exist between the measured proton spin observables and the non-eikonal multiple scattering theory described in chapter 1. Also at the larger momentum transfers[1-31,33], the External Proton Beam (EPB) data at 800 MeV is in poor agreement with the multiple scattering calculation. The fact that these proton spin observables are not accurately predictable using the multiple scattering theory is very suprising since the deuteron tensor and vector observables are in good agreement with the same calculations[1-3,27] (see figure 4-14).

Several possibilities exist for these large discrepancies:

1) Ambiguities in the NN phase shift data.
2) Improper treatment of the approximations used in the current calculation.
3) Breakdown of the non-relativistic multiple scattering approach.

The poor agreement between the proton spin observable data and the multiple scattering prediction is in some way probably due to the calculation (reasons 1,2 or 3). As described in section 3.K., several systematic checks on the data were possible giving good reason to believe that the data are correct. Also as seen in figures 4-8 through 4-13, large discrepancies between the data and the calculation[1-7] exist at the larger momentum transfers (data taken in a completely different experimental setup-EPB). In the region of overlap, the EPB data agree quite well with the HRS data.

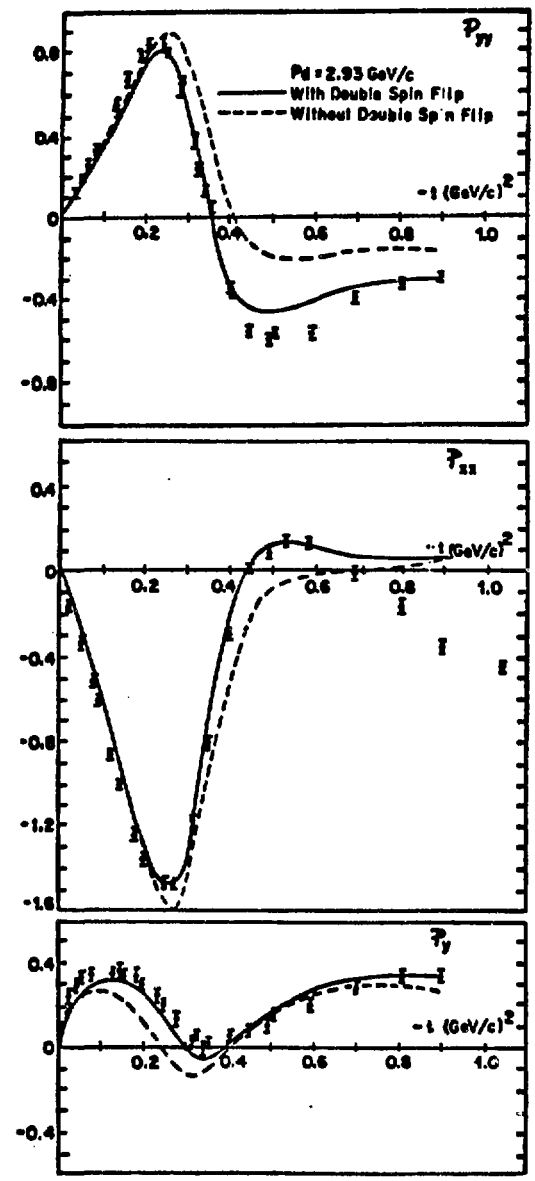

FIGURE 4-14

Deuteron observables
measured at ZGS facility

a completely different experimental setup-EPB). In the region of overlap, the EPB data agree quite well with the HRS data.

One possible explanation for the large discrepancies is 1). As described in section 1.C.1., the NN amplitudes, particularly the pn amplitudes, are not very well known at 800 MeV. But at 500 MeV, where the NN amplitudes are well known, the same proton spin observables for $\vec{p}d \to \vec{p}d$ are now in fairly good agreement with the same type of theoretical calculation[1-40]. Therefore, this could be the main reason for the disagreements. These data may be useful in constraining the pn amplitudes which are not so well known at 800 MeV (δ and ε, see section 1.C.1.).

Another possibility for the poor agreement could be that the approximations used in the current multiple scattering calculation are not valid. In the double scattering term several multi-dimensional integrals require approximations, see eqn 1-1. At the larger momentum transfers the double scattering contribution becomes large (the incident proton scatters from both the proton and the neutron of the deuteron). But at the very forward angles, double scattering is negligible and single scattering dominates (either from protons or neutrons). In view of these considerations, the large discrepancies between the theory[1-7] and the data at small momentum transfers are probably no a result of these approximations.

It could just be that the non-relativistic multiple scattering theory is not sufficient to predict these proton spin observables. If so, these discrepancies could disappear if a multiple scattering

theory based on the Dirac equation is put together. At the present time, the Dirac approach[4-1] is limited to an impulse approximation formalism but has had great success in improving the large problems that previously existed for proton-nucleus analyzing powers and spin rotation parameters in the intermediate energy range (300 MeV to 1 GeV) for medium to heavy nuclei. Its not clear whether or not this approach will result in improvements in the predictions of the pd spin observables[1-40].

In summary, the proton-deuteron elastic scattering data presented here should provide for a sensitive and very stimulating test of any theory to be used in the intermediate energy range (up to 1 GeV) for proton-nucleus scattering.

Table 8 - D_{nn} for $\vec{p}d \to \vec{p}d$ at 800 MeV.

Lab Angle	$-t(GeV/c)^2$	D_{nn}
2.5	0.0041	.956± .057
3.5	0.0080	.829± .050
6.0	0.0234	.860± .034
9.0	0.0522	.880± .027
12.0	0.0920	.953± .027
15.0	0.1420	1.000± .030
18.0	0.2016	.887± .037
20.0	0.2463	.919± .043
22.0	0.2945	.932± .046

Table 9 - D_{ss} for $\vec{p}d \to \vec{p}d$ at 800 MeV.

Lab Angle	$-t(GeV/c)^2$	D_{ss}
3.0	0.0059	.892± .033
6.0	0.0234	.901± .015
9.0	0.0522	.855± .016
12.0	0.0920	.800± .019
15.0	0.1420	832± .018
18.0	0.2016	.851± .018
20.0	0.2463	.852± .021

Table 10 - $D_{s\ell}$ for $\vec{p}d \to \vec{p}d$ at 800 MeV.

Lab Angle	$-t(GeV/c)^2$	$D_{s\ell}$
3.0	0.0059	-.069± .030
6.0	0.0234	-.131± .021
9.0	0.0522	-.221± .021
12.0	0.0920	-.300± .025
15.0	0.1420	-.346± .022
18.0	0.2016	-.362± .021
20.0	0.2463	-.355± .024

Table 11 - $D_{\ell s}$ for $\vec{p}d \to \vec{p}d$ at 800 MeV.

Lab Angle	$-t$ (GeV/c)^2	$D_{\ell s}$
3.0	0.0059	.063± .026
6.0	0.0234	.069± .018
9.0	0.0522	.174± .019
12.0	0.0920	.243± .017
15.0	0.1420	.316± .017
18.0	0.2016	.352± .016
20.0	0.2463	.358± .018
22.0	0.2945	.319± .018
24.0	0.3460	.334± .020
26.0	0.4005	.401± .020
28.0	0.4576	.455± .023

Table 12 - $D_{\ell\ell}$ for $\vec{p}d \to \vec{p}d$ at 800 MeV.

Lab Angle	$-t$ (GeV/c)^2	$D_{\ell\ell}$
3.0	0.0059	891± .036
6.0	0.0234	.819± .025
9.0	0.0522	.828± .027
12.0	0.0920	.819± .022
15.0	0.1420	.841± .021
18.0	0.2016	.821± .019
20.0	0.2463	.808± .020
22.0	0.2945	.772± .019
24.0	0.3460	.702± .021
26.0	0.4005	.614± .020
28.0	0.4576	.559± .023

Table 13 - A_y for $\vec{p}d \to \vec{p}d$ at 800 MeV.

Lab Angle	$-t(GeV/c)^2$	A_y
2.5	0.0041	.063± .026
3.5	0.0080	.165± .018
6.0	0.0234	.286± .019
9.0	0.0522	.370± .020
12.0	0.0920	.423± .013
15.0	0.1420	.389± .010
18.0	0.2016	.306± .015
20.0	0.2463	.227± .016
22.0	0.2945	.102± .015

A.1. Polarized Deuterium Target and its associated Hardware

A $\vec{p}\vec{d}\rightarrow\vec{p}d$ experiment was done at 800 MeV at the HRS in September/October 1983 using a polarized proton beam, polarized deuteron target and measuring the polarization of the outgoing proton. Although the data of this experiment have not been analyzed yet, sections A.1. through A.6. are devoted to describing the experimental setup.

The deuterium target used was polarized using a horizontal dilution refrigerator[A-1,2] with high cooling power for operation in the frozen spin mode. The dilution refrigerator pumps on the $^3He/^4He$ dilution phase and in conjunction with a high cooling capacity enables the target material to cool to a temperature of about 20 - 100 mK. This dilution phase is the phase where ^3He and ^4He are separated below the critical temperature (see Figure A-1). The upper phase is richer in ^3He than the lower phase. The lower part (dilute phase) is superfluid (^4He) but plays no significant thermodynamic or hydrodynamic role at low temperatures. Therefore, the ^3He of the dilute phase in the lower part behaves like an ideal gas. When ^3He dilutes from the ^3He rich phase to the dilute phase it has a cooling power of[A-3]

$$dQ/dt = dn/dt(95T^2 - 12T_I^2) \qquad (A-1)$$

where dn/dt is the ^3He flow rate into the dilute phase in mole/sec, dQ/dt is the cooling power in watts and T is the temperature (K) of

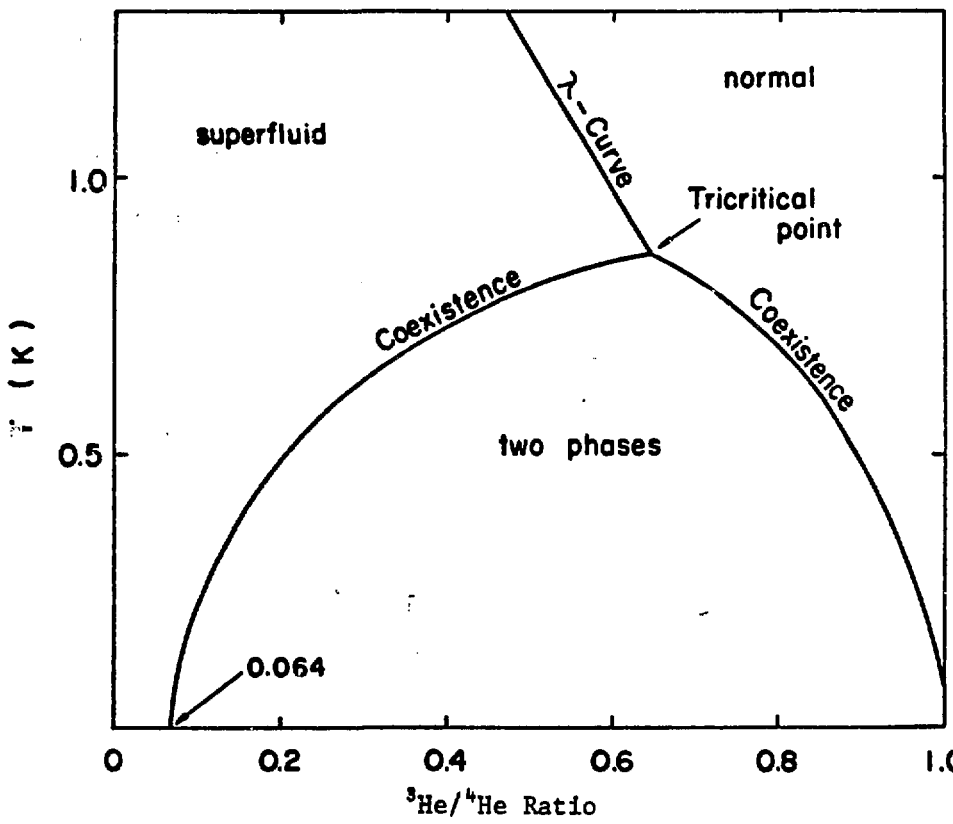

FIGURE A-1

Helium phase diagram

the mixing chamber in which the phase separation occurs. T_i is the temperature (K) of the incoming concentrated stream to the mixing chamber. At these low temperatures, the nuclear spin relaxation time is quite long (~100 hours at 10 KG magnetic field) thus " freezing in " the target polarization. This allows data to be taken in a holding mode which requires a lower and less homogeneous magnetic field than the polarizing field. In the holding mode, the microwaves which are used for polarizing, are turned off. Deuteron polarizations of ~40% were obtained in the experiment. Figure A-2 is a schematic view of the dilution refrigerator.

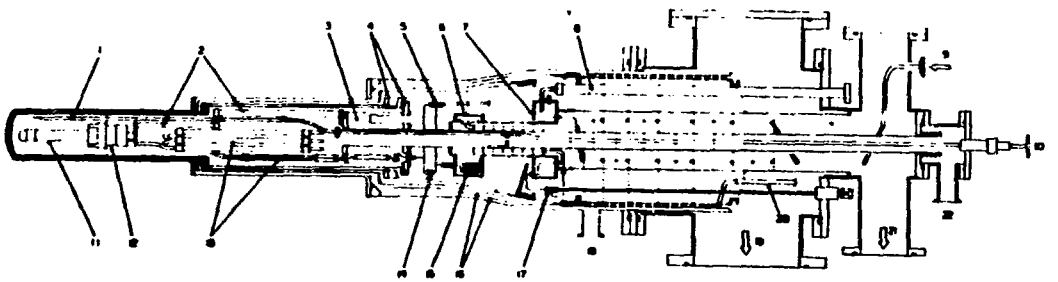

Fig. 1. Schematic view of the horizontal dilution refrigerator. 1. waveguide; 2. supporting pipe; 3. still; 4. indium seal flanges; 5. ^{3}He inlet needle valve; 6. ^{4}He evaporator, 7. ^{4}He gas separator; 8. liquid ^{3}He transfer line; 9. ^{3}He gas inlet; 10. microwave inlet; 11. PFA (teflon) target holder; 12. brass joint; 13. heat exchangers; 14. calibrated capilla tube; 15. ^{3}He condenser; 16. radiation shields; 17. ^{4}He needle valve; 18. cryostat insulation vacuum pumping line; 19. ^{3}He pumping line; 20. separated ^{4}He gas pumping lir 21. ^{4}He pumping line; 22. mixing chamber insulation vacuum pumping line.

FIGURE A-2 Horizontal dilution refrigerator

A.2 Cooldown and Polarization Process

First the refrigerator is cooled down from room temperature using liquid Nitrogen (77K). Using a transfer line, liquid ^{4}He is then transferred to the ^{4}He gas separator, which separates the ^{4}He liquid from the ^{4}He gas evaporated in the transfer process. The liquid ^{4}He then flows through precooling pipes to the evaporator. ^{4}He pumps are constantly used to pump on the ^{4}He at both the separator and the evaporator. The ^{3}He circulation is mostly independent and isolated from that for the ^{4}He and is pumped on by a separate ^{3}He pump package. The ^{3}He , as it enters the refrigerator, is precooled by both the separator and the evaporator through the heat exchangers. Liquid ^{4}He continually enters the separator (~5 liters/hour) so the temperature of the separator stays at roughly liquid ^{4}He temperature (4.2K). The evaporator is typically at 1.5K because the ^{4}He is being pumped on there. Concentrated ^{3}He gas is injected through the gas handling system at a very high rate (~6 standard liters per minute) and is liquified in the still after being pre-cooled as explained above. It's cooled down to the still temperature through a still heat exchanger. It then goes through a special heat exchanger , where it's cooled by the dilute ^{3}He phase returning from the mixing chamber, and into the mixing chamber (where the target flask resides). In normal operation, in the still we pump almost exclusively on ^{3}He (over 90% ^{3}He) because the vapor pressure of the ^{3}He is much higher than that of ^{4}He at the still temperature, which is typically 700 mK (the critical point temperature for the

$^3He/^4He$ dilution or coexistence phase), as shown in Figure A-1. The still temperature is 700 mK because the still is heated by the still heater in order to obtain a large ^3He pumping rate. By the final cooling stage, the mixing chamber has reached a temperature of 20 - 100 mK. The ^3He circulation system is shown in Figure A-3.

After the cool down procedure has finished, the Zoltan electromagnet with its vertical magnetic field (normal to the scattering plane) is powered up to a magnetic field of 25 KG. With this field and temperature (without microwaves) an extremely small deuteron polarization (<<1%) is induced due to the Boltzman thermal distribution expected. The Boltzman distribution has the following form:

$$n1/n2 = \exp[-\Delta E/kT] \qquad (A-2)$$

where n1 and n2 are populations of levels 1 and 2. Here ΔE is the energy difference between the two levels in the magnetic field. Under the same conditions, the electrons in the target material are almost completely polarized (>99%) because of the large energy splitting due to their relatively large magnetic moment. That is, all the electrons are in the same spin state (lowest energy).

In order to understand the deuteron polarization process , consider the simpler situation of polarizing protons. The proton polarization process occurs by impinging 70 GHz microwaves into the target material inducing transitions between the energy levels, see

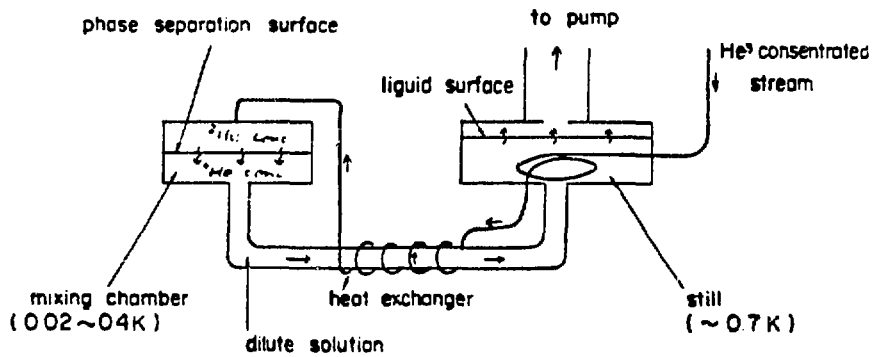

FIGURE A-3

^{3}He circulation system

fig. A-4. As seen in this figure, the up polarization is obtained by transitions between levels 2 and 3. The down polarization is attained by transitions between levels 1 and 4. In both cases, polarizing flips both the electron and proton spins. The electrons have an extremely small relaxation time (of the order of msecs) due to their large magnetic moment. Without microwaves, levels 1 and 2 are nearly equally populated and levels 3 and 4 are almost totally unpopulated. Once the polarization has built up to roughly its maximum value (~80% for protons, ~40% for deuterons), see figure A-5, the magnetic field can be decreased to its holding field of 10 KG, because the nuclear spin relaxation time of the target is still very long as shown in Figure A-6 as a result of the very low temperature. During the polarizing process, the target heats up due to the polarizing microwaves. When data is being taken (no microwaves during data taking) the beam heats up the target. The energy level scheme of deuterium in a magnetic field is somewhat more complicated (6 levels) than that of the proton system. For details see ref A-7.

During the polarization process, the target polarization is measured using an Nuclear Magnetic Resonance (NMR) system[A-4,5,6]. Microwaves of 16.3 MHz (corresponding to the deuteron magnetic resonance (DMR) - see Figure A-7 are sent into the target meterial to measure the polarization by exciting the DMR and measuring their absorption. As seen in fig. A-7, the DMR spectrum is a very good

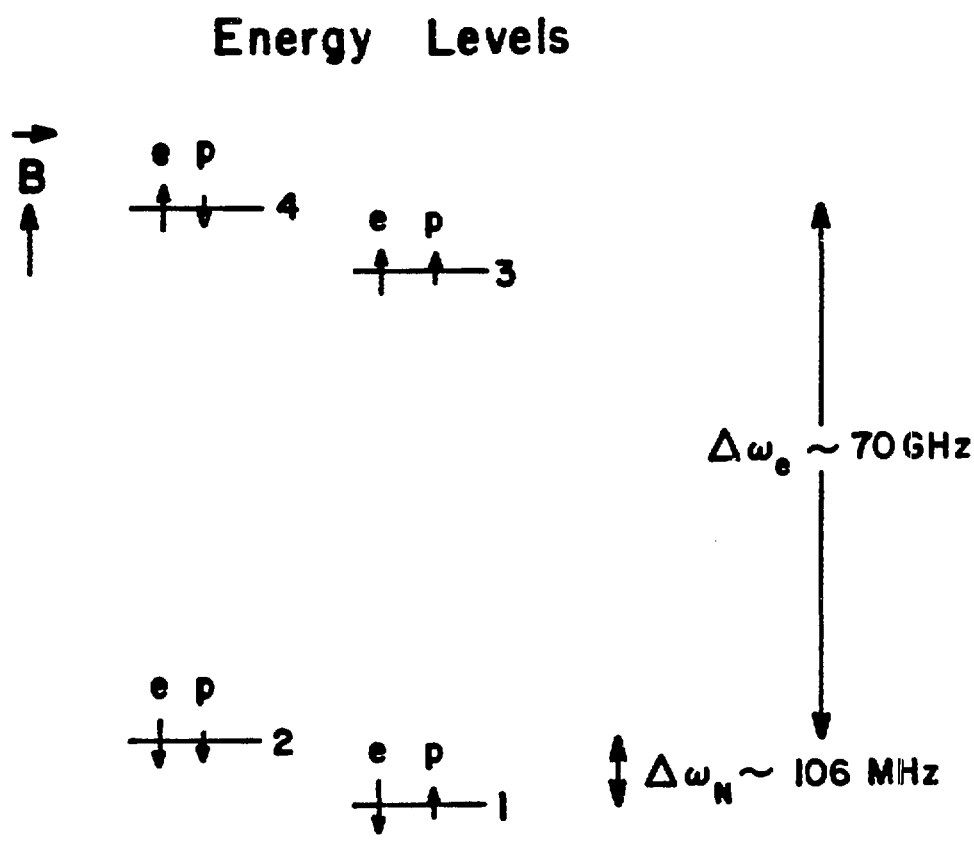

FIGURE A-4

Energy level diagram for polarization

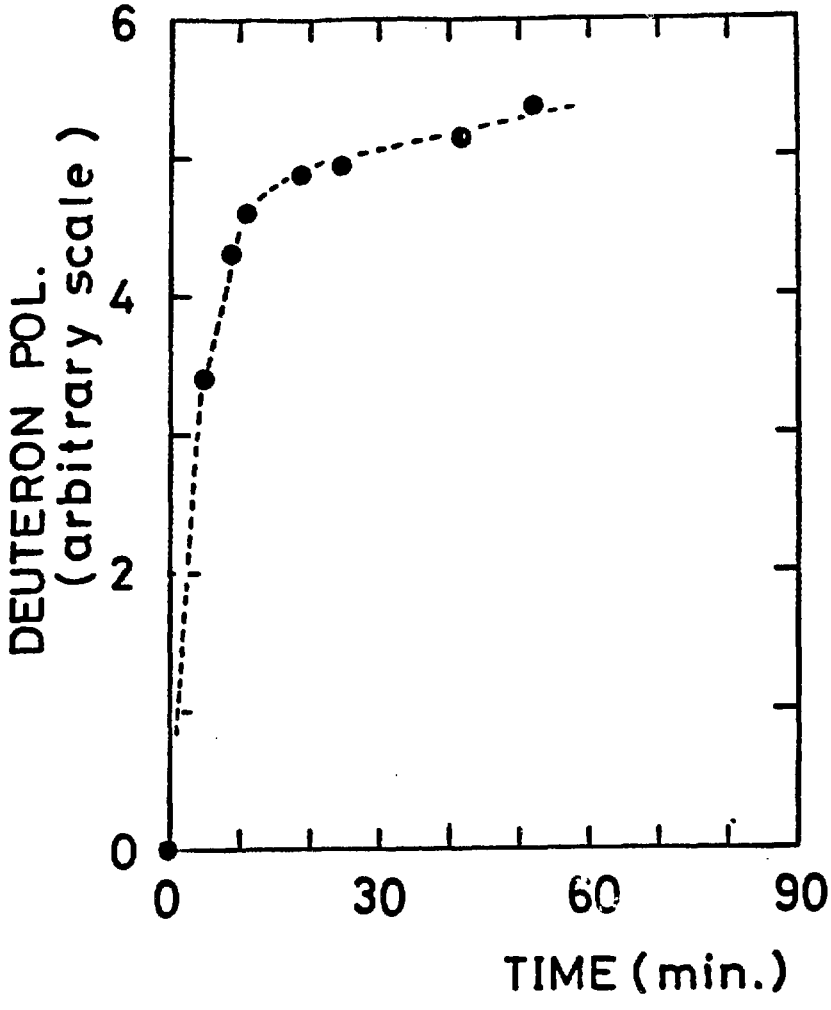

FIGURE A-5

Deuteron polarization vs time

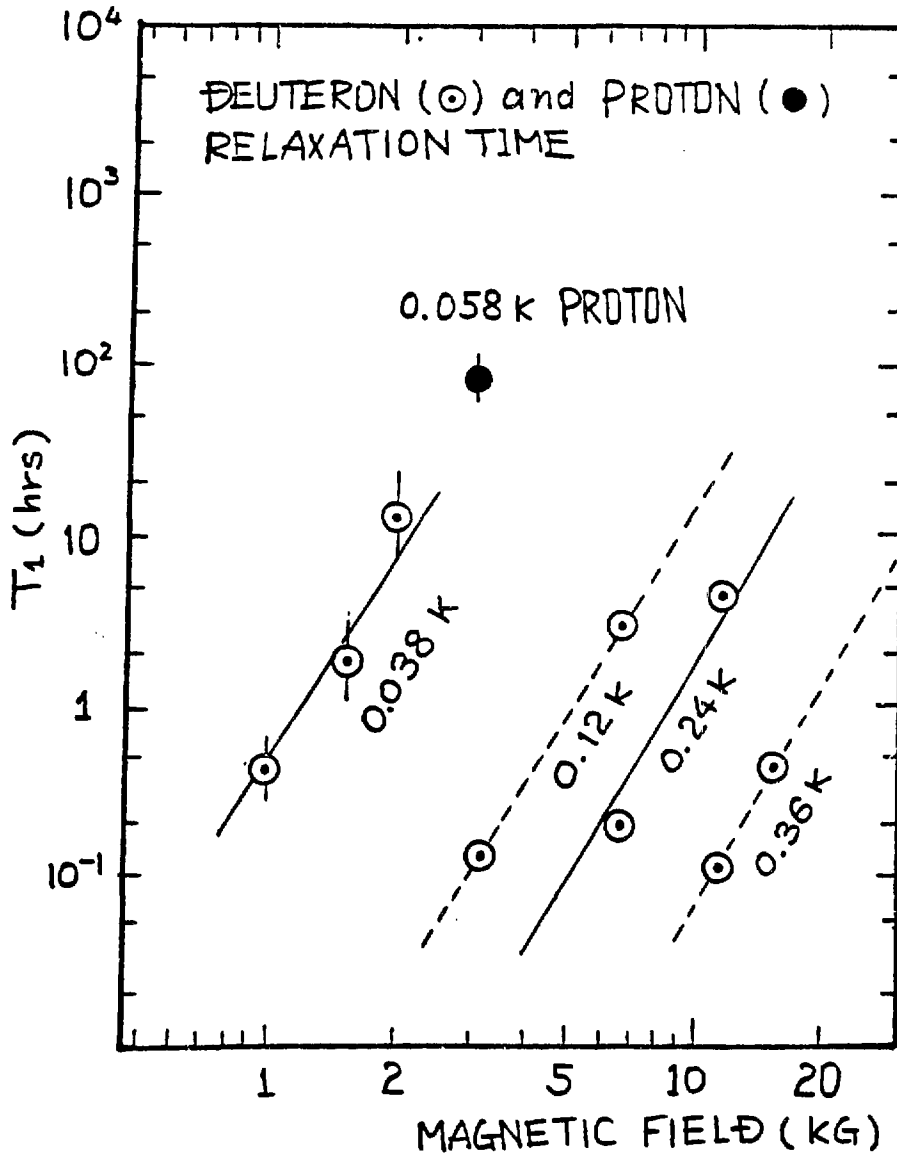

FIGURE A-6

Polarization relaxation data

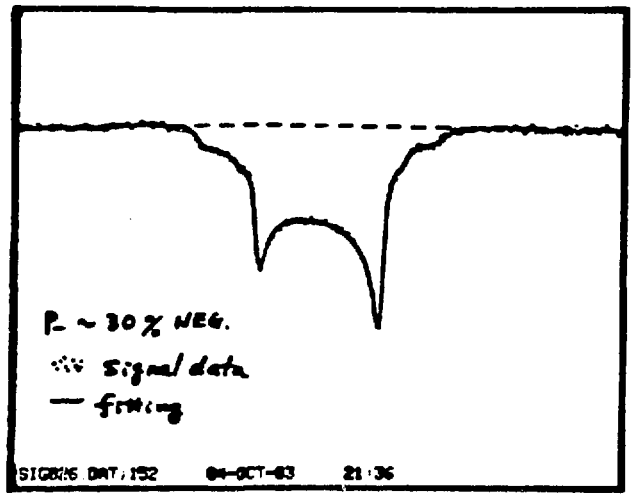

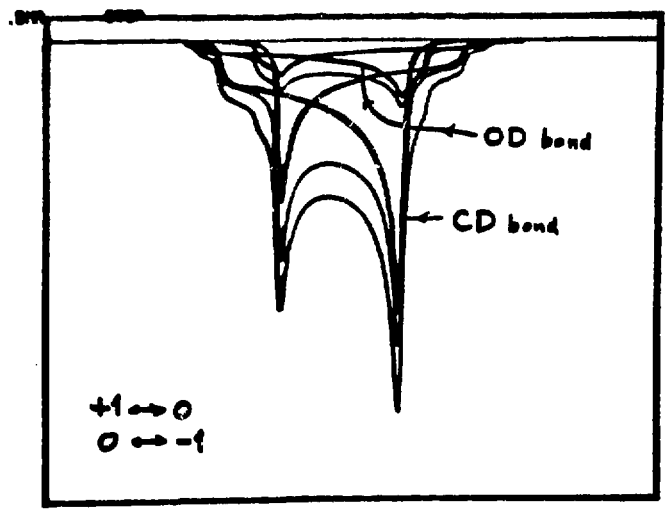

FIGURE A-7

Deuteron magnetic resonance signal

fit but its not completely understood at this time (drifting electronics etc.). The deuteron polarization is given by

$$P = \frac{4\tanh(\hbar\nu/2KT_s)}{3+\tanh^2(h\nu/2KT_s)} \qquad (A-3)$$

where ν = Larmor frequency and T_s = deuteron spin temperature.

So the target polarization depends only on temperature. Calibrated Spear carbon resistors were used to measure the temperature at various places within the dilution refrigerator.

During the time data was being taken, the target depolarized primarily due to beam heating effects, since the spin - relaxation time was of the order of 100 hours at its temperature of ~50 mK in a 10 KG holding magnetic field. As long as the beam intensity was kept low enough, ($\sim 10^6$ protons/sec cm^2), beam heating effects were not serious and the target stayed polarized at ~35% for hours, even with the holding magnetic field of just 10 KG.

A.3 Target Material and Flask

The target material is made of Propanediol-D8 ($CD_3CD(OD)CD_2OD$) doped with a chromium complex EHBA ($Na((C_2H_5)_2C_2O_3CrOC_2O_3(C_2H_5)_2)H_2O$). In its proper proportions, the target sample contains 18% deuterium, 43% carbon, 38% oxygen by weight. The target flask is made of PFA - teflon and is 4cm x 2.5cm x 2cm. The target material consists of beads 1.5 mm in diameter in order to polarize and as a consequence has a packing factor of about 65% by volume[A-1]. Empirically the packing factor appears to be larger (~80%). This was inferred from the comparison of proton-carbon yields using the target material and liquid hydrogen-propaindiol at room temperature[A-12]. The proton beam also sees the vacuum jackets and windows associated with the dilution refrigerator which are made of stainless steel and copper - see figure A.2.

A.4. Polarized Target Hardware

In addition to the horizontal dilution refrigerator, there was considerable hardware required for the polarized target. A brief description of the major hardware used is given below.

1. ^{3}He Pump Package - This pump package consisted of a rough pump, roots blower and a few mechanical pumps used to pump on the ^{3}He in the still.
2. ^{4}He Pump Package - This pump package also was made up of a rough pump, roots blower, and a few mechanical pumps used to pump on the ^{4}He in both the separator and the evaporator.
3. Gas Handling System - The gas cart consisted of a liquid Nitrogen cold trap, a rough pump, a ^{3}He transfer pump, pressure gauges, many valves and pieces of copper tubing etc. Its main purpose was to control the flow of gas in all modes of operation - normal operation, restoring ^{3}He and ^{4}He to the storage tanks, putting ^{3}He in the system, evacuating the system etc.
4. Storage Tanks - There were 3 large (142, 346 and 411 liter) storage tanks used to store ^{3}He, ^{4}He and the largest one was used as a relief tank in case of an over pressure situation or emergency at any spot in the polarized target setup.
5. 1000 liter ^{4}He Dewar - This was used as the liquid ^{4}He supply for the separator. ^{4}He was constantly being consumed at a rate of ~5 liter/hour to cool the refrigerator.

6. Carcinotron - The carcinotron is the high power microwave unit used to supply the ~70 GHz microwaves necessary for polarizing. Its microwave frequency was easily changed by ~400 MHz (a few times the NMR frequency) in order to switch the target polarization from up to down or vice versa. The Carcinotron was powered by a large HV power supply.

7. NMR/DMR Hardware - This basically consisted of an oscillator, frequency counter and some amplifier circuits which together generate a signal used to measure the target polarization by exciting the DMR and measuring its absorption.

8. PDP 11/34 Computer with a Microprogrammable Branch Driver and Camac Hardware- The computer and Camac hardware was set up to read the DMR signal and calculate the target polarization[A-5,6]. This was done only during polarization periods (with 25 KG magnetic field), not during data taking when the magnetic field was 10 KG and off the 16.3 MHz DMR.

9. Movable Platforms - There were two large movable platforms used to move the dilution refrigerator and the 1000 liter ^{4}He dewar (which were connected by a rigid transfer line) away from the target pivot point at the center of the magnet's pole face in order to move the solid target mechanism into an operable position in the beam.

10. Solid Target Mechanism - This device was used to insert any one of eight different solid targets into the pivot point region. For

example CD_2, ^{12}C, ^{208}Pb, etc. targets were needed for beam tuning and other calibrations.

A.5. Deuteron Magnetic Resonance - Target Polarization

One of the methods for determining the deuteron target polarization used a deuteron magnetic resonance (DMR) system. In a 25 KG magnetic field the DMR is at a frequency of 16.3 MHz. By measuring the absorption of this 16.3 MHz signal, the relative deuteron target polarization is attainable. A typical DMR spectrum is given in figure A-7. As seen, two peaks of different frequency occur as a result of the electric quadrupole interaction of the deuteron in a magnetic field. The area under the spectrum or equivalently the sum of the two peak heights give a relative value of the deuteron target polarization. These relative values will be normalized to the value of target polarization determined by a fit of the signal line shape which provides the ratio of the two transition intensities. Another independent method for normalizing these DMR polarization values is by the measurement of the left/right scattering asymmetry with the HRS at 12.5^0 (maximum of deuteron vector analyzing power).

A.6. Monitor System

A set of MWDCs and scintillators was used in order to independently determine the target and beam polarizations. The left/right proton-proton quasifree scattering coincidences were detected using ten scintillators. The MWDCs were used to only cut slightly on the background since the the quasifree spectra are so broad.

This monitor system is based on the fact that deuterium is a spin 1 object. Therefore, the protons in the deuterium basically have the same vector polarization as that of the deuterons. The pp cross section for quasifree scattering from deuterium at 17^0 (maximum in pp analyzing power) is higher than the pd elastic scattering cross section at 40^0 (second maximum in pd analyzing power, the first maximum is at 15^0 and the deuterons do not get out of the target because of their low energy). The carbon and oxygen of the propaindiol target sample also contribute to the pp yields but have no scattering asymmetry since they are not polarized (spin 0 nuclei). This method for determining the deuteron target polarization is independent of the DMR method described in section A.5. More work has to be done before the monitor system data can be proved to be useful.

A.7. Nucleon-Nucleon Measurements at EPB

As mentioned in section 1.C.1., we have participated in some nucleon-nucleon (NN) experiments at the External Proton Beam (EPB) area at LAMPF. The work was done with B.E. Bonner et. al.[1-35-37]. These experiments are listed with their respective energies in table 14. As seen in the table, pp elastic and inelastic spin transfer measurements were made at energies between 600 and 800 MeV. The purpose of the pp elastic experiments is to complete the T=1 NN amplitude measurements at intermediate energies which are used as input to proton-nucleus calculations and to map out their energy dependence. We measured D_{ss}, $D_{\ell s}$, $D_{\ell\ell}$ and P for $\vec{p}p \to \vec{p}p$ at 600, 650, 700 and 750 MeV. The reactions $\vec{p}p \to \vec{p}n\pi^+$ and $\vec{p}p \to d\pi^+$ were done in order to look at the NN inelastic channels to help awnser the questions with regards to the possibility of dibaryon resonances and threshold type behaviours. We measured D_{nn} for $\vec{p}p \to \vec{d}\pi^+$ and D_{nn}, P and A for $\vec{p}p \to \vec{p}n\pi^+$ at 800 MeV. See refs 1-35,36,37 for more details.

Table 14 - EPB Nucleon-Nucleon Measurements

Reaction	Energies(MeV)
$\vec{p}p \rightarrow \vec{p}p$	750, 700, 650, 600
$\vec{p}p \rightarrow \vec{d}\pi^+$	800, 650
$\vec{p}p \rightarrow \vec{p}n\pi^+$	800,650

A.8. HRS Focal Plane Polarization Analysis

The HRS focal plane polarizations were determined using the Fourier analysis (phi + pi criteria) method of ref A-8. Given these focal plane polarizations (the proton polarizations at the focal plane), the proton polarization at the target was calculated by taking the spin precession through the HRS dipoles into account, see eqn 3-2 thru 3-8. The azimuthal distribution of particles scattered in the carbon has the form:

$$I(\phi_c,\theta_c) = I_o(\theta_c)[1+\varepsilon_n(\theta_c)\cos\phi_c + \varepsilon_s(\theta_c)\sin\theta_c]A(\theta_c,\phi_c) \qquad (A-4)$$

where θ_c and ϕ_c are the polar and azimuthal carbon scattering angles respectively and $A(\theta_c,\phi_c)$ is the acceptance function. The scattering asymmetries in the normal and sideways directions are respectively represented by $\varepsilon_n(\theta_c)$ and $\varepsilon_s(\theta_c)$ (see eqns 3-11,12).

In the $\phi+\pi$ test the acceptance function is:

$$A(\theta_c,\phi_c) = A(\theta_c, \phi_c + \pi) \qquad (A-5)$$

So given the θ and ϕ distributions of scattered particles the focal plane polarizations can be obtained see section A.12. This $\phi + \pi$ test is useful because it eliminates false asymmetries (and thus false polarizations) that might arise due to the finite acceptance of the detector system.

A.9. Proton Spin Precession in a Magnetic Field

The spin of a proton is precessed in a magnetic field due to both Larmor and Thomas precession effects. A derivation of the expression for this precession can be found in the textbook of J.D. Jackson[A-9]. The time rate of change of the protons's spin is given by:

$$\frac{d\vec{s}}{dt} = \frac{e}{mc}\vec{s} \times \vec{B}[g/2 - 1 + 1/\gamma] \qquad (A\text{-}6)$$

where g is the g-factor of the proton, γ is the Lorentz contraction factor, m is the proton mass and $\vec{B}$ is the magnetic field of the HRS dipoles. The proton spin precession frequency is thus[A-9]:

$$\omega = \frac{eB}{mc}[g/2 - 1 + 1/\gamma] \qquad (A\text{-}7)$$

The precession of the proton momentum ($\vec{p}$) direction as it moves through a magnetic field, $\vec{B}$, is given by:

$$\frac{d\vec{p}}{dt} = \frac{e\vec{p}}{mc\gamma} \times \vec{B} \qquad (A\text{-}8)$$

$$\Omega = \frac{eB}{mc\gamma} \qquad (A\text{-}9)$$

By combining eqns A-7 and A-9 gives the precession frequency of the proton spin relative to the direction of the proton momentum:

$$\omega - \Omega = \gamma[g/2 - 1]\Omega \qquad \text{(A-10)}$$

i.e. if the proton momentum is bent an angle α in the HRS dipoles, then the proton spin precession angle relative to the proton momentum is:

$$\chi = \gamma[g/2 - 1]\alpha \qquad \text{(A-11)}$$

Note that the precession angle, χ, is independent of the magnetic field and depends only on the bend angle for a given energy. See section 3.A. for details on the proton spin observables and how they are affected by spin precession in the HRS dipoles.

A.10. Symmetry Properties

The proton-deuteron scattering amplitude was given in section 1.D. As stated in section 1.C., the spin observables obey several symmetries due to rotational, parity and time reversal invariance.

The construction of the most general pd scattering amplitude, F, is discussed in this section. Next some properties of both the spin 1/2 x 0 and spin 1/2 x 1 systems resulting from parity invariance are derived. Also in this section some symmetries in the spin observables resulting from time reversal invariance are derived.

The pd scattering amplitude, F, is a function of the kinematic quantities representing the degrees of freedom of the reaction. These are the momenta and the polarizations of the two particles before and after the scattering.

In the center of mass (CM) system, the only vector quantities available in momentum space are:

$\vec{k}_i$ initial proton momentum

$\vec{k}_f$ final proton momentum

From those one can construct the orthogonal unit vectors:

$$\hat{x} \propto \vec{k}_i - \vec{k}_f$$

$$\hat{y} \propto \hat{k}_i \times \hat{k}_f \qquad \text{(A-12)}$$

$$\hat{z} \propto \hat{k}_i + \hat{k}_f$$

All vector quantities in momentum space can be expanded as functions of these three base vectors. The quantities of vectorial character in spin space are:

$\hat{\sigma}$	proton spin operator	(A-13)
$\hat{J}$	deuteron vector spin operator	(A-14)
$\hat{Q}$	deuteron tensor spin matrix	(A-15)

Since the scattering amplitude F is rotationally invariant, it can only depend on scalar products of the vector quantities listed above. The scattering operator, $\hat{F}$, which is constructed from the scattering amplitude F, can be expanded as a polynomial in the operators corresponding to the scalar products mentioned above. In each term of the polynomial, there is a maximum of one of the σ_i's and a maximum of one of the J_i's or Q_{jk}'s, since any operator in spin space can be expressed as a linear combination of these spin operators plus their respective unity operators.

Using rotational invariance, the scattering amplitude can be written in terms of scalar products:

$$\hat{F} = F^o + \Sigma_i F^i \sigma_i + \Sigma_j F^j J_j + \Sigma_{jk} F_{jk} Q_{jk} + \Sigma_{ij} F^i_j \sigma_i J_j + \Sigma_{ijk} F^i_{jk} \sigma_i Q_{jk} \qquad \text{(A-16)}$$

The various terms in F are in the form which preserves rotational invariance, e.g.:

$$F^{x}\sigma_{x} = F^{x}\hat{x}\cdot\vec{\sigma}$$

$$F^{x}_{x}\sigma_{x}J_{x} = F^{x}_{x}(\hat{x}\cdot\vec{\sigma})(\hat{x}\cdot\vec{J}) \qquad \text{(A-17)}$$

$$F^{x}_{y}\sigma_{x}J_{y} = F^{x}_{y}(\hat{x}\cdot\vec{\sigma})(\hat{y}\cdot\vec{J})$$

Note that $\hat{x}$ projects out the x-component of $\vec{\sigma}$ etc. σ_x etc. are defined in table 1.

The behavior of the different components of the scattering amplitude under parity and time reversal in the CM system are listed in table 1. Under parity inversion, only $\hat{x}$ and $\hat{z}$ change sign since they are "proper vectors". But $\hat{y} = \hat{k}_i \times \hat{k}_f / |\hat{k}_i \times \hat{k}_f|$, $\vec{\sigma}$ and $\vec{J}-\hat{Q}$ are pseudovectors-tensor and do not change sign. A pseudovector is a vector that does not change sign under parity. Inspection of the expressions in eqn A-17 shows that terms appearing in $\hat{F}$ like $F^{j}_{i}\sigma_j J_i$ or $F^{k}_{ij}\sigma_k Q_{ij}$ change sign under parity when the number of x is and z indicies in F^{k}_{ij} is an odd number. Here we will denote the number of x and z occurences in the indicies of a given term by n_x and n_z respectively. Therefore, the scattering amplitudes do not have terms with $n_x + n_z$ odd because of parity invariance.

As a result of parity invariance, several results can be derived. First consider the spin observables $C(\alpha,\mu;\beta,\nu)$ of eqn 1-4:

$$C(\alpha,\mu;\beta,\nu) = Tr\{\hat{F}\sigma_\alpha\hat{O}_\mu\hat{F}^+\sigma_\beta\hat{O}_\nu\}/I_o \qquad (A\text{-}18)$$

where $\hat{O}$ are the deuteron spin-1 operators (either $\hat{J}_\mu$ or $\hat{Q}_{\mu\nu}$) and σ_α are the Pauli spin-1/2 operators defined in table 1. Note that μ and ν include all vector and tensor indicies in the deuteron spin operators. The trace given in eqn A-18 projects out a sum of terms of the form:

$$F^\gamma_\tau F^{\delta+}_\rho \qquad (A\text{-}19)$$

where γ, τ, δ and ρ represent any spin indicies. Since each of the F^γ_τ separately have $n_x + n_z$ even in the incicies γ and τ, then the product $F^\gamma_\tau F^{\delta+}_\rho$ also has $n_x + n_z$ even. Thus, we have proved eqn (1-9):

$$C(\alpha,\mu;\beta,\nu) = 0 \quad (\text{if } n_x + n_z \text{ is odd}) \qquad (A\text{-}20)$$

where $n_x + n_z$ is the number of occurences of x and z in the indicies α, μ, β and ν.

Consider now some properties of the spin observables resulting from time reversal invariance. As seen in table 1, under time reversal we have:

$$\vec{k}_i \to -\vec{k}_f$$

$$\vec{k}_f \to -\vec{k}_i$$

$$\vec{\sigma} \to -\vec{\sigma} \qquad \text{(A-21)}$$

$$\vec{J} \to -\vec{J}$$

$$\hat{Q} \to \hat{Q}$$

i.e. the quantities $\vec{y}$, $\vec{z}$, $\vec{\sigma}$ and $\vec{J}$ change sign under time reversal whereas $\vec{x}$ and $\hat{Q}$ do not (also see table 1). Consider the reaction denoted by:

$$\phi' = \hat{F}\phi \qquad \text{(A-22)}$$

where $\phi = |\vec{k}_i, \vec{\sigma}_i\rangle$ is the initial wave function and $\hat{F}$ is the scattering amplitude. Because F is invariant under time reversal, we have:

$$\phi'_{TR} = \hat{F}\phi_{TR} \qquad \text{(A-23)}$$

where $\phi_{TR} = |-\vec{k}_i, -\vec{\sigma}_i\rangle$ is the time reversed wave function. The time reversed reaction is:

$$\phi_{TR} = \hat{F}_{TR}\phi'_{TR} \tag{A-24}$$

or

$$\phi'_{TR} = \hat{F}^{+}_{TR}\phi_{TR} \tag{A-25}$$

since

$$\hat{F}^{-1} = \hat{F}^{+} \tag{A-26}$$

from unitarity considerations. By combining eqns (A-23) and (A-25) gives:

$$\hat{F}_{TR} = \hat{F}^{+} \tag{A-27}$$

Now consider the properties of the $D_{\alpha\beta}$'s under time reversal.

$$D^{TR}_{\alpha\beta} = Tr\{\sigma^{TR}_{\alpha}\hat{F}_{TR}\sigma^{TR}_{\beta}\hat{F}^{+}_{TR}\}/I^{TR}_{o} \tag{A-28}$$

$$I^{TR}_{o} = Tr\{\hat{F}\hat{F}^{+}\} = Tr\{\hat{F}_{TR}\hat{F}^{+}_{TR}\}$$

so

$$I^{TR}_{o} = Tr\{\hat{F}^{+}\hat{F}\} = Tr\{\hat{F}\hat{F}^{+}\} = I_{o} \tag{A-29}$$

Therefore the time reversal operation on I_o leaves it unchanged. Therefore:

$$D_{\alpha\beta}^{TR} = Tr\{\sigma_\alpha^{TR}\hat{F}_{TR}\sigma_\beta^{TR}\hat{F}^+_{TR}\}/I_o = Tr\{\sigma_\alpha^{TR}\hat{F}^+\sigma_\beta^{TR}\hat{F}\}/I_o = Tr\{\sigma_\beta^{TR}\hat{F}\sigma_\alpha^{TR}\hat{F}^+\}/I_o$$

so

$$D_{\alpha\beta}^{TR} = (-1)^{n_x}Tr\{\sigma_\beta\hat{F}\sigma_\alpha\hat{F}^+\}/I_o = (-1)^{n_x}D_{\beta\alpha} \qquad (A-30)$$

where n_x is the number of occurences of x in α and β. this proves eqn 1-10 (same as eqn A-30). Thus, for elastic scattering:

$$D_{xz} = -D_{zx} \qquad (A-31)$$

$$D_{0y} = D_{y0} \qquad (A-32)$$

or

$$P = A_y \qquad (A-33)$$

Eqn (A-33) is valid in all coordinate systems where the $\hat{y}$-direction is normal to the scattering plane since P and A_y are invariant of Lorentz transformations which leave $\hat{y}$ unchanged. On the other hand, eqn A-31 is in general only valid in the

coordinate system used here (see eqn A-12) and some other related systems, like the CM particle helicity frame[A-10], also see section 1.E. For example eqn A-31 is not valid in the laboratory particle helicity frame.

Several relations can be derived for the spin 1/2 x 0 scattering case (i.e. proton - ^{12}C elastic scattering). The most general scattering amplitude has the form[1-39]:

$$M = A + B(\hat{\sigma}\cdot\hat{n}) \tag{A-34}$$

The proton spin observables of eqn (1-18) are of the form:

$$D_{\alpha\beta} = Tr\{\sigma_\alpha M \sigma_\beta M^+\}/I_o \tag{A-35}$$

where

$$I_o = Tr\{MM^+\} \tag{A-36}$$

Since M only contains the proton spin operators $\hat{1}$ and $\hat{\sigma}_y$:

$$D_{nn} = 1 \qquad (\alpha = \beta = n = y) \tag{A-37}$$

and

$$P = A_y \qquad (\alpha = 0, \beta = y; \alpha = y, \beta = 0) \tag{A-38}$$

This proves the formula of section 3.K.2.

A.11. Wigner Rotations

This section contains the description of transforming the proton spin observables D_{xx}, D_{zz}, D_{xz} and D_{zx} (in either the Breit or CM frame) to the observables D_{ss}, $D_{\ell\ell}$, $D_{s\ell}$ and $D_{\ell s}$ in the laboratory system.

In any frame the spin rotation observables are defined as:

$$D_{\alpha\beta} = Tr\{F\sigma_\alpha F^+\sigma_\beta\}/Tr\{FF^+\} \qquad (A-39)$$

where $\alpha = x,y,z$ and $\beta = x,y,z$ in either the Breit or CM frames while in the lab frame $\alpha = s,n,\ell$ and $\beta = s',n',\ell'$ (see figures 1-2,3 and eqn 1-24).

In order to find the relations between the $D_{\alpha\beta}$ in the Breit (or CM) frames and the $D_{\alpha\beta}$ in the lab frame, it is necessary to transform the Pauli operators.

$\vec{\sigma} = (\sigma_x,\sigma_y,\sigma_z)$ in Breit or CM frames

$\vec{\sigma} = (\sigma_s,\sigma_n,\sigma_\ell)$ in $sn\ell$ initial proton lab frame (A-40)

$\vec{\sigma} = (\sigma_{s'},\sigma_{n'},\sigma_{\ell'})$ in $s'n'\ell'$ final proton lab frame

Since the normal direction ($\perp$ to the scattering plane) is the same in all of these coordinate systems ($\hat{n} = \hat{n}' = \hat{y}_{cm} = \hat{y}_B$), only rotations in the plane of scattering are of interest. The following relations describe the rotations for the proton spin operators:

$$\begin{pmatrix} \sigma_s \\ \sigma_\ell \end{pmatrix} = \begin{pmatrix} \cos\chi & \sin\chi \\ -\sin\chi & \cos\chi \end{pmatrix} \begin{pmatrix} \sigma_x \\ \sigma_z \end{pmatrix} \tag{A-41}$$

$$\begin{pmatrix} \sigma_{s'} \\ \sigma_{\ell'} \end{pmatrix} \begin{pmatrix} \cos\chi' & \sin\chi' \\ -\sin\chi & \cos\chi' \end{pmatrix} \begin{pmatrix} \sigma_x \\ \sigma_z \end{pmatrix} \tag{A-42}$$

where σ_x and σ_z are defined in either the Breit or CM frames and σ_s and σ_ℓ are defined in the lab frame. Here χ is the relativistic rotation angle between the $\hat{\ell}$ and $\hat{z}$ axes and χ' is the corresponding rotation angle between the $\hat{\ell}'$ and $\hat{z}$ axes. By substituting the results from eqns (A-41,42) into the formulas for the $D_{\alpha\beta}$ (eqn A-39), e.g.:

$$\begin{aligned} D_{\ell\ell'} &= \mathrm{Tr}\{F\sigma_\ell F^+\sigma_{\ell'}\} \\ \sigma_\ell &= -\sin\chi\sigma_x + \cos\chi\sigma_z \\ \sigma_{\ell'} &= -\sin\chi'\sigma_x + \cos\chi'\sigma_z \end{aligned} \tag{A-43}$$

The result is given in eqn (3-32). As seen in eqn (3-32), the transformation between the lab and the Breit (or CM) systems is a 4 x 4 matrix multipication where the matrix elements are products

of $\sin\chi$, $\cos\chi$, $\sin\chi'$ and $\cos\chi'$. The method for determining χ and χ' is given below. Note that in transforming the spin observables, it is only necessary to see how the Pauli operators transform since the scattering amplitude, F, is the same in these reference frames (invariant - see section A.10.).

In order to find χ and χ', the method using relativistic velocity diagrams will be described here. In this approach, the velocities of the particles in the reaction, $\vec{p}d \to \vec{p}d$, are represented as points on the hyperbola:

$$v_o^2 - \vec{v}^2 = 1 \qquad \text{(A-44)}$$

where this eqn represents the dot product of the four-velocity $v_\mu \cdot v^\mu$. For the reaction $\vec{p}d \to \vec{p}d$, the velocity diagram is shown in fig. A-8. As seen in the figure, the three coordinate systems - Breit, CM and laboratory systems are represented as the points B, c and d respectively. In this diagram, the points are defined as:

d = incident deuteron rest mass frame (lab frame)

d' = scattered deuteron rest mass frame

p = incident proton rest mass frame (anti-laboratory frame)

p' = scattered proton rest mass frame (A-45)

c = center of mass (CM) frame

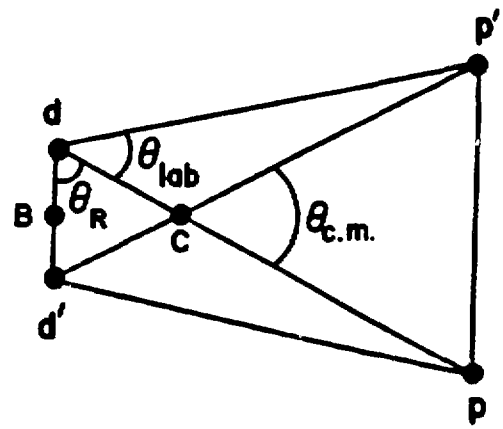

FIGURE A-8

Relativistic velocity diagram

B = Breit frame (brick wall frame-see section 1.C.)

Note that the trapizoid of fig. A-8 is symmetric (top and bottom of equal length) because this reaction is an elastic scattering process. It is convenient to define the following scattering angles:

$$\theta_{CM} = \langle pcp' \qquad (A\text{-}46)$$

$$\theta_{lab} = \langle pdp'$$

$$\theta_B = \langle pBp'$$

$$\theta_{lab} = \langle dpd'$$

$$\theta_R = \langle d'dp$$

$$\alpha = \langle Bpd$$

Here θ_{cm}, θ_{lab} and θ_B represent the proton scattering angles in the CM, lab and Breit systems respectively. θ_{lab} is the deuteron scattering angle in the anti-laboratory system (incident proton rest mass frame). θ_R is the deuteron recoil angle in the lab frame and α is the angle between the velocities of the Breit and lab frames as seen from the anti-laboratory system. The convenience of using this velocity diagram to determine χ and χ' is that all particles are on the same hyperbola. Lorentz transformations could also be used but the method using relativistic velocity diagrams is simpler and gives the same

result. Since the proton and deuteron have different masses ($E^2 - p^2 = m^2$), they could not be put on the same momentum hyperbola, as they can be in velocity space.

The coordinate systems to be considered are right-handed cartesian reference frames. In fig A-8, the CM system is defined as:

C - origin of CM frame

x_c - axis pointing down (A-47)

y_c - axis into paper

z_c - axis pointing to the right

In fig. A-8, the Breit frame is described by:

B - origin of Breit frame

x_B - axis pointing down (A-48)

y_B - axis pointing into paper

z_B - axis pointing to the right

In fig. A-8, the lab system points are labelled:

d - origin of laboratory frame

$\hat{\ell}$ - points from d to p

$\hat{\ell}'$ - points from d to p′ (A-49)

$\hat{n} = \hat{n}'$ - points into paper

$\hat{s} = \hat{n} \times \hat{\ell}$

$\hat{s}' = \hat{n}' \times \hat{\ell}'$

Since this diagram represents a velocity hyperbola, it should be noted that x_c and z_c are not parallel to x_B and z_B. The transformation angles between the lab and CM frames have the form:

$$\chi_c = \theta_{cm}/2 - \delta_{dcp} \tag{A-50}$$

$$\chi_{c'} = -\theta_{lab} + \theta_{cm}/2 - \delta_{dcp'} \tag{A-51}$$

Here δ represents the defect of the relativistic triangle[1-40] and is a purely relativistic correction in both χ_c and $\chi_{c'}$. The defect, δ, is given by[1-40]:

$\delta = \pi$ - sum of the angles in the triangle

as seen in fig. A-8,

$$\delta_{dcp} = 0 \tag{A-52}$$

$$\delta_{dcp'} = \pi - [\theta_{lab} + \theta_{lab} + (\pi - \theta_{cm})]$$

Here from symmetry $\angle cp'd = \theta_{lab}$. Combining eqns A-50,51,52 gives:

$$\chi_c = \theta_{cm}/2 \qquad \text{(A-53)}$$

$$\chi_c' = -\theta_{cm}/2 + \theta_{lab}$$

which represents the transformations between the lab and CM frames given in eqn (3-33).

The transformation angles between the lab and Breit frames are of the form (see fig A-8):

$$\chi_B = \pi/2 - \theta_R - \delta_{dBp} \qquad \text{(A-54)}$$

$$\chi_B' = \pi/2 - \theta_R - \theta_{lab} - \delta_{dBp'}$$

where the relativistic defects are:

$$\delta_{dBp} = \pi - (\theta_R + \alpha + \pi/2 + \theta_B/2) = \pi/2 - \theta_R - \alpha - \theta_B/2 \qquad \text{(A-55)}$$

$$\delta_{dBp'} = \pi - (\theta_{lab} + \theta_R + \theta_{lab} - \alpha + \pi/2 - \theta_B/2)$$

$$= \pi/2 - \theta_R - \theta_{lab} + \theta_B/2 + \alpha - \theta_{lab}$$

Combining eqns (A-54,55) gives:

$$\chi_B = \theta_B/2 + \alpha \qquad \text{(A-56)}$$

$$\chi_B' = -\theta_B/2 - \alpha + \theta_{lab}$$

These results are given in eqn (1-23) for the transformation between the lab observables and the Breit parameters.

In the following part of this section, the derivation of the transformation shown in eqn (1-22) is presented. The transformation to be described gives the expressions for the depolarization parameters, D_j, in the Breit frame as linear combinations of the experimental spin rotation observables, $D_{\alpha\beta}$, in the laboratory (particle helicity) frame. In the Breit frame we have[A-10]:

$$\begin{aligned} D_o &= 1/4[1 + D_{xx} + D_{yy} + D_{zz}] \\ D_x &= 1/4[1 + D_{xx} - D_{yy} - D_{zz}] \\ D_y &= 1/4[1 - D_{xx} + D_{yy} - D_{zz}] \\ D_z &= 1/4[1 - D_{xx} - D_{yy} + D_{zz}] \end{aligned} \tag{A-57}$$

where the D_j and $D_{\alpha\beta}$ are defined in eqns (1-18,20). Using eqns (A-41,42), the following laboratory to Breit system relations are obtained:

$$\begin{aligned} D_{xx} &= cc'D_{ss} + ss'D_{\ell\ell} - sc'D_{\ell s} - cs'D_{s\ell} \\ D_{zz} &= ss'D_{ss} + cc'D_{\ell\ell} + cs'D_{\ell s} + sc'D_{s\ell} \\ D_{zx} &= sc'D_{ss} - cs'D_{\ell\ell} + cc'D_{\ell s} - ss'D_{s\ell} \\ D_{xz} &= cs'D_{ss} - sc'D_{\ell\ell} - ss'D_{\ell s} + cc'D_{s\ell} \end{aligned} \tag{A-58}$$

where

$$c = \cos\chi$$

$$c' = \cos\chi' \qquad \text{(A-59)}$$

$$s = \sin\chi$$

$$s' = \sin\chi'$$

Substituting into eqns (A-57) gives:

$$D_o = 1/4[1 + D_{nn} + \cos(\chi-\chi')(D_{ss} + D_{\ell\ell}) + \sin(\chi-\chi')(D_{s\ell} - D_{\ell s})]$$

$$D_x = 1/4[1 - D_{nn} + \cos(\chi-\chi')(D_{ss} - D_{\ell\ell}) - \sin(\chi+\chi')(D_{s\ell} + D_{\ell s})] \qquad \text{(A-60)}$$

$$D_y = 1/4[1 + D_{nn} - \cos(\chi-\chi')(D_{ss} + D_{\ell\ell}) - \sin(\chi-\chi')(D_{s\ell} - D_{\ell s})]$$

$$D_z = 1/4[1 - D_{nn} - \cos(\chi+\chi')(D_{ss} - D_{\ell\ell}) + \sin(\chi+\chi')(D_{s\ell} + D_{\ell s})]$$

where the following trigometric properties have been used:

$$\cos(\chi-\chi') = \cos\chi\cos\chi' + \sin\chi\sin\chi'$$

$$\sin(\chi-\chi') = \sin\chi\cos\chi' - \cos\chi\sin\chi' \qquad \text{(A-61)}$$

$$\cos(\chi+\chi') = \cos\chi\cos\chi' - \sin\chi\sin\chi'$$

$$\sin(\chi+\chi') = \sin\chi\cos\chi' + \cos\chi\sin\chi'$$

Therefore by transforming from the lab observables, D_{ss}, $D_{\ell\ell}$, $D_{s\ell}$ and $D_{\ell s}$ to the observables, D_{xx}, D_{zz}, D_{xz} and D_{zx} (in either the Breit or CM systems), one obtains the D_j's.

A.12. Determination of the Scattered Proton Polarization

As mentioned in section 3.A., the measurement of the proton spin observables involves the determination of the scattered proton polarization from the proton polarizations measured at the HRS focal plane. In this section the formalism to correct the proton spin observables for out-of-plane scattering effects, that tend to mix final-state polarizations is described. The approach taken here allows for corrections to be made after the "first order" values have been determined. In most cases, corrections to one spin transfer observable involve values of other spin transfer observables.

Because the transport of the outgoing target polarization vector depends critically on the optics of the spectrometer, a brief description of the HRS is appropriate. As mentioned in section 2.B., the HRS is a vertical-dispersion, horizontal-scattering, vertical-analysis (VHV) quadrupole-dipole-multipole-dipole (QDMD) spectrometer. The total bend in the dispersion plane is 150° with point-to-point focusing in the vertical and point-to-parallel focusing in the horizontal directions. The angular acceptance at the target is limited to ±1° in the horizontal and ±2° in the vertical. More details on the HRS may be found in Refs. 2-3 and A-11.

We define five coordinate systems to completely describe the scattering process. The first is the "beam-line" system labeled as ($\hat{s}_o$, $\hat{n}_o$, $\hat{\ell}_o$) in Fig. A-9. This is used for definition of beam

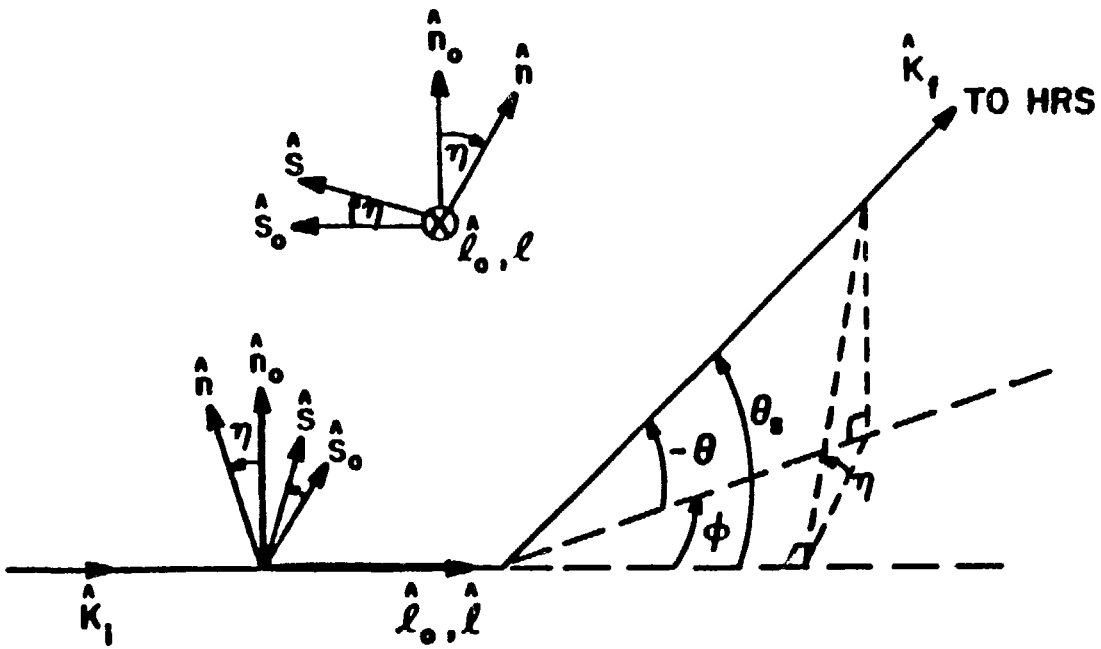

FIGURE A-9

HRS Coordinate Systems

polarization. Second is the "incident-particle" frame given by $(\hat{s},\ \hat{n},\ \hat{\ell})$ where $\hat{n} = \vec{k}_i \times \vec{k}_f / |\vec{k}_i \times \vec{k}_f|$ is the normal to the reaction plane $\hat{\ell} = \hat{\ell}_o$ and $\hat{s} = \hat{n} \times \hat{\ell}$. The "beam-line" and "incident-particle" frames coincide when the azimuthal scattering angle at the target η in Fig. A-9 is zero. Note that the azimuthal scattering angle at the target was previously referred to as ϕ in chapter 3. The vertical scattering angle at the target is θ (+ down), ϕ is the horizontal, and the true scattering angle at the target is θ_S. The relation between the various angles in Fig. A-9 is given by:

$$\tan \theta_S = \tan \theta \quad 1 + \frac{\tan^2 \phi}{\sin^2 \theta} \tag{A-62}$$

$$\tan \eta = \frac{\tan \phi}{\sin \theta} \tag{A-63}$$

The third system is the "scattered-particle" frame given by $(\hat{s}',\ \hat{n}',\ \hat{\ell}')$ with $\hat{n}' = \hat{n}$, $\hat{\ell}'$ along $\vec{k}_f$ and $\hat{s}' = \hat{n}' \times \hat{\ell}'$. the second and third frames are important because the actual scattering process is defined in terms of them. A further rotation that aligns $\hat{s}'$ along the magnetic field lines of the HRS dipoles is convenient, allowing for a semidefinite axis along which to precess the spin through the HRS dipoles. This fourth system is the "dipole" frame given by $(\hat{s}'',\ \hat{n}'',\ \hat{\ell}'')$. Finally, the actual measurements are made in the "focal-plane" system.

Polarizations are calculated for the two transverse components at the focal plane $P_n(FP)$ and $P_s(FP)$.

The polarization of the incoming beam measured in the "beam-line" system ($\hat{s}_o$, $\hat{n}_o$, $\hat{\ell}_o$) is given by:

$$\vec{P}_B^0 = \begin{pmatrix} P_s^0 \\ P_n^0 \\ P_\ell^0 \end{pmatrix} \tag{A-64}$$

The same beam polarization measured in the "incident-particle" system ($\hat{s}$,$\hat{n}$,$\hat{\ell}$) is given by:

$$\vec{P}_B = \begin{pmatrix} P_s \\ P_n \\ P_\ell \end{pmatrix} = \begin{pmatrix} \cos\eta & \sin\eta & 0 \\ -\sin\eta & \cos\eta & 0 \\ 0 & 0 & 1 \end{pmatrix} \vec{P}_B^0 \tag{A-65}$$

The polarization of the scattered particle in the "scattered-particle" system ($\hat{s}'$, $\hat{n}'$, $\hat{\ell}'$) is given by (see eqn 4-1):

$$\vec{P}' = \begin{pmatrix} P_s' \\ P_n' \\ P_\ell' \end{pmatrix} = \left[\begin{pmatrix} R & 0 & A \\ 0 & D & 0 \\ R' & 0 & A' \end{pmatrix} \vec{P}_B + \begin{pmatrix} 0 \\ P(\theta_S) \\ 0 \end{pmatrix} \right] \frac{1}{1 + P_n A_y} \tag{A-66}$$

where D, R, A, R′, and A′ are the commonly-referred-to Wolfenstein parameters (D_{NN}, D_{SS}, D_{LS}, D_{SL}, and D_{LL}, respectively). $P(\theta_S)$ is the polarization function and A_y is the vector analyzing power for the reaction. The $\hat{s}'$ vector is now rotated into the horizontal plane of the dipoles to give:

$$\vec{P}'' = \begin{pmatrix} \cos\eta & -\sin\eta & 0 \\ \sin\eta & \cos\eta & 0 \\ 0 & 0 & 1 \end{pmatrix} \vec{P}' \tag{A-67}$$

A more complicated expression is needed to transform into the "dipole" frame if the effects of the quadrupole are explicitly taken into account. Relying on the quadrupole field to produce nearly parallel rays in the horizontal plane going into the dipole fields allows for the simplified form of the true rotation. We now assume that precession in the dipoles takes place about the $\hat{s}$" axis only. The justifications for these approximations are discussed in ref. 2-6. The polarization at the focal plane is then given by:

$$\vec{P}(FP) = \begin{pmatrix} 1 & 0 & 0 \\ 0 & \cos\chi & \sin\chi \\ 0 & -\sin\chi & \cos\chi \end{pmatrix} \vec{P}'' \qquad \text{(A-68)}$$

where χ is the precession angle of the proton polarization with respect to its momentum and is given by (see section A.9.):

$$\chi = \gamma\left(\frac{g}{2} - 1\right)\alpha \simeq 269\ \gamma \qquad \text{(A-69)}$$

γ is the Lorentz factor, $\frac{g}{2}$ is the proton magnetic moment (2.793), and α is the bend angle in the HRS ($\sim 150^{\circ}$). Some variation in α occurs as a result of different trajectories within the HRS. These are calculated event by event in the determination of χ and averages over all events are made (see ref 2-6).

A.11.A $\hat{n}$-Type Beam

Consider a beam polarized along the $\hat{n}$ direction. Following the development of section A.11. we obtain:

$$\vec{P}_B^0 = \begin{matrix} 0 \\ 1 \\ 0 \end{matrix} P_n$$

$$\vec{P}_B = \begin{matrix} \sin\eta \\ \cos\eta \\ 0 \end{matrix} P_n$$

$$\vec{P}' = \begin{matrix} P_nR \sin\eta \\ P_nD \cos\eta + P(\theta_S) \\ P_nR' \sin\eta \end{matrix} \frac{1}{1 + P_nA_y \cos\eta}$$

$$\vec{P}'' = \begin{matrix} P_nR \cos\eta \sin\eta - [P_nD \cos\eta + P(\theta_S)] \sin\eta \\ P_nR \sin^2\eta + [P_nD \cos\eta + P(\theta_S)] \cos\eta \\ P_nR' \sin\eta \end{matrix} \frac{1}{1 + P_nA_y \cos\eta}$$

$$\vec{P}(FP) = \begin{matrix} P_nR \cos\eta \sin\eta - [P_nD \cos\eta + P(\theta_S)] \sin\eta \\ \{P_nR \sin^2\eta + [P_nD \cos\eta + P(\theta_S)] \cos\eta\} \cos\chi + P_nR' \sin\eta \sin\chi \\ -\{P_nR \sin^2\eta + [P_nD \cos\eta + P(\theta_S)] \cos\eta\} \sin\chi + P_nR' \sin\eta \cos\chi \end{matrix}$$

$$* \frac{1}{1 + P_nA_y \cos\eta} \qquad \text{(A-70)}$$

Data are taken for both normal (spin up) and reverse (spin down) beam polarizations, P_n^+ and P_n^-, respectively. We assume $P_n^+ = -P_n^- \equiv P_n$.

As the asymmetry for $\hat{n}$-type beam is in the horizontal plane, the distribution of η is the same for normal and reverse such that:

$$\begin{matrix}\cos\eta \\ \sin\eta\end{matrix} - = \begin{matrix}\cos\eta \\ \sin\eta\end{matrix}^{+} \qquad \text{(A-71)}$$

in the absence of cuts to the data that could produce a skewed η distribution. (See ref 2-6.) After some algebra and averaging over events as described in ref 2-6, we obtain:

$$D = D_{NN} = D_o - \frac{1}{\langle\cos\ \eta\rangle^2}\left(R\langle\sin^2\ \eta\rangle + R'\langle\sin\ \eta\rangle\langle\tan\ \chi\rangle\right)$$

where

$$D_o = \frac{1}{P_n\ \langle\cos\ \eta\rangle^2\langle\cos\ \chi\rangle}\ \frac{[P_n^{+}(FP)-P_n^{-}(FP)]}{2}$$

$$+\ P_nA_y\ \langle\cos\ \eta\rangle\ \frac{[P_n^{+}(FP)+P_n^{-}(FP)]}{2}$$

and (A-77)

$$P(\theta_S) = \frac{1}{\langle\cos\ \eta\rangle\ \langle\cos\ \chi\rangle}\ \frac{[P_n^{+}(FP)+P_n^{-}(FP)]}{2}$$

$$+\ P_nA_y\ \langle\cos\ \eta\rangle\ \frac{P_n^{+}(FP)-P_n^{-}(FP)}{2}$$

$P_n^+(FP)$ and $P_n^-(FP)$ are the focal-plane polarizations measured with normal and reverse beam polarization, and $\langle\ \rangle$ refers to the average over events.

A.11.B. $\hat{s}$-Type Beam

Following section A.11.A we get:

$$\hat{P}(FP) = \begin{matrix} P_s\,(R\cos^2\eta + D\sin^2\eta) \cdot\cdot P(\theta_S)\sin\eta \\ [P_s\,(R-D)\sin\eta\cos\eta + P(\theta_S)\cos\eta]\cos\chi + P_s R'\cos\eta\sin\chi \\ -[P_s\,(R-D)\sin\eta\cos\eta + P(\theta_S)\cos\eta]\sin\chi + P_s R'\cos\eta\cos\chi \end{matrix} * \frac{1}{1 - P_s A_y \sin\eta} \qquad \text{(A-73)}$$

Here the asymmetry at the target is in the vertical plane, hence the distribution of η is opposite for normal and reverse in the absence of cuts to the data, such that:

$$\begin{matrix} \cos\eta \\ \sin\eta \end{matrix} - = \begin{matrix} \cos\eta \\ -\sin\eta \end{matrix} + \qquad \text{(A-74)}$$

This yields

$$R = D_{SS} = R_o(1 - P_s A_y \langle\sin\eta\rangle) - \frac{D\langle\sin^2\eta\rangle}{\langle\cos^2\eta\rangle} + \frac{P(\theta_S)\langle\sin\eta\rangle}{P_s\langle\cos^2\eta\rangle}$$

where

$$R_o = \frac{P_s^+(FP) - P_s^-(FP)}{2P_s \langle \cos^2 \eta \rangle}$$

$$R' = D_{SL} = R_o' (1 - P_s A_y \langle \sin \eta \rangle)$$

where

$$R_o' = \frac{P_n^+(FP) - P_n^-(FP)}{2P_s \langle \cos \eta \rangle \langle \sin \chi \rangle}$$

and

$$P(\theta_S) = P_o(\theta_S) (1 - P_s A_y \langle \sin \eta \rangle) - P_s \langle \sin \eta \rangle (R - D)$$

where

$$P_o(\theta_S) = \frac{P_n^+(FP) + P_n^-(FP)}{2 \langle \cos \eta \rangle \langle \cos \chi \rangle} \qquad \text{(A-75)}$$

A.11.C. $\hat{\ell}$-Type Beam

In this case:

$$\vec{P}_B = \vec{P}_B^0 = \begin{matrix} 0 \\ 0 \\ 1 \end{matrix} \; P_\ell$$

and

$$\vec{P}(FP) = \begin{matrix} P_\ell A \cos\eta - P(\theta_S) \sin\eta \\ [P_\ell A \sin\eta + P(\theta_S) \cos\eta] \cos\chi + P_\ell A' \sin\chi \\ -[P_\ell A \sin\eta + P(\theta_S) \cos\eta] \sin\chi + P_\ell A' \cos\chi \end{matrix} \quad \text{(A-76)}$$

As there are no asymmetries transverse to the beam in the absence of cuts to the data, the η distribution is the same normal and reverse. This gives:

$$A = D_{LS} = \frac{P_S^+(FP) - P_S^-(FP)}{2P_\ell \langle\cos\eta\rangle}$$

$$A' = D_{LL} = A_0' - A \langle\sin\eta\rangle \langle\cot\chi\rangle$$

where

$$A_o' = \frac{P_n^+(FP) - P_n^-(FP)}{2P_\ell \langle \sin \chi \rangle}$$

and

$$P(\theta_S) = \frac{P_n^-(FP) + P_n^+(FP)}{2 \langle \cos \eta \rangle \langle \cos \chi \rangle} \qquad \text{(A-77)}$$

These expressions were given in eqns 3-2 through 3-8. For more details on the calculation of these observables see ref. 2-6.

References

1-1 G. Alberi et. al.,Phy. Lett. 92B(1980)41.

1-2 M. Bleszynski, Phys. Lett. 92B(1980)91.

1-3 M. Bleszynski et. al., Phys. Lett. 106B(1981)42.

1-4 R.A. Arndt and L.D. Roper, private communication.

1-5 E. Aprile et. al., Phys. Rev. Lett. 46(1981)1047.

1-6 R.F. Rodebaugh and B.E. Bonner, "Amplitude Reconstruction for pp Scattering at 800 MeV", Few Body Conference, Karlsruhe, Germany (1983).

1-7 G. Alberi, M. Bleszynski and T. Jasoszewicz, Ann. Phys. 142(1982)299.

1-8 L. Wolfenstein, Phys. Rev. 96(1954)1654.

1-9 L. Wolfenstein, Ann. Rev. of Nucl. Sci. 6(1956)43.

1-10 G. Igo, Proc. of IX Intern. Conf. on High Energy Phys. and Nucl. Struc., Ed. P. Calillon et. al., Nucl. Phys. A374(1982)253.

1-11 J.M. Cameron, Proc. of VIII Intern. Conf. on High Energy Phys. and Nucl. Struc., Ed. D.F. Measday and A.W. Thomas, Nucl. Phys. A235(1980)453.

1-12 C. Bruge, Proc. of VII Intern. Conf. on High Energy Phys. and Nucl. Struc., Ed. M.P. Locher (Birkhauser Verlag, 1977)69.

1-13 J.E. Simmons, Proc. of VI Intern Conf. on High Energy Phys. and Nucl. Struc., Ed. D.E. Nagle et. al., (AIP, New York, 1975)103.

1-14 G.W. Bennett et. al., Phys. Rev. Lett. 19(1967)387.

1-15 E. Coleman et. al., Phys. Rev. Lett. 16(1966)761.

1-16 E. Coleman et. al., Phys. Rev. 164(1967)1655.

1-17 D.R. Harrington, Phys Rev. Lett. 21(1968)1496.

1-18 V. Franco and R.J. Glauber, Phys Rev. Lett. 22(1969)370.

1-19 N.E. Booth et. al., Phys. Rev. D 4(1971)1261.

1-20 E.T. Boschitz et. al., Phys Rev. C6(1972)457.

1-21 J.C. Alder et. al., Phys. Rev. C6(1972)2010.

1-22 L. Dubal et. al., Phys. Rev. D9(1974)597.

1-23 A.N. Anderson et. al., Phys. Rev. Lett. 40(1978)1553.

1-24 E. Biegert et. al., Phys. Rev. Lett. 41(1978)1098.

1-25 M.G. Albrow et. al., Phys. Lett. 35B(1971)247.

1-26 G. Bunce et. al., Phys. Rev. Lett. 28(1972)120.

1-27 G. Igo et. al., Phys. Rev. Lett. 43(1979)425.

1-28 M. Bleszynski et. al., Phys. Lett. 87B(1979)198.

1-29 E. Winkelmamm et. al., Phys. Rev. C21(1980)2535.

1-30 A.A. Rahbar, UCLA Thesis, Los Alamos Report LA-9505-T (1982).

1-31 A.A. Rahbar et. al., submitted to Phys. Rev. Lett.

1-32 Sun Tsu-hsun et. al., Few Body Conference, Karlsruhe, Germany (1983).

1-33 Sun Tsu-hsun et. al., accepted by Phys. Rev. C.

1-34 G.S. Weston et. al., Bull. Am. Phys. Soc. 28(1983)996.

1-35 B.E. Bonner et. al., Few Body Conference, Karlsruhe, Germany (1983).

1-36 D. Cremans et. al., Few Body Confernece, Karlsruhe, Germany (1983).

1-37 M.W. McNaughton et. al., submitted to Phys. Rev. Lett.

1-38 W. Reid, Ann. of Phys. 192(1982)233.

1-39 G. Ohlsen, Rep. Prog. Phys. 35(1972)717.

1-40 M. Bleszynski, UCLA, private communication.

2-1 LAMPF Users Handbook, MP-DO-1-UHB (Rev.), 1980.

2-2 LAMPF Pamphlet, LALP-82-5.

2-3 B. Zeidman, The HRS Spectrometer System:Concepts and Design-LANL Report LA-4773-MS, Part 1, (1971).

2-4 C.L. Morris et. al., Nucl. Instr. Meth. 196(1982)263.

2-5 L.G. Atencio et. al., Nucl. Instr. Meth. 187(1981)381.

2-6 J.B.McClelland et. al., to be submitted to NIM and published as Los Alamos National Laboratory report, LA-UR-.

2-7 R.D. Ransome et. al., Nucl. Instr. Meth. 201(1982)309.

3-1 M.W.McNaughton, Los Alamos Informal Report LA-8307-MS.

3-2 M.W.McNaughton et. al., Phys. Rev. C 23 (1981)1128.

3-3 R.D. Ransome et. al., Nucl. Instr. Meth. 201(1982)315.

3-4 R.D. Ransome et. al., Thesis, Los Alamos Scientific Laboratory, LA-8919-T(1981).

3-5 P.R. Bevington et. al., Phys. Rev. Lett. 41(1978)384.

3-6 M.W.McNaughton, private communication.

3-7 Particle Properties Data Booklet (1982).

3-10 J.B. McClelland et. al., Phys. Rev. Lett. (1983).

3-11 R.W. Fergeusen, Univ. of Texas, private communication.

4-1 R.Amado and S. Wallace, Phys. Today 37no.1(1984)s40.

A-1 S. Ishimoto, S. Isagawa, A. Masaike and K. Morimoto, Nucl. Instr. Meth. 171(1980)269.

A-2 A. Masaike, Argonne National Lab report ANL-HEP-PR-77-88 (1977).

A-3 O.V. Lounasmaa, "Experimental Principles and Methods Below 1K," Academic Press (1974).

A-4 O. Hamada, S. Hiramatsu, S. Isagawa, S. Ishimoto, A. Masaike and K. Morimoto, Nucl. Instr. and Meth. 189(1981)561.

A-5 G. Pauletta, NMR software.

A-6 F. Sperisen, DMR software.

A-7 K. Muto and D. Hirakawa, Jour. of Phys. Soc. of Japan, 42(1977)1467.

A-8 D. Besset et. al., Nucl. Instr. Meth. 166(1979)515.

A-9 J.D. Jackson, "Classical Electrodynamics", Second Edition, Wiley, New York, 1975.

A-10 E. Bleszynski, M. Bleszynski and C.A. Whitten, Jr., Phys. Rev. C.26(1982)2063.

A-11 T. Kozlowski et. al., Los Alamos National Laboratory report, LA-4773-MS, Part 1(1971).

A-12 B. Aas, UCLA, private communication.

☆U.S. GOVERNMENT PRINTING OFFICE 1984—776-026/4130